High-Intensity Pulses in the Terahertz and Visible Ranges

DSc Dissertation

József András Fülöp

MTA-PTE High-Field Terahertz Research Group

Pécs, 2017.

This work is dedicated to my wife Nurcahaya and to my children Sára, Sámuel, Nóra, and Magdaléna.

Contents

Abbreviations

2D	two-dimensional
2PA, 3PA, 4PA	two-, three-, four-photon absorption
ARWG	absorption-reduced waveguide
CG	contact grating
cLN	congruent lithium niobate ($LiNbO_3$)
CPA	chirped-pulse amplification
CT	cryogenic temperature
DFG	difference-frequency generation
EOS	electro-optic sampling
FCA	free-carrier absorption
FL	Fourier limit, Fourier limited
FWHM	full width at half maximum
GVD	group velocity dispersion
MPA	multi-photon absoprtion
OPA	optical parametric amplification
OPCPA	optical parametric chirped-pulse amplification
OR	optical rectification
LN	lithium niobate ($LiNbO_3$)
PFT	pulse-front tilt
RT	room temperature
SFG	sum-frequency generation
SHG	second-harmonic generation
SPIDER	spectral phase interferometry for direct electric field reconstruction
sLN	stoichiometric lithium niobate ($LiNbO_3$)
TPFP	tilted-pulse-front pumping

I. Introduction

The application possibilities of electromagnetic radiation sources are determined and limited by their coherence, spectral content (bandwidth), and intensity or field strength. These features are often interrelated. New applications require the improvement of source characteristics and to tailor them to specific needs. The advent of the laser enabled the construction of light sources with unprecedented coherence properties. The high degree of coherence was essential for pushing the limits both in bandwidth and intensity.

The energy of highly coherent radiation can be confined to extremely narrow spectral or temporal intervals. An extremely narrow bandwidth and high frequency stability is needed for precision spectroscopy. The confinement of radiation energy to very short time intervals opened up the field of ultrafast spectroscopy. Generally, the achievable pulse duration is inversely proportional to the spectral bandwidth (a more precise formulation can be found e.g. in Ref. [1]). Thus, a very short pulse must have a very large bandwidth.

Besides time-resolved studies on ultrafast time scales, the confinement of light energy to very short time scales also enables to reach extremely high intensities and field strengths. Prominent application examples of ultrahigh-intensity pulses are laser-driven electron and ion acceleration.

The emission bandwidth and wavelength range of laser materials sets a limit on the achievable pulse duration. In laser amplifier systems the bandwidth can be significantly reduced by the gain-narrowing effect. Furthermore, spectroscopic applications often request wavelengths which are not, or not easily, accessible by laser materials. Thus, frequency conversion and spectral broadening of laser sources is of utmost practical importance.

The generation of new frequency components, not present at the input of an optical device, requires a nonlinear process. In 1961, only one year after the first demonstration of laser operation, second-harmonic generation of a laser beam was performed. This marked the birth of nonlinear optics. Second-harmonic generation and a wealth of other nonlinear optical processes represent key technologies to reach frequency ranges or bandwidths which are not directly accessible by laser materials. Nonlinear frequency conversion of laser radiation is now the basis for coherent radiation sources from the X-ray to the microwave regime. Besides accessing new spectral regimes, nonlinear optical processes, such as optical parametric amplification, can also be used to reach unprecedented peak intensities. Nonlinear optical frequency conversion or amplification were essential in making the laser an extremely versatile tool for science and technology.

This work deals with topics on the development of nonlinear optical amplification and frequency conversion techniques.

The ultimate limit for shortening the pulse duration is set by the carrier frequency of the radiation. The duration of a single oscillation cycle is about 3 fs for optical wavelengths near 1 μm. Frequency conversion of laser radiation to the extreme ultraviolet or soft x-ray enabled to significantly shorten the pulse duration because of the much

shorter oscillation cycle. The shortest electromagnetic pulses routinely available today from laser-driven secondary sources are about 50 attosecond long. Such pulses can be generated by high-order harmonic generation in gas jets, a highly nonlinear process requiring intense few-cycle driver laser pulses. The generation of stronger and shorter attosecond pulses may be possible at even shorter wavelengths generated from solid-density targets with the help of high-power few-cycle laser pulses.

One main goal of the work presented here was to develop the technology of high-power few-cycle pulse sources in the visible—near infrared spectral range using optical parametric amplification. This was motivated by the quest for suitable primary sources to drive novel attosecond sources and other high-field applications like laser-driven electron acceleration. The experimental work related to optical parametric amplification was mainly carried out at the Max Planck Institute of Quantum Optics and the Ludwig Maximilians University in Garching near Munich, Germany.

Nonlinear optical frequency conversion techniques are not only suitable for the generation of short-wavelength radiation but can also be utilized to reach the infrared and terahertz (THz) spectral ranges. For the latter, optical rectification is a suitable technique. THz radiation can be used to access degrees of freedom in matter with low excitation energies. THz pulses with extremely high energy and field strength are enabling novel applications, such as the resonant control over ionic motion, bound and free electrons, as well as nonresonant and strong-field interactions. Intense THz pulses hold promise for the development of a new generation of compact particle and X-ray sources. Laser- and THz-driven particle accelerators with unprecedented flexibility can be important for free-electron lasers and materials science, and can revolutionize medical therapy with X-ray, electron, or proton beams.

Another main goal of the work presented here was to develop intense THz sources based on optical rectification, using optical pump pulses with tilted intensity front for phase matching. This research was motivated by enabling new applications in high-field THz science, such as THz-driven particle acceleration, or resonant and nonresonant control of matter. The work related to the generation and application of intense THz pulses was mainly carried out at the University of Pécs and the MTA-PTE High-Field Terahertz Research Group, in close collaboration with a number of other institutes and industrial partners.

The structure of the dissertation is as follows. Part II is devoted to a brief description of the scientific background. Part III presents the scientific achievements. Part IV is the summary of the work, formulated in thesis points. The acknowledgement and the list of references are given at the end. English language has been chosen in order to enable not only Hungarian but also foreign students and colleagues to use the dissertation as an introduction to the topic and to serves as a source for background information on this research.

II. Scientific background

The advent of ultrafast solid-state lasers pumped by efficient laser diodes lead to a technological breakthrough and had a transformative impact on many areas of science, which is hard to overestimate. Ultrashort light pulses down to few-cycle pulse durations can be generated by compact solid-state laser oscillators, which utilize Kerr lens mode locking, a technique based on a third-order nonlinear optical process. Nonlinear optical processes also provide essential tools both for the generation of high-power few-cycle pulses as well as to extend the spectral range accessible by laser sources. *The very basics of nonlinear optics are summarized in Section 1.*

Weak ultrashort pulses, delivered for example by a Ti:sapphire laser oscillator, can be amplified to TW–PW power levels by chirped-pulse amplification (CPA) without the risk of optical damage. However, it is challenging to achieve high peak power with laser amplification while simultaneously maintaining few-cycle pulse duration. An alternative route is offered by optical parametric amplification (OPA), a second-order nonlinear optical process. Combining OPA with CPA, a technology called optical parametric chirped-pulse amplification (OPCPA), enables to amplify few-cycle pulses to unprecedented peak powers. *Some basic features of the OPA process are summarized in Section 2.*

Various laser sources can emit radiation in the THz spectral range [2]. Examples are molecular gas lasers involving transitions between rotational levels, the p-type germanium laser, the quantum-cascade laser, or the free-electron laser. These lasers typically emit continuous-wave radiation or many-cycle pulses. Optical rectification (OR), another second-order nonlinear optical process, can be used to generate long-wavelength radiation in the infrared and THz spectral range. Single-cycle THz pulses can be generated by OR when pumped by femtosecond lasers pulses. *The fundamentals of THz pulse generation by OR are summarized in Section 3. A few examples of novel application possibilities are also given.*

1. Nonlinear optical interactions

A sufficiently strong optical field can modify the optical properties of a material system. In such a case the response of a material system to the applied optical field depends in a nonlinear manner on the strength of the optical field [3]. Historically, the discovery of second-harmonic generation (SHG) by Franken et al. in 1961, shortly after the demonstration of the first working laser, marked the beginning of the field of nonlinear optics. Typically, only laser light is sufficiently intense to significantly modify the optical properties of materials.

The effect of an external electric field **E** on the medium can be described by the time-dependent average density of the induced (atomic or molecular) electric dipole moments in the medium, $\mathbf{P}(\mathbf{E})$. For small field strengths the dependence of the induced polarization in a medium on the electric field is linear:

$$\mathbf{P}(\mathbf{E}) = \varepsilon_0 \chi^{(1)} \mathbf{E} = \mathbf{P}^{(1)}. \tag{II.1}$$

In general, the linear susceptibility $\chi^{(1)}$ is a second-rank tensor and it can be frequency dependent. ε_0 is the electric permittivity of free space. For higher field strengths, the material response to the applied field may become nonlinear, which can be described by a Taylor-series expansion:

$$\begin{aligned} \mathbf{P}(\mathbf{E}) &= \varepsilon_0 \left(\chi^{(1)} \mathbf{E} + \chi^{(2)} \mathbf{E}\mathbf{E} + \chi^{(3)} \mathbf{E}\mathbf{E}\mathbf{E} + \cdots \right) \\ &= \mathbf{P}^{(1)} + \mathbf{P}^{(2)} + \mathbf{P}^{(3)} + \cdots \\ &= \mathbf{P}^{(1)} + \mathbf{P}^{\mathrm{NL}}. \end{aligned} \tag{II.2}$$

Here $\chi^{(n)}$ is the n^{th}-order nonlinear susceptibility, a tensor of rank $n+1$.

During propagation of a light beam in a medium with nonlinear response new frequency components can be generated which were not contained in the input. Let us consider a nonlinear medium with second-order nonlinear susceptibility $\chi^{(2)}$ and an input field which contains two distinct frequency components:

$$E(t) = \frac{1}{2} \hat{E}_1 e^{i\omega_1 t} + \frac{1}{2} \hat{E}_2 e^{i\omega_2 t} + \text{c.c.} \tag{II.3}$$

For the sake of simplicity, the vector notation has been dropped here and only the time dependence of the electric field is considered. The second-order nonlinear response is given as follows:

$$\begin{aligned} P^{(2)}(t) &= \varepsilon_0 \chi^{(2)} EE \\ &= \frac{1}{4} \varepsilon_0 \chi^{(2)} \big[\hat{E}_1^2 e^{i2\omega_1 t} + \hat{E}_2^2 e^{i2\omega_2 t} + 2\hat{E}_1 \hat{E}_2 e^{i(\omega_1+\omega_2)t} \\ &\qquad + 2\hat{E}_1 \hat{E}_2^* e^{i(\omega_1-\omega_2)t} + 2\hat{E}_1 \hat{E}_1^* \big] + \text{c.c.} \end{aligned} \tag{II.4}$$

The first two terms describe SHG of both frequency components. The further terms describe sum-frequency generation (SFG), difference-frequency generation (DFG), and OR, respectively. Here, the latter is a static (DC) field.

In the more general case, the field can be composed of several monochromatic components ω_n with slowly-varying amplitudes $\tilde{\mathbf{E}}_n(\mathbf{r})$:

$$\mathbf{E}(\mathbf{r},t)=\frac{1}{2}\sum_{n}\tilde{\mathbf{E}}_n(\mathbf{r})e^{i(\omega_n t-\mathbf{k}_n\mathbf{r})}+\text{c.c.} \tag{II.5}$$

The induced nonlinear polarization can be written as follows:

$$\mathbf{P}^{\mathrm{NL}}(\mathbf{r},t)=\frac{1}{2}\sum_{n}\tilde{\mathbf{P}}_n^{\mathrm{NL}}(\mathbf{r})e^{i(\omega_n t-\mathbf{k}_n\mathbf{r})}+\text{c. c.} \tag{II.6}$$

For waves propagating in the z-direction with negligible diffraction one obtains the following coupled wave equations:

$$\frac{\partial}{\partial z}\tilde{\mathbf{E}}_n(z)=-i\frac{\omega_n}{2c\varepsilon_0 n_n}\tilde{\mathbf{P}}_n^{\mathrm{NL}}(z), \tag{II.7}$$

where $n_n=n(\omega_n)$ is the refractive index. This is the simplest form of the coupled wave equations in nonlinear optics. It shows that $\tilde{\mathbf{E}}_n$ will grow at a maximal rate if the polarization wave has a phase lead of π/2 with respect to the field (i.e. the arguments of $\tilde{\mathbf{P}}_n^{\mathrm{NL}}$ and $i\tilde{\mathbf{E}}_n$ are the same). If the sign of the phase difference is reversed (a phase lag of π/2), the field will decay at a maximal rate. If the polarization and field are in phase, the amplitude of the field will be unchanged, but its phase will change under propagation, meaning a modification of the refractive index.

In many practical situations, a measurable output field can be generated usually at just one or some of all possible new frequencies. The reason is that a fixed phase relationship (phase matching, see below) should be maintained during the propagation, which cannot be fulfilled simultaneously for all possible frequency combinations. Therefore, in the simplest situation when dealing with second-order nonlinear processes, it is sufficient to consider the interaction of three waves coupled by the nonlinear polarization (three-wave mixing). For their frequencies $\omega_1\le\omega_2\le\omega_3$ energy conservation requires

$$\omega_3=\omega_1+\omega_2. \tag{II.8}$$

Of particular interest for this work are OPA and OR, specific cases of three-wave mixing, which differ in initial conditions. OR is a special case with $\omega_3\approx\omega_2$ and $\omega_1\ll\omega_2,\omega_3$. The coupled wave equations take the following form for three-wave mixing:

$$\begin{aligned}
\frac{\partial}{\partial z}\tilde{\mathbf{E}}_1(z)&=-i\frac{\omega_1}{2cn_1}\chi^{(2)}\tilde{\mathbf{E}}_3(z)\tilde{\mathbf{E}}_2^{*}(z)e^{-i\Delta kz},\\
\frac{\partial}{\partial z}\tilde{\mathbf{E}}_2(z)&=-i\frac{\omega_2}{2cn_2}\chi^{(2)}\tilde{\mathbf{E}}_3(z)\tilde{\mathbf{E}}_1^{*}(z)e^{-i\Delta kz},\\
\frac{\partial}{\partial z}\tilde{\mathbf{E}}_3(z)&=-i\frac{\omega_3}{2cn_3}\chi^{(2)}\tilde{\mathbf{E}}_1(z)\tilde{\mathbf{E}}_2(z)e^{i\Delta kz}.
\end{aligned} \tag{II.9}$$

The phase mismatch parameter is defined as $\Delta k=k_3-k_2-k_1$.

It is instructive to introduce the modified field variables $\tilde{A}_i=\sqrt{n_i/\omega_i}\,\tilde{E}_i$ $(i=1,2,3)$, where the vector notation has been dropped for simplicity. With these, the coupled wave equations take the following simpler form:

$$\begin{aligned}\frac{\partial \tilde{A}_1}{\partial z} &= -i\,\eta \tilde{A}_3 \tilde{A}_2^* e^{-i\Delta kz},\\ \frac{\partial \tilde{A}_2}{\partial z} &= -i\,\eta \tilde{A}_3 \tilde{A}_1^* e^{-i\Delta kz},\\ \frac{\partial \tilde{A}_3}{\partial z} &= -i\,\eta \tilde{A}_1 \tilde{A}_2 e^{i\Delta kz}.\end{aligned} \qquad \text{(II.10)}$$

The advantage is that the same coupling coefficient $\eta = \left(\chi^{(2)}/2c\right)\sqrt{\omega_3\omega_2\omega_1/(n_3n_2n_1)}$ can be used in all three equations. $\left|\tilde{A}_i\right|^2$ is proportional to the photon current density: $\Phi_i = I_i/\hbar\omega_i = (c\varepsilon_0/2\hbar)\left|\tilde{A}_i\right|^2$ $(i = 1,2,3)$.

2. Optical parametric amplification

Few-cycle laser pulses with unprecedented peak powers are crucial for the investigation of laser-driven strong-field phenomena [4], having become an accessible field of research with the advent of suitable laser systems. Conventional laser-amplification technology can provide very high power levels, but the pulse duration determined by the laser material is limited to the tens-of-femtosecond range. The technique of OPA, which allows for very large amplification bandwidths, has opened up a new path towards generating few-cycle pulses with unprecedented peak powers [5-13].

In OPA amplification takes place in a nonlinear optical crystal. OPA can be viewed as DFG with special initial conditions, where a weak input beam (the seed) with the frequency ω_1 or ω_2 is being amplified with the help of a strong pump beam of frequency ω_3, which is being depleted. The pump beam has the highest frequency: $\omega_1 \leq \omega_2 < \omega_3$. The field with the medium frequency is usually called the signal and that with the smallest frequency the idler. At degeneracy, these two frequencies are equal. Typically, the idler field is not present in the input, but it is generated during OPA. Both signal and idler are amplified in the OPA process. In the simplest cases, Equations (II.9) or (II.10) can be used to describe the OPA process. The description of broadband amplification with short pulses requires more sophisticated models, taking into account the different group velocities of the interacting pulses [14], material dispersion, and possibly third-order cross- and self-phase modulation effects [15].

In OPA, phase-matching in a non-collinear geometry (Figure 1) allows for extremely large amplification bandwidths [5], which can be significantly larger than that of any known laser medium. This enables the amplification of broadband seed pulses using relatively narrowband pump pulses delivered by conventional laser amplification technology. The gain can be very high even in a short length of material, which results in a lower B-integral (the accumulation of nonlinear phase by passing through material). Furthermore, in contrast to laser amplifiers, essentially no energy is converted into heat, thereby eliminating thermal distortions of the beam.

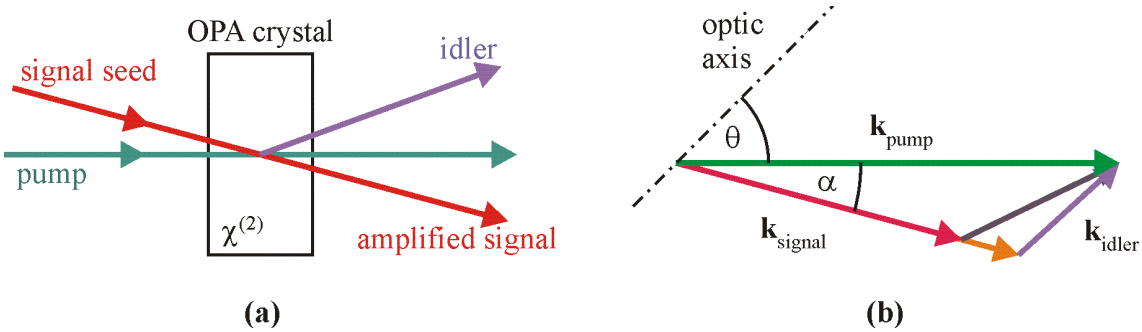

Figure 1. (a) Scheme of noncollinear OPA. (b) Phase matching in a noncollinear OPA.

In order to reach the highest possible peak intensities, in high-power systems OPA is usually combined with CPA, called optical parametric chirped-pulse amplification (OPCPA, Figure 2), a scheme first proposed by Dubietis et al. [16]. In such a system, pulse energies as high as 35 J were achieved in 84-fs pulses [17]. In the few-cycle regime 10-fs pulses with 90 mJ energy were demonstrated from an OPCPA system [18]. In typical ultrabroadband OPCPA systems the duration of pump pulses obtained from a

Nd:YAG laser are usually on the order of 100 ps [11, 12, 18]. Some smaller-scale systems use shorter pump pulses of ~100 fs duration and were able to generate sub-10-fs pulse durations, however, only with energies in the μJ range [8-10, 19-21]. 300 μJ output pulse energy has been reported from an OPCPA system [22] pumped by 150-fs pulses, however, the signal pulse duration was about 20 fs. Novel concepts and perspectives to reach high average and peak powers simultaneously are summarized in the review article Ref. [23].

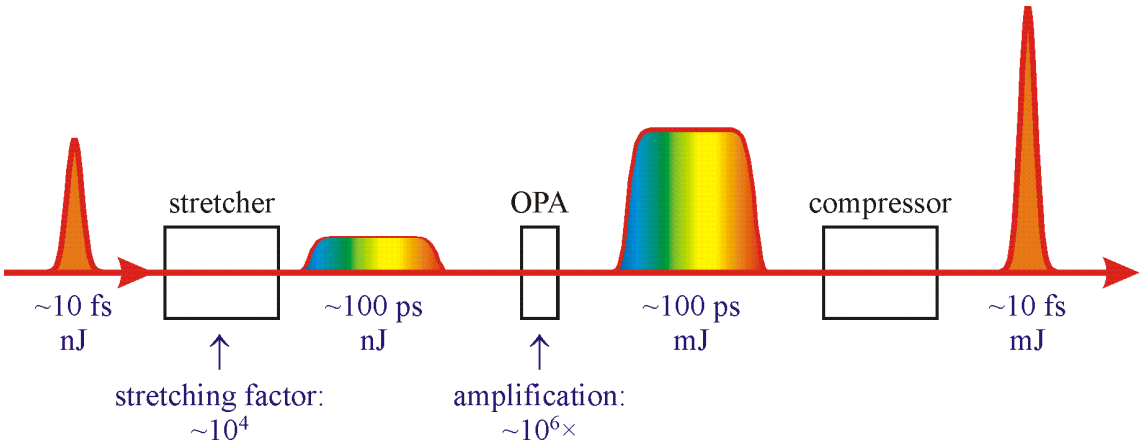

Figure 2. Scheme of a typical OPCPA system for generating few-cycle pulses.

3. Generation and applications of THz pulses

The widespread availability of table-top laser sources triggered the development of various types of laser-driven pulsed THz sources. This development now enables to routinely provide THz pulses with unprecedented energies as well as peak electric and magnetic field strengths throughout the entire THz spectral range [24]. Different laser-based THz generation techniques can be used to access different parts of the THz spectral range extending from 0.1 THz to 10 THz (1 THz = 10^{12} Hz). Some of the recently developed technologies enable to generate radiation with even larger bandwidth or tuning range up to 100 THz and beyond, which lead to an extension of what is called the THz spectral range. An overview of the approximate spectral coverage and the achieved highest pulse energies of various technologies is given in Figure 3.

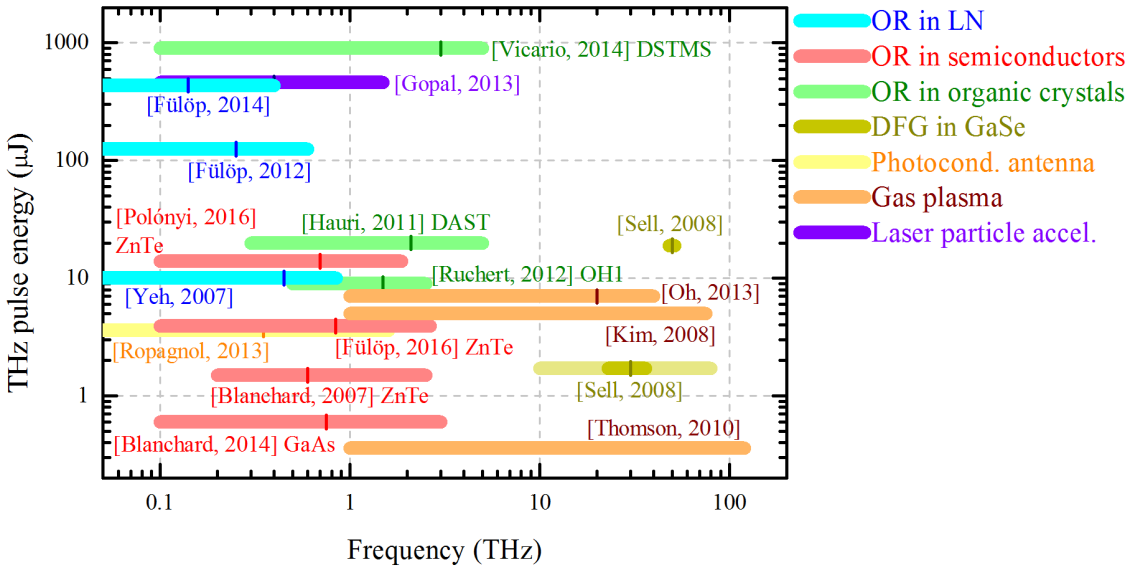

Figure 3. Some of the highest reported experimental values of THz pulse energy and approximate spectral coverage for various types of pulsed THz sources. The short vertical lines indicate the approximate frequencies of the spectral peaks. LN: $LiNbO_3$.

Sources driven by femtosecond laser pulses are capable of delivering single-cycle or nearly-single-cycle THz pulses with energies on the μJ–mJ level and MV/cm peak electric field strengths. In the low-frequency part of the THz range (about 0.1–2 THz), it is mainly OR in lithium niobate ($LiNbO_3$, LN) and in different semiconductors which can be used to provide intense pulses. At medium frequencies (about 1–20 THz), organic crystal have been proven to be very efficient. Multi-cycle pulses at higher frequencies (10–70 THz) can be generated by DFG in GaSe. Extremely large bandwidths covering the entire range of 1 to 100 THz or even beyond could be achieved with two-color laser-plasma sources.

As a result of the development in source technology, intense THz pulses have proven significant discovery and application potential. This relies on their interaction with various degrees of freedom in matter [25, 26], including (i) nuclear dynamics with ions (acceleration [27]), molecules (vibration and rotation [28]), and condensed matter (lattice vibrations [29]); (ii) spin [30]; and (iii) electrons (excitations of electron-hole pairs [31], Cooper pairs, electron acceleration [32]). Some of the new applications are highlighted in Section 3.4, with emphasis on charged-particle acceleration and manipulation.

3.1. THz generation by optical rectification

The generation of THz radiation, called far-infrared at that time, in electro-optical materials was investigated as early as 1971 [33, 34]. Generation of nearly single-cycle THz pulses by OR was first demonstrated by Auston et al. in 1984 [35].

OR, a second-order nonlinear optical process, is a special case of DFG [3]. A femtosecond optical pulse can be used to drive OR. Spectral components with angular frequencies ω and $\omega + \Omega$ from the optical pulse can combine by DFG to generate a new spectral component with the angular frequency Ω (Figure 4). Thus, OR can be described as intra-pulse DFG, as opposed to inter-pulse DFG with two input pulses (which may have different carrier frequencies). The nonlinear polarization induced by the pump pulse can be calculated as [36]

$$P_{\mathrm{NL}}(\Omega) = \varepsilon_0 \chi^{(2)} \int_0^{\infty} E(\omega + \Omega) E^*(\omega) d\omega, \tag{II.11}$$

where ε_0 is the permittivity of free space, $\chi^{(2)}$ is the second-order nonlinear susceptibility of the medium, $E(\omega)$ is the one-sided ($\omega > 0$) Fourier-component of the pump pulse, ω is the optical frequency, and Ω is the difference frequency. Typical optical pump pulse durations used for OR range from about 30 fs to 1.5 ps. Accordingly, the generated difference frequency spectral components are in the THz range. According to Equation (II.11), a narrowband pump pulse generates low THz frequencies, while a broadband pulse can generate a broad THz spectrum containing also higher THz frequencies.

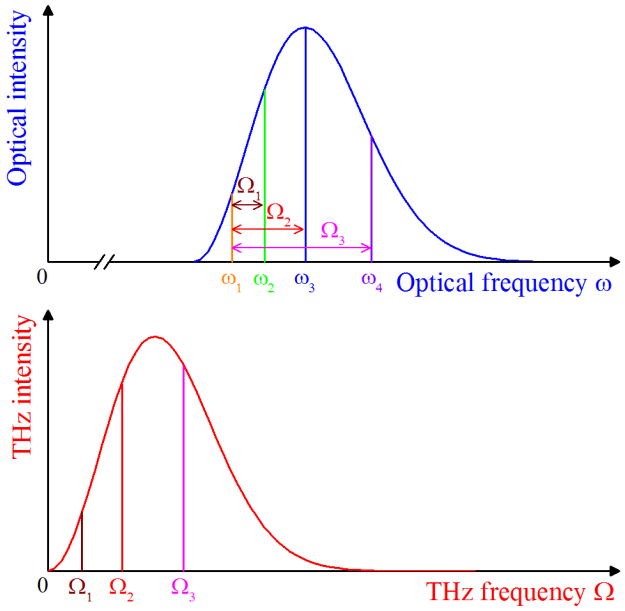

Figure 4. Schematic representation of optical and THz spectra in case of OR. Pairs of optical frequency components (upper panel, note the horizontal axis break) generate a THz spectral components at their difference frequencies (lower panel).

The build-up of the THz field over macroscopic distances in the medium can be described by the coupled wave equations (II.9) or (II.10) [3]. In many cases, when the generated THz field is weak, the optical-frequency fields can be regarded as constant and

only the equation for the THz field needs to be retained. Besides the nonlinear polarization, OR is also influenced by the dispersion of the medium. The efficiency of OR is highest when the phase matching condition, $\Delta\mathbf{k} = 0$, is fulfilled [3, 36, 37], where

$$\Delta\mathbf{k} = \mathbf{k}(\Omega) + \mathbf{k}(\omega) - \mathbf{k}(\omega + \Omega) \approx \mathbf{k}(\Omega) - \left.\frac{\partial\mathbf{k}}{\partial\omega}\right|_{\omega_0} \cdot \Omega. \tag{II.12}$$

The second, approximate equation holds if $\Omega \ll \omega$, which is usually valid for THz generation by OR. In case of collinear phase matching, Equation (II.12) gives $\Delta k = |\Delta\mathbf{k}| = \left[n(\Omega) - n_\mathrm{g}(\omega_0)\right] \cdot \Omega/c$. Here, ω_0 is the pump central (carrier) frequency, c is the speed of light in vacuum, n and n_g are the refractive and group indices, respectively. Thus, in case of phase matching, the phase velocity of the generated THz radiation, $v = c/n$, equals the group velocity of the optical pump pulse, $v_\mathrm{g} = c/n_\mathrm{g}$, and the following velocity matching condition holds:

$$v(\Omega) = v_\mathrm{g}(\omega_0). \tag{II.13}$$

Materials suitable for OR are semiconductors such as CdTe, GaAs, GaP, GaSe, or ZnTe, ferroelectric materials such as LN or lithium tantalate ($LiTaO_3$), and organic materials such as DAST, OH1, DSTMS, or HMQ-TMS. Their properties are briefly described in Section 3.3, more details can be found in the literature [24, 38-42]. For the selection of a suitable material it is instructive to consider the expression for the THz generation efficiency in case of phase matching [37]:

$$\eta(\Omega) = \frac{2\Omega^2 d_\mathrm{eff}^2 L^2 I}{\varepsilon_0 c^3 n^2(\omega_0) n(\Omega)} \cdot e^{-\frac{1}{2}\alpha(\Omega)L} \cdot \frac{\sinh^2\left[\frac{1}{4}\alpha(\Omega)L\right]}{\left[\frac{1}{4}\alpha(\Omega)L\right]^2}. \tag{II.14}$$

Here, L is the material length and I is the pump intensity. Obviously, a large effective nonlinear coefficient, d_eff, and a small THz absorption coefficient, $\alpha(\Omega)$, is advantageous for a high efficiency. The scaling of the efficiency with the square of the THz frequency enables significantly higher efficiencies at higher THz frequencies and makes it challenging to achieve comparable values at low THz frequencies. An important property of OR is that a carrier-envelope phase stable pulse is generated when driven by an optical pulse. Carrier-envelope phase stability is essential in many field-driven applications (see Section 3.4).

It is worth to mention that Wynne and Carey gave an integrated description of THz generation driven by a laser pulse travelling through the medium and inducing a polarization oscillating at THz frequencies [43]. This description is valid for various mechanisms, such as OR, microscopic currents from photoinduced charge transfer in aligned molecules, and current surge (photoconductive antennas). In the simplest case of an instantaneously responding medium, no dispersion in the THz range, and perfect phase matching, the electric field of the THz pulse is shaped as the time derivative of the optical pulse envelope. For Gaussian-like pump pulse envelopes this means that single-cycle THz pulses can be generated.

In a realistic model of intense THz sources, besides OR, usually other effects have also to be taken into account. It is important to consider linear absorption in the THz

range, determined by the complex dielectric function of the material. Absorption of pump light, especially multi-photon absorption, can cause an increased carrier concentration and absorption in the THz range [41, 44]. In case of very strong THz fields, it is important to take into account the influence of the generated THz pulse on the optical pump pulse caused by their nonlinear interaction (sum- and difference-frequency generation between optical and THz fields) [45-47]. At high pump intensities, other nonlinear effects may also occur, such as self-phase modulation, second- and third-harmonic generation, or stimulated Raman scattering. In noncollinear geometries (see Section 3.2), spatio-temporal coupling can lead to additional complexity.

3.2. Tilted-pulse-front pumping

The phase-matching condition, given by Equation (II.13), can be fulfilled in some cases by utilizing the birefringence of the nonlinear material. One example is GaSe. Other semiconductors, such as ZnTe, GaP, or GaAs, are optically isotropic. Here, collinear phase matching is possible only in specific cases, at certain pump and THz frequencies. One example is ZnTe pumped at 0.8 μm wavelength to generate radiation around 1 THz frequency. At other wavelengths or in other materials a specific noncollinear geometry, called tilted-pulse-front pumping (TPFP), may be used for phase matching.

The TPFP technique was proposed by Hebling et al. to enable efficient THz pulse generation in LN [48], a material with high effective nonlinear coefficient but lack of collinear phase matching possibility for OR. Recently, it has also been applied to semiconductors [44, 49-51]. TPFP is of great practical importance, as it is scalable to high THz pulse energies simply by increasing the pumped area. It enables broadband (achromatic) phase matching for OR in a noncollinear geometry involving pump angular dispersion using pump pulses with tilted intensity front [24, 48, 52].

The scheme of TPFP is shown in Figure 5a. The pump pulse propagates with a tilted intensity front inside the nonlinear medium. The tilt angle of the pulse front with respect to the phase fronts is γ. The THz radiation is generated by the induced polarization along the tilted pulse front. Therefore, according to Huygens' principle, the THz radiation propagates perpendicularly to the pump pulse front. A strong THz field can build up if the source (the induced polarization along the pump pulse front), moving with the group velocity $v_g(\omega_0)$, remains in phase with the THz field propagating with the phase velocity $v(\Omega)$. According to Figure 5a, this is fulfilled at the pulse-front tilt (PFT) angle γ satisfying the following velocity matching condition:

$$v(\Omega) = v_g(\omega_0) \cdot \cos\gamma. \tag{II.15}$$

This equation is a more general form of Equation (II.13). It states that the projected pump group velocity needs to match the THz phase velocity. As the pump pulse propagates, it slides along the THz phase front. Obviously, Equation (II.15) can be fulfilled only in materials with a THz phase velocity smaller than, or equal to the pump group velocity.

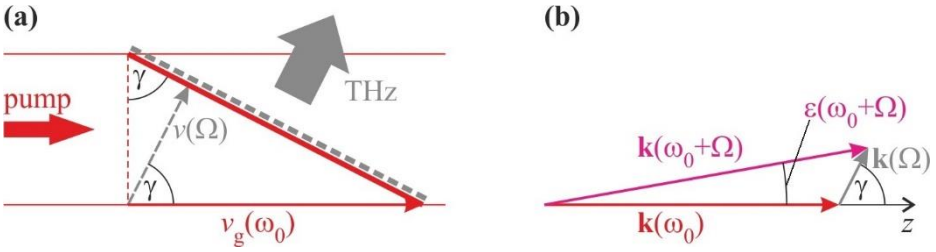

Figure 5. (a) Scheme of TPFP with pump pulse front (thick red solid line) and THz phase front (thick gray dashed line) [24]. (b) Noncollinear phase matching in TPFP.

The TPFP scheme can also be described with wave vectors as noncollinear vector phase matching (Figure 5b). The PFT is linked to angular dispersion according to the relation [48, 52, 53]:

$$\tan\gamma = -\frac{n}{n_g}\lambda\frac{d\varepsilon}{d\lambda}. \tag{II.16}$$

The propagation angles, $\varepsilon(\omega)$, with respect to the beam propagation direction, z, are typically small and for the z-projection of the wave vectors in case of phase matching $k(\Omega)\cos\gamma \approx k(\omega_0+\Omega) - k(\omega_0) \approx \Omega(dk/d\omega)|_{\omega_0}$ is a good approximation. By using the definitions of the wave vector, phase, and group velocities, one can easily obtain from this relation the velocity-matching condition of Equation (II.15).

The angular dispersion present in TPFP schemes contributes to the group velocity dispersion (GVD) [52], in addition to the contribution from material dispersion. The GVD parameter can be written as follows [53, 54]:

$$D = \frac{d\left(v_g^{-1}\right)}{d\lambda} = \frac{\lambda}{c}\left[n\left(\frac{d\varepsilon}{d\lambda}\right)^2 - \frac{d^2n}{d\lambda^2}\right], \tag{II.17}$$

where the first and second terms originate from angular dispersion and material dispersion, respectively. For a large pulse front tilt angle the former can dominate over the latter, thereby significantly enhancing the variation of the pump pulse duration with propagation distance [1]. The influence of GVD, originating from angular dispersion, on THz generation will be discussed for LN in Section 5.1 and for semiconductors in Section 7.1.

3.3. Materials for optical rectification

Materials suitable for OR are ferroelectric materials such as LN or $LiTaO_3$, semiconductors such as CdTe, GaAs, GaP, GaSe, or ZnTe, and organic materials such as DAST, OH1, DSTMS, or HMQ-TMS. Detailed comparison of their properties can be found in the literature [24, 38-42]. Below, a brief description of the properties, most important for OR, of these materials is given.

Lithium niobate

LN is one of the most widely used materials for intense THz sources. Its properties relevant for THz generation by OR are discussed in Refs. [24, 38-41, 55, 56]. The most important features are summarized below:

- LN has a high effective nonlinear coefficient of $d_{\text{eff}} = d_{33} = 168\ \text{pm/V}$. This is higher than typical values for semiconductors, which range from about 25 pm/V to 80 pm/V, but smaller than that of organic materials. In order to utilize d_{33} for OR, both the pump and the THz should be polarized along the dielectric Z axis of LN.
- The THz absorption coefficient is relatively high (about 16 cm^{-1} at 1 THz) at room temperature, but can be significantly reduced (below 5 cm^{-1}) by cooling the crystal to cryogenic temperatures [55]. Phonon absorption limits the useful THz spectral range to the low-frequency part of the THz spectrum (up to about 4.5 THz [39]).
- Even though LN is optically anisotropic, utilizing birefringence for phase matching by angle tuning in OR is not possible below the transverse optical phonon frequency, due to the strong contribution of the lattice vibration to the dielectric function [39]. Owing to the very different optical group and THz phase velocities, a large PFT angle of about 63° is required for phase matching (see Section 3.2).
- It is available in congruent (cLN) and stoichiometric (sLN) forms, where somewhat higher THz generation efficiencies were achieved with the latter. Both types are available in large sizes up to several cm. To prevent photorefractive damage, the strong photorefractive effect can be significantly reduced by doping with MgO. The optimal doping concentration was found to be about 0.7% for sLN and 6% for cLN [57].
- LN can be pumped at high intensities (~100 GW/cm^2) owing to its high damage threshold. Multiphoton absorption (MPA) of the pump usually plays a minor role as the material is insulator with a large bandgap of 3.8 eV. At the typical pump wavelengths of 0.8 μm and 1.03 μm, the lowest order effective MPA is three-photon absorption (3PA) and four-photon absorption (4PA), respectively.

THz generation from LN was demonstrated as early as 1971 [34], however the efficiency was extremely low due to lack of phase matching. It was the introduction of the TPFP technique [48], which enabled more efficient THz pulse generation from this material (empty symbols in Figure 6, see also Figure 3) and the increase of the THz pulse energy by several orders of magnitude [58, 59]. The potential of the technique for high-energy THz pulse generation was demonstrated in subsequent experiments, where 10 μJ [60], 30 μJ [61], and 50 μJ [62] pulse energies were reported with efficiencies of about 0.1% or below. Peak electric field strengths up to 2.1 MV/cm were reported [63, 64]. In these experiments, short pump pulses of about 100 fs were used.

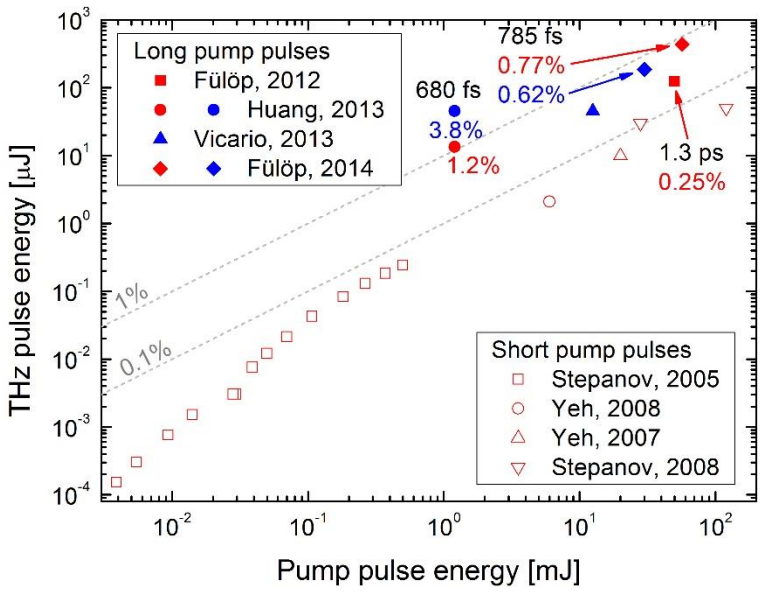

Figure 6. Measured scaling of the THz pulse energy with the pump pulse energy in LN using TPFP for short (about 100 fs) and long (0.5 ps–1.5 ps) pump pulses. Red (blue) symbols: room (cryogenic) crystal temperature. The dashed grey lines indicate the 0.1% and the 1% levels of pump-to-THz energy conversion efficiency.

Semiconductors

Semiconductors are among the most frequently used materials in generation and detection of THz radiation. As THz sources they can constitute the nonlinear optical material for OR, DFG, or OPA. They also form the photoconductive substrate for biased antenna structures (photoconductive antennas). As detectors, semiconductors are applied in electric-field waveform measurement of broadband THz pulses using (unbiased) photoconductive antennas or electro-optic sampling.

Photoconductive antennas are frequently used for low-energy THz sources, especially in linear THz time-domain spectroscopy systems. Large-area photoconductive antennas should be mentioned as alternative sources of intense THz pulses [65-67]. The highest energy demonstrated with this technique was 3.6 μJ using a ZnSe interdigitated large aperture photoconductive antenna [67], corresponding to 143 kV/cm peak electric field with a spectral coverage between 0.05 THz and 1 THz. Limited THz pulse shaping, ranging from a symmetric single-cycle THz pulse to an asymmetric half-cycle THz pulse, was also possible by using a binary phase mask. However, scaling this technology to substantially higher energies and field strengths remained challenging.

THz pulse energies on the order of 1 μJ were demonstrated both with OR [49, 68] and OPA [69]. Multicycle THz pulses at multi-10-THz frequencies were generated with energies up to 19 μJ by DFG [70]. Recent development indicates that OR will expectedly be scalable to substantially higher, mJ-level energies [50, 51, 71]. This is discussed in more detail in Section 7.

Important properties of semiconductors relevant for THz generation by OR are compiled in Refs. [24, 38-41, 56]. In brief, the main features are:

- Semiconductors possess nonlinear coefficients smaller than that of LN and organic crystals, typically falling into the range of 25 pm to 80 pm/V.

- The absorption coefficient of some semiconductors in the THz range is smaller than that of LN or organic crystals. This can partially compensate for their smaller nonlinearity. Semiconductors with higher phonon frequency can enable the generation of higher THz frequencies, such as GaP up to about 7 THz [39, 72].
- Many semiconductors (for example CdTe, GaAs, GaP, ZnTe) are optically isotropic. In some cases, collinear phase matching for OR is fulfilled at a specific pump wavelength. Examples are ZnTe pumped around 0.8 μm, GaP pumped around 1 μm, or GaAs pumped around 1.5 μm, where commercially available Ti:sapphire, Yb-doped, or Er-doped pump lasers can be used. At longer pump wavelengths TPFP has to be used for phase matching because the optical group index decreases with increasing wavelength. Birefringent phase matching was utilized in GaSe above the phonon frequency [69, 70].
- At common pump wavelengths used for collinear phase matching, semiconductors exhibit two-photon absorption (2PA). The resulting increased free-carrier absorption (FCA) leads to a strong limitation of the maximum useful pump intensity and of the achievable THz generation efficiency. Longer pump wavelengths with only higher-order effective MPA can provide a solution. The issue of MPA is discussed in more detail in Section 7.

Organic crystals

Recently, organic crystals have gained increasing attention for the generation of intense THz pulses. Organic THz emitters (DAST [73-77], DSTMS [77-79], OH1 [77, 80], HMQ-TMS [42], etc.) can provide high laser-to-THz conversion efficiencies at room temperature and octave-spanning, or even multi-octave THz spectra. They have the largest nonlinear coefficients among materials used for OR. In case of DAST (Figure 7), for example, it is $d_{\text{eff}} = 615$ pm/V [40, 81]. Organic crystals are best suited for accessing the mid-frequency (1 THz–20 THz) part of the THz range [75, 82].

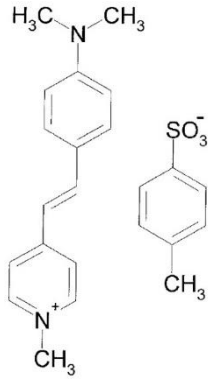

Figure 7. Chemical structure of the organic salt 4-N, N-dimethylamino-4'-N'-methyl-stilbazolium tosylate (DAST). From Ref. [83].

For phase matching they typically require infrared pump wavelengths in the 1.2 μm to 1.6 μm spectral range (Figure 8), where a collinear geometry can be used for THz generation. Phase matching at the 0.8 μm wavelength of Ti:sapphire lasers is usually possible only at low frequencies below 1 THz. Organic crystals typically have several phonon absorption bands in the mid-frequency THz spectral range. Owing to the associated anomalous dispersion of the THz refractive index this can enable simultaneous

phase matching in different THz spectral bands, which are separated by absorption bands. The complicated phase matching behaviour is illustrated in Figure 8a, showing the coherence length for OR in HMQ-TMS [82]. In consequence, the spectral intensity (Figure 8b) and phase structure of the generated THz pulses becomes complex, often leading to multi-cycle waveforms. Varying the pump wavelength was utilized for controlling the spectral coverage of the generated THz pulses (Figure 8b) [82].

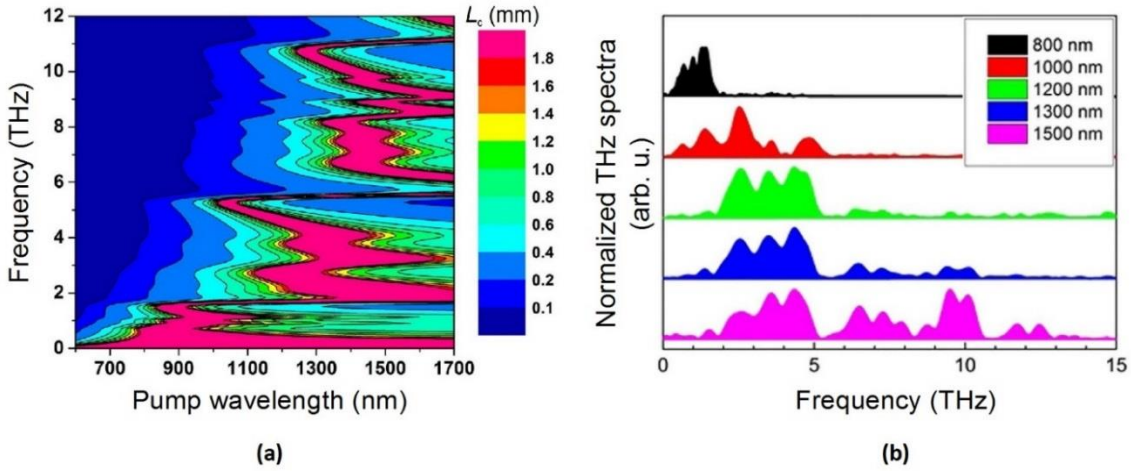

Figure 8. (a) Coherence length $L_c = \pi/\Delta k$ for HMQ-TMS as function of optical pump wavelength and THz frequency. (b) Experimentally recorded THz spectra for various pump wavelengths. From Ref. [82].

Owing to the collinear phase matching geometry, the generated THz radiation is naturally collimated, enabling a good focusability of the beam for achieving high field strengths. High-power single-cycle THz pulses at a central frequency of 2.1 THz with 1 MV/cm electric and 0.3 T magnetic field strengths in focus were demonstrated by OR in DAST pumped with 1-mJ signal pulses of an infrared OPA [76]. The pump-to-THz conversion efficiency was as high as 2%.

White-light seeded OPAs are unfavourable for pumping THz generation in organic crystals because of their low optical-to-optical conversion efficiency, the often irregular beam profile containing hot spots, and the large shot-to-shot energy fluctuation. These features limit the maximum usable pump fluence and can result in unstable THz emission [77, 79]. Cr:forsterite lasers, operating around 1.25 μm wavelength, enable efficient direct pumping of organic crystals. Larger than 10 MV/cm electric and 3 T magnetic field strengths were achieved with up to 3% efficiency by using such a laser to pump different organic crystals [77].

Possible limitations of the crystal size can be overcome by using partitioned crystals [74, 79]. High-field THz transients were reported with as high as 0.9 mJ energy, produced in a 400-mm^2 partitioned DSTMS crystal by OR of 30-mJ laser pulses, delivered by a Cr:forsterite laser [78]. The frequency range covered was between 0.1 THz and 5 THz. The peak THz electric and magnetic field was 42 MV/cm and 14 T, respectively. The conversion efficiency was as high as 3%.

3.4. Applications of THz pulses

The great majority of previous investigations conducted with weak THz sources was restricted to a passive probing of matter using, for example, linear THz spectroscopy. The recent development of intense THz sources enabled to reach unprecedented electric and magnetic field strengths throughout the THz spectrum. Intense THz pulses with peak electric field strength on the 0.1 MV/cm to 1 MV/cm scale enabled a more active role: It became possible to initiate changes in matter and to trace the induced dynamics with THz pump—THz probe [84] or THz pump—optical probe spectroscopy. Resonant and non-resonant control of ionic, electronic, and spin degrees of freedom in a great variety of materials and structures could be demonstrated [30, 85]. Recent reviews on nonlinear light-matter interaction at THz frequencies can be found for example in Refs. [25, 26].

Nonlinear electronic response induced by THz pulses has been studied in Rydberg atoms [66], where the motion of an electronic charge across a distance of the order of 1 nm (the approximate radius of a Rydberg atom) results in extremely large transition dipole moments. The nonlinear THz response and ultrafast carrier dynamics in semiconductors was extensively studied [31, 84-87]. Coherent THz emission was observed in *n*-type GaAs excited by intense THz pulses [85]. The emitted THz field was due to stimulated emission from impurities having a populated excited state and an unpopulated ground state (inversion). Carrier heating and impact ionization dynamics in the low-band-gap semiconductor InSb was observed by THz pump—THz probe spectroscopy [84]. The strong saturation of FCA in *n*-type semiconductors and nonequilibrium carrier distribution were revealed and investigated by using the same technique [87] (Figure 9). High-field single-cycle THz pulses were used for bidirectional ultrafast electric-field gating of interlayer charge transport in a cuprate superconductor [88]. In the studies mentioned above, THz pulses with peak electric field strengths up to about 150 kV/cm were used. Highly nonlinear THz light-matter interaction in single-walled carbon nanotubes was investigated by THz pump—optical probe spectroscopy [89]. The high peak electric field of 0.7 MV/cm and the low effective mass of carriers resulted in ponderomotive energies exceeding the bandgap and in interband excitation, although the THz photon energy (4 meV) was much smaller than the bandgap (1 eV).

Lattice-based THz-induced nonlinear response was investigated in ferroelectric crystals [90, 91]. Ferroelectric materials can be switched between two different domain orientations, indicating the significant anharmonicity associated with the double-well lattice potential and the barrier between the wells. Because of lattice anharmonicity the nonlinear coefficient can be much larger in the THz domain than in the optical range. For example, about three orders of magnitude larger nonlinear refractive index (n_2) was estimated for LN in the THz range than in the visible [90, 92]. Intense THz pulses were used to impulsively drive the ferroelectric soft mode in a $SrTiO_3$ thin film to a large amplitude and enabled the exploration of intrinsic quartic anharmonicity [93] (Figure 10). As the THz electric field increased, the soft-mode absorption peak exhibited blueshifting and spectral narrowing. A classical anharmonic oscillator model suggested that the induced displacement is comparable to that of the ferroelectric phase transition. This indicates that THz coherent control over macroscopic order can also become possible.

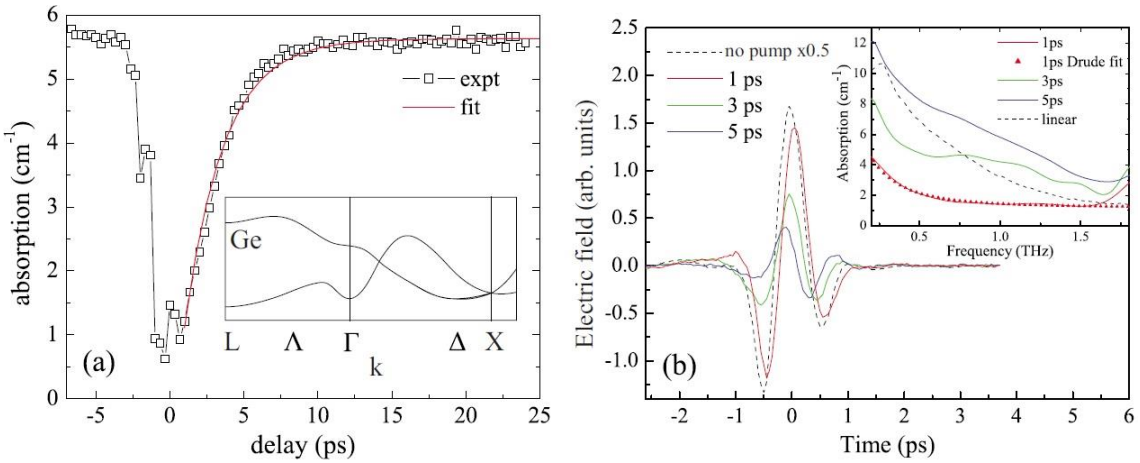

Figure 9. THz pump—THz probe spectroscopy of Ge. (a) Spectrally averaged probe-pulse absorption as function of the THz probe delay for Ge. The inset shows the schematic illustration of the conduction-band structure. (b) The incident (black dotted line) and transmitted THz probe-pulse waveforms for Ge for 1 ps, 3 ps, and 5 ps probe delays, respectively. The inset shows the corresponding absorption spectra, the linear absorption spectrum (black dotted line), and a fit to the sum of two Drude-type components at 1 ps (red triangles). From Ref. [87].

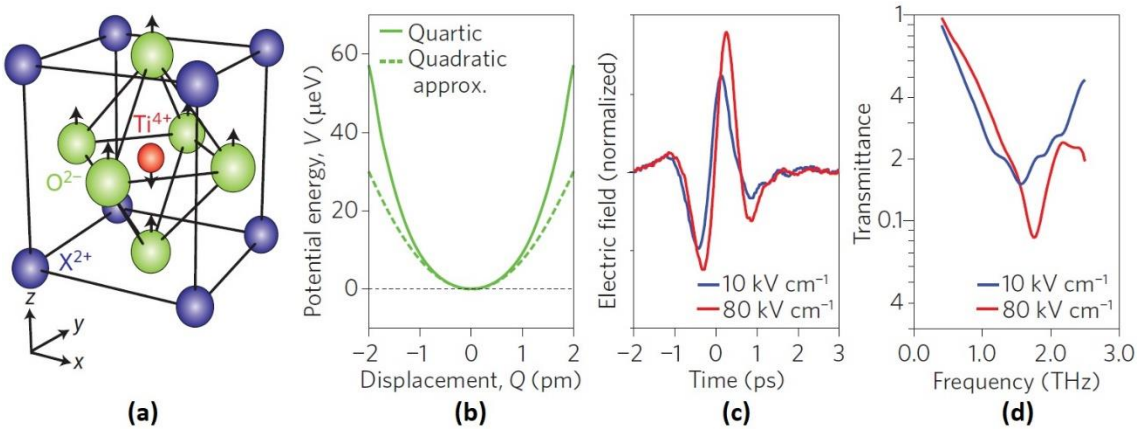

Figure 10. Investigation of lattice anharmonicity in $SrTiO_3$. (a) Schematic representation of the perovskite crystal structure and the soft-mode oscillation in $SrTiO_3$ (X = Sr). (b) Potential $V(Q)$ of the soft mode as a function of the Ti^{4+} ion displacement Q. (c) Transmitted THz waveforms after traversing a $SrTiO_3$ thin film for low (blue) and high (red) incident field amplitudes. (d) Resulting sample transmittances for weak and strong THz excitations. The stiffening of the soft mode with increasing vibrational amplitude is indicated by the shift of the resonance to a higher frequency. From Refs. [25, 93].

Efficient manipulation of charged particles and their (relativistic) beams requires THz field strengths on the order of 1 MV/cm to 10 MV/cm, or even up to the 100 MV/cm level. Today's cutting-edge THz sources can provide such field strengths. The enhancement of attosecond-pulse generation by manipulating laser-ionized electron trajectories in high-harmonic generation in gases has been proposed [94-97]. Electron acceleration, undulation, deflection, and spatial as well as temporal focusing with THz fields is becoming possible [98] and will expectedly lead to important practical applications.

Using THz radiation in such applications can be superior to microwave radiation since THz pulses can be generated with significantly smaller temporal jitter to the electron bunch to be manipulated as compared to microwave pulses. Furthermore, the achievable accelerating gradient is limited by microwave-induced plasma breakdown, where the

threshold surface electric field (E_s) scales with frequency ν and pulse duration τ as $E_s \propto \sqrt{\nu}/\sqrt[4]{\tau}$ (see Ref. [32] and references therein). Clearly, higher frequencies and shorter pulses are beneficial for a higher accelerating gradient.

GeV/m accelerating gradients can be achieved by wakefield acceleration in laser plasma driven by TW–PW scale lasers. However, this technique is susceptible to instabilities. Direct acceleration by intense optical fields is also possible. However, due to the short optical wavelength, it is challenging to achieve a sufficiently precise synchronization of the electron bunch to the laser field and the bunch charge is also limited. Contrary to optical pulses, the much longer wavelength of THz pulses fits well to typical sizes of electron bunches.

THz-driven electron acceleration has been recently demonstrated in a proof-of-principle experiment [32], where 7 keV energy gain in 3 mm was shown in a dielectric-loaded cylindrical metallic waveguide (Figure 11). With more energetic THz pulses, GeV/m accelerating gradient and electron energies on the 10 MeV scale are predicted.

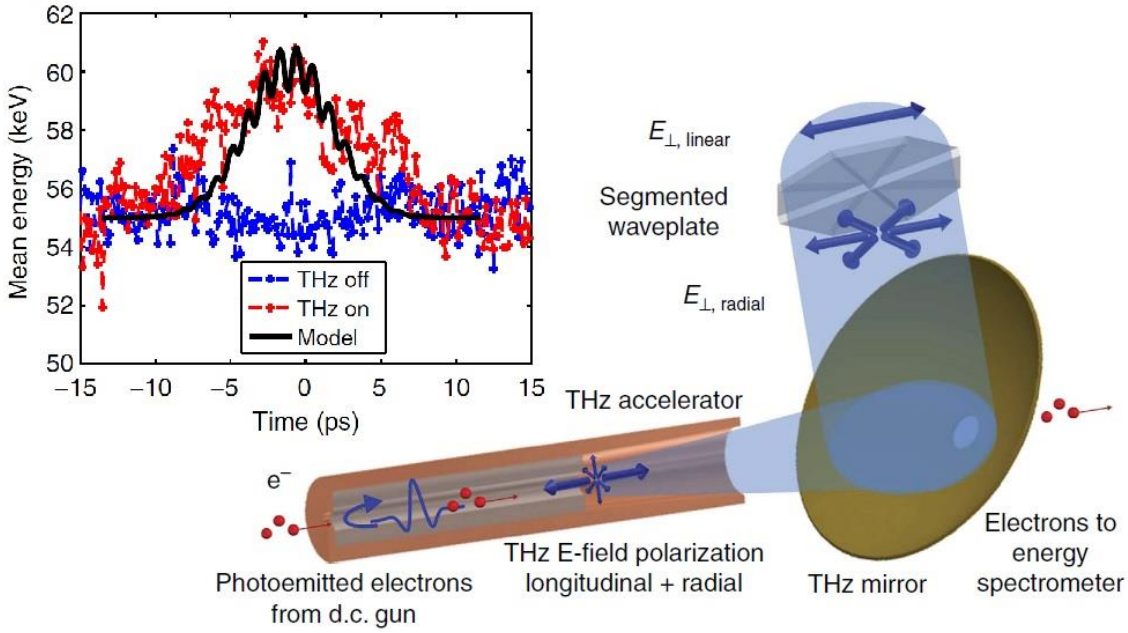

Figure 11. THz-driven linear accelerator. The inset shows the temporal profile of the mean electron energy with (red) and without (blue) THz field. From Ref. [32].

Many applications in materials science require ultrafast electron bunches at tens- or hundreds-of-keV energies. Ultrafast electron microscopy and diffraction can provide atomic-scale (pm) spatial and femtosecond temporal resolution [99]. Few-fs temporal resolution can be achieved with single-electron wavepackets. The generation of ultrafast electron bunches with high charge density requires very large electric field strengths to reduce the space-charge effects in the initial acceleration stage. THz-field driven electron sources can be superior to conventional electron guns in providing higher electron energies from very compact setups up to the (multi-)MeV range, in combination with significantly larger bunch charges, while preserving the short pulse duration. Recently, a THz-driven electron gun was demonstrated with promising scaling potential [100, 101].

Postacceleration of laser-generated proton beams has also been proposed [27]. It utilizes the evanescent field of THz pulses in the vacuum gap between a pair of dielectric

crystals (Figure 12). Laser-driven accelerators produce ion beams with only tens of MeV/nucleon energy at maximum within an extremely broad energy spectrum. It is predicted that the energy of a laser-generated proton bunch can be increased from 40 MeV to 56 MeV in five subsequent THz-driven postaccelerator stages and its initially broad energy distribution can be significantly narrowed down. This holds promise of compact and flexible ion accelerators suitable even for hadron therapy. Medical applications ideally require ion beams with ∼100 MeV/nucleon energy and relative energy fluctuation on the order of 1%. For this application, THz pulses in the 0.1 THz to 0.5 THz frequency range and peak electric field on the MV/cm level are particularly suitable. THz pulses with similar parameters were already demonstrated from a LN source [102]. A THz-driven ion source from a near critical density hydrogen plasma has also been proposed recently [103].

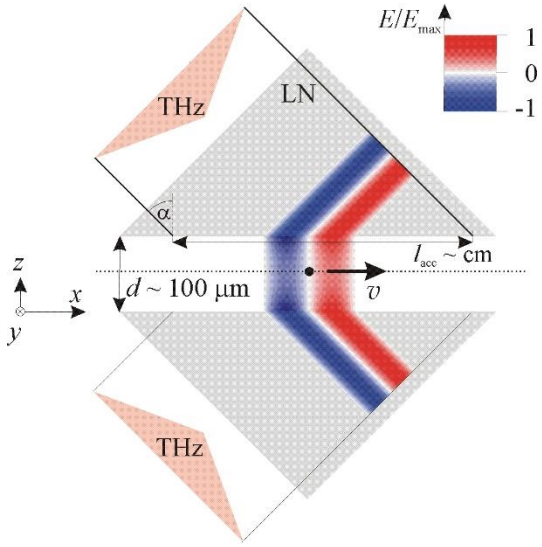

Figure 12. Scheme of the evanescent-wave postaccelerator for laser-generated proton beams. From Ref. [27].

III. Results

In this Chapter, the achieved scientific results are presented.

Section 4 deals with the development of high-power few-cycle pulse sources in the visible—near infrared spectral range. This research was motivated by the quest for suitable primary sources for high-field applications, such as to drive novel attosecond sources or laser-driven electron acceleration.

Section 5 deals with the development of intense THz sources based on optical rectification in $LiNbO_3$, using optical pump pulses with tilted intensity front for phase matching. This research was motivated by new applications in high-field THz science, such as THz-driven particle acceleration, or resonant and nonresonant control of matter.

Section 6 deals with the development of high-average-power THz sources motivated by the need for efficient generation of THz pulses with nJ–μJ pump pulse energies suitable for nonlinear THz spectroscopy or the control of short electron bunches.

Section 7 deals with the development of highly efficient and compact semiconductor THz sources pumped at infrared wavelengths sufficiently long to suppress the pump-induced free-carrier absorption due to lower-order multiphoton absorption of the pump. Such THz sources can be advantageous and versatile alternatives to $LiNbO_3$-based sources in high-field applications.

The summary is given in Chapter IV, in form of thesis points.

4. Optical pump sources for high-field applications

The technique of OPA opened up a new path towards generating few-cycle laser pulses with unprecedented peak powers. Such pulses are crucial for the investigation of laser-driven strong-field phenomena. In Section 4.1, the development of a pulse shaper for narrowband picosecond pump pulses is described. Section 4.2 describes a feasibility study of the short-pulse-pumped OPCPA concept in view of its scalability to the PW peak power level. The work described in Sections 4.1 and 4.2 was carried out at the Max Planck Institute of Quantum Optics in Garching, Germany. It was a contribution to the efforts of constructing OPA-based light-wave synthesizers of optical pulses with ultrahigh peak power and few-cycle controlled waveform.

4.1. Shaping of picosecond pulses for pumping optical parametric amplification

In the OPA process the resulting gain sensitively depends on the pump intensity [14, 104] and hence on the temporal and spatial shape of the pump pulse. In most cases a pump pulse with a Gaussian temporal profile is used. For a uniform gain, the pump pulse has to be significantly longer than the seed in order to keep the pump intensity approximately constant during amplification. In this case a large fraction of the pump energy is discarded (Figure 13a), thereby reducing the overall efficiency of the OPA process. If the seed and pump pulses are of comparable duration, the gain along the seed pulse will be strongly nonuniform, resulting in a distortion of the amplified pulse (Figure 13b). For a strongly chirped seed pulse this effect can possibly lead to a significant decrease of the spectral bandwidth.

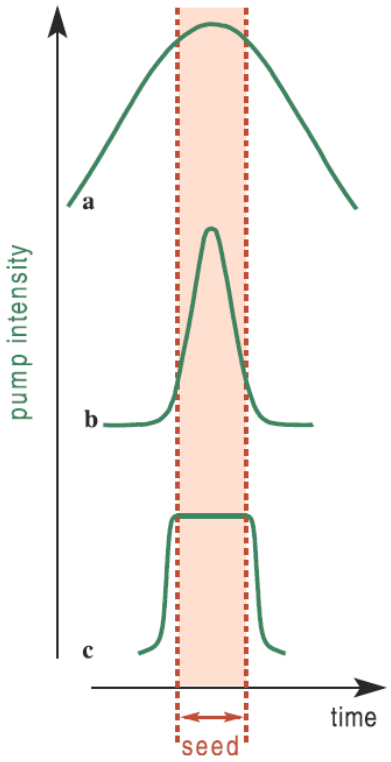

Figure 13. OPCPA with differently shaped pump pulses. The time window of the seed pulse is indicated by the shading. From Ref. [105].

These problems can be avoided by controlling the temporal shape of the pump pulse. A pump pulse with a rectangular temporal profile and a duration comparable to that of the seed pulse (Figure 13c) would provide a uniform gain for all spectral components, thereby avoiding spectral distortion and increasing the pump-to-signal conversion efficiency. If the seed profile shows a more complicated structure, as is often the case with ultrabroadband oscillators or supercontinua, a shapeable pump pulse would allow to compensate for such structure and to obtain an amplified pulse as desired. The advantage of using pump pulses, shaped both in space and time, on the OPA conversion efficiency has been previously demonstrated in the case of ~1-ns pulses and a relatively narrowband seed signal [106].

In typical ultrabroadband OPCPA systems the duration of pump pulses, obtained from a Nd:YAG laser, are usually of the order of 100 ps [11, 12] (see also Figure 2). This time scale lies below the limits of fast (opto)electronics, which therefore cannot be used for shaping such pulses. On the other hand, the corresponding bandwidth, typically a fraction of a nanometre, is too narrow to allow for conventional shaping methods based on spectral filtering, routinely used in the femtosecond regime.

The question of a passive pulse-shaping device in the picosecond regime has been the subject of a number of earlier studies [107-113], mostly motivated by applications in the field of laser-induced fusion. While some of these methods spatially shape the pulses and subsequently transform the obtained structure into the temporal domain [108-110], most approaches are based on the principle of pulse stacking [111-113]. Here a number of replicas of an input pulse are created, then delayed with respect to each other, and finally recombined to give an output pulse of the desired shape. The resulting pulse shape is extremely sensitive to the relative delays and phases of the replicas on an interferometric scale, thus the realization of this simple scheme is not straightforward. Several setups have been designed for this purpose, allowing a composition of the output pulse from up to 20 individual pulses [111]. It is clear that the more replicas are used, the finer the final shape of the pulse can be adjusted. However, in previous designs it was not possible to vary the degrees of freedom which determine the resulting pulse shape independently, thereby limiting the possible output shapes in spite of the large number of pulse replicas.

To circumvent these limitations, we developed a novel pulse-stacking setup for the shaping of picosecond pulses, using only four replicas of the input pulse, but allowing for individual adjustment of all possible degrees of freedom (i.e. relative delays, amplitudes, and phases) [105]. This enabled the fully flexible synthesis of any pulse shape allowed by the pulse-stacking principle.

The pulse shaper device

The design of the pulse-stacking interferometer is shown schematically in Figure 14. The incoming beam is split into four replicas using two pairs of birefringent prisms made of vanadate (YVO_4) crystals. Such crystals are easily available and have a large birefringence. The first prisms splits the beam into two, according to the ordinary and extraordinary polarization components. The spatial separation of the two beams is set by the distance between the first and second prisms. The second prism pair is rotated by 90° with respect to the first, and, working on the same principle, splits the two separated parts

of the beam into two parts each, creating a total of four replicas. A $\lambda/2$ waveplate is placed in front of both the first and the second prism pairs, allowing to rotate the polarization direction so that the resulting replicas are of equal intensities. In our design the location of the four beam replicas formed the corners of a square.

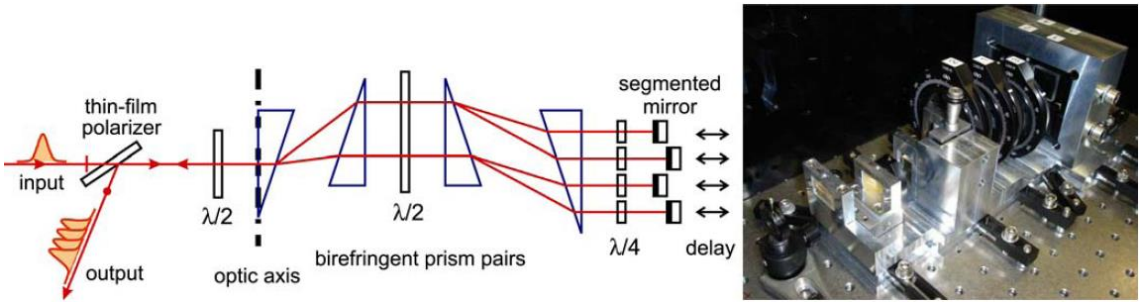

Figure 14. Left: Schematic setup of the pulse-stacking interferometer. The second pair of prisms is rotated by 90° about the beam direction for clarity. Right: Photograph of the pulse-stacking setup. From Ref. [105].

A segmented mirror retroreflects the four beamlets. The optical path of each of the pulse replicas can be controlled independently by the positions of the mirror segments. The retroreflected pulse replicas are combined by the birefringent prism pairs to form the output pulse with the desired shape and coupled out by a thin-film polarizer. The relative amplitude of each pulse replica can be adjusted independently by adjusting their polarization directions with the $\lambda/4$ plates. The resulting pulse shapes depend very sensitively on the relative phases of overlapping replicas. The adjustments on the interferometric scale can be carried out by slightly changing the tilt angle of each mirror segment. More conveniently, two of the three relative phases between the four replicas can be set by moving the second prism of each pair into or out of the beam.

Long-term stability with interferometric precision was a crucial requirement. In order to achieve such a stability we (i) minimized the number of moving parts; (ii) used a very compact design on a solid aluminium block and carefully selected optomechanical components; (iii) applied a Perspex housing to minimize environmental influences such as air turbulences. An active thermal stabilization was not necessary.

The pulse shaping can be done before laser amplification to high enough values required for OPA pumping. Therefore, the limited throughput of the pulse-shaping device, typically 20–25%, can usually be easily tolerated. The limit of our pulse-stacking concept in terms of pulse duration is set by the material dispersion of the optical components. According to our calculations, input pulses as short as ~200 fs can be used without obtaining significant distortions. The concept of our pulse stacker could be extended to a larger number of replicas, allowing to determine details of the pulse shape on a finer scale.

Results

The capabilities of the pulse-shaping device were demonstrated by using input pulses from a Nd:vanadate oscillator with a wavelength of 1064 nm, pulse energy of 6 nJ, and a duration of 19 ps. The four pulse replicas were delayed with respect to each other by ~25 ps, resulting in a shaped pulse with the approximate duration of 80 ps. The output pulse shape was measured by cross-correlation with part of the unshaped input pulse.

As the shaped pulses would have to be amplified in a laser amplifier prior to their application as pump pulses for an OPCPA stage, we also investigated the behaviour of the shaped pulses when passing through a Nd:YAG amplifier system consisting of a regenerative amplifier (regen) and a double-pass postamplifier. Shaped seed pulses of only 10 pJ energy (losses were due to some low-transmission optics before the amplifier) were amplified with a total gain of 10^7–10^8 after ~35 round trips in the regen to about ~2 mJ, and subsequently to ~100 mJ in the postamplifier.

A great variety of pulse shapes could be generated in our experiment. The cross correlation of one of these shapes is shown in Figure 15a. Assuming a shaped pulse composed of four Gaussian pulses and a least-squares fit to the measured cross correlation enabled the elimination of the effect of convolution with the reference pulse and the approximate reconstruction of the pulse shape (Figure 15b). Figure 15c and Figure 15d show the cross correlation and the fitted pulse shape for an amplified pulse, respectively. The Frantz-Nodvik model [114] was used to calculate the effect of laser amplification.

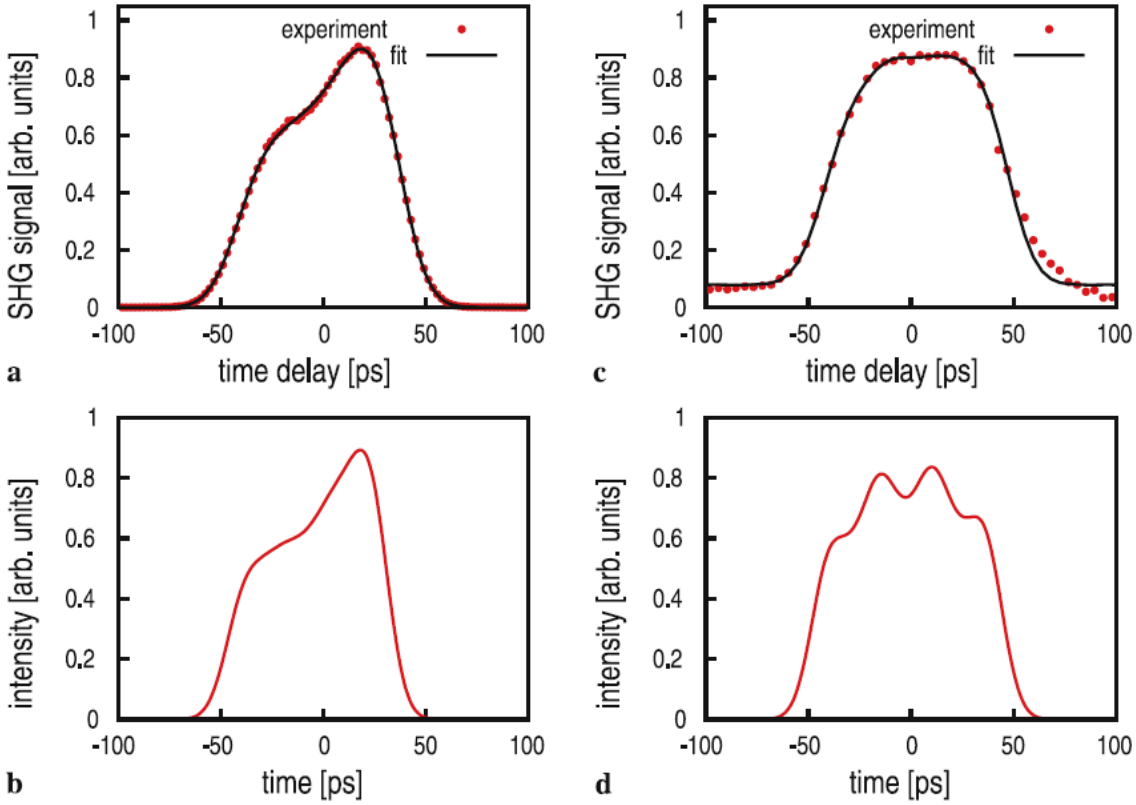

Figure 15. Cross correlation of shaped pulses (a) prior to and (c) after amplification. Figures (b) and (d) show the corresponding pulse shapes inferred from the fitting. From Ref. [105].

As discussed above, the best results in OPA are obtained for pump pulses with temporal profiles as close as possible to a flat-top shape. For generating such a pulse one needs to take into account gain depletion, which results in a higher gain for the leading edge of the pulse than that of the trailing edge. Thus, a flat-top-shaped amplified pulse requires a precompensated input pulse shape having a sloping top. In Figure 16 we can clearly see that the slope of the pulse tops is altered in the laser amplifier and that it is possible to choose a set of delays and relative amplitudes that allows to create a nearly flat-top temporal profile.

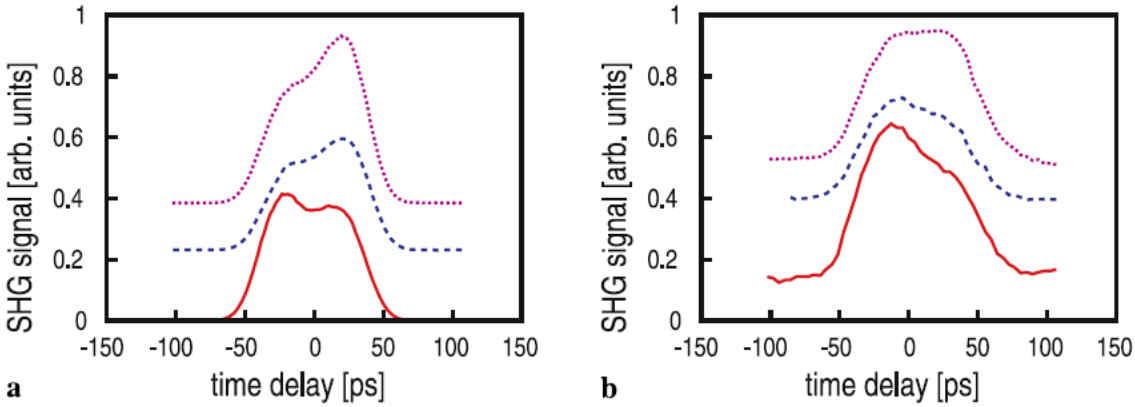

Figure 16. Cross correlation of shaped pulses with different top slopes (a) prior to and (b) after amplification. Colors indicate the corresponding measurements. From Ref. [105].

Furthermore, we can also see in Figure 16 that the rise and fall times of the amplified pulses have slightly increased in comparison with the pulses prior to amplification. The reason for this lies in the gain narrowing of the amplifying medium. For the high gain in our case the amplification bandwidth of Nd:YAG does not support 19-ps pulses. This pulse distortion effect could, in principle, be overcome by choosing a different amplifier medium with broader gain bandwidth.

It shall be noted that possible ripples on the top of the stacked pulses may be intolerable in OPCPA stages where the gain is high and the pump-to-signal conversion efficiency is low. In this case, the amplified seed spectrum very sensitively depends on intensity variations of the pump pulse. On the other hand, shaped pump pulses are important in OPCPA stages with high conversion efficiency and small gain, e.g. in the last stage of a multistage setup. Here the ripples have less influence on the signal pulse.

In conclusion, we have demonstrated the shaping and amplification of picosecond pulses to the 100-mJ level using a novel pulse-shaping interferometer based on the pulse-stacking principle. Our shaper design allows for the synthetization of any pulse shapes possible with pulse stacking. Such pulses can be used as pump pulses in OPCPA, allowing for optimization of this technique.

4.2. Short-pulse optical parametric chirped-pulse amplification for the generation of high-power few-cycle pulses

OPCPA pumped by short (100 fs to a few ps) pulses is a promising route towards boosting the output pulse energy up to the Joule level while keeping the shortest output pulse durations. This approach can surpass in peak power more established concepts of ultrabroadband OPCPA with typical pump pulse durations of about 100 ps [11, 12] (see also Figure 2). Short-pulse-pumped OPCPA systems in the few-cycle regime reported earlier were pumped by μJ-scale pulses [8-10, 19-21].

Our goal was to verify the scalability of the short-pulse-pumped OPCPA concept to higher power levels and to provide a proof-of-principle study for supporting the design of a PW-scale system to be realized in the Petawatt Field Synthesizer project at the Max Planck Institute of Quantum Optics [115, 116].

The short-pulse-pumped OPCPA approach improves the conditions for high-power few-cycle pulse generation as compared to long-pulse-pumped OPCPA in the following ways. (i) The short pump-pulse duration reduces the necessary stretching factor for the seed pulse, thereby increasing stretching and compression fidelity and allowing the use of *simple, high-throughput stretcher-compressor systems*, consisting of a block of glass for stretching and chirped multilayer mirrors for compression. (ii) The short pump pulse duration results in a short amplification time window and a *dramatically enhanced pulse contrast* outside this window. (iii) The significantly increased pump power permits the use of thinner OPA crystals, which implies an *increase of amplification bandwidth* as compared to OPA driven by longer pulses.

However, this novel approach also imposes challenges that need to be overcome. Firstly, as in the case of long-pulse OPCPA the amplification sensitively depends on the uniformity of the pump beam profile. Secondly, for short pulses the constraints on the pump-signal synchronization are stricter than with ~100-ps or longer pulses. Thirdly, the matching of pump and signal pulse fronts has to be considered, which is critical especially in OPCPA systems with sub-ps pump pulse duration and with relatively large beam diameters.

Experimental setup and methods

The experimental setup is shown in Figure 17. The ATLAS TW-scale Ti:sapphire CPA laser system was used as a drive laser both for seeding and pumping the OPCPA. It consists of a broadband oscillator, a preamplifier, a stretcher, a regenerative amplifier, a postamplifier, and a vacuum compressor. The output pulses have an energy of 350 mJ and a pulse duration of 43 fs at a repetition rate of 10 Hz.

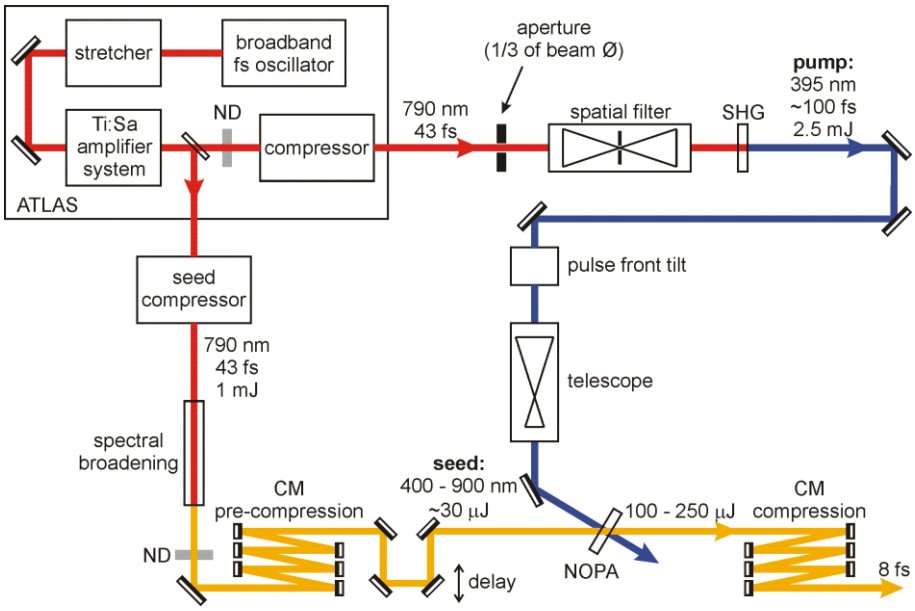

Figure 17. Schematics of the short-pulse-pumped OPCPA experimental setup. ND: neutral density filter, CM: chirped mirror. From Ref. [115].

Both seed and pump pulses for OPCPA were derived from the ATLAS laser. Owing to this optical synchronization the strict requirements of fs-scale timing precision were still met even after separately propagating the two beams along path lengths of about 20 m before overlapping them in the OPA crystal. Seed pulses were generated by splitting

and separately compressing a small (1 mJ) fraction of the uncompressed ATLAS pulses to ~43 fs, followed by spectral broadening in a gas cell filled with 1.4 bar of Ar. The output pulse energy was 0.8 mJ. A typical broadened spectrum is shown in Figure 18 (red solid curve). A comparison with the input spectrum (black dotted curve) reveals a broadening factor of about four, giving a transform-limited pulse duration of about 10 fs. We note that the very broad but weak tail with an exponentially decreasing intensity extending on the short-wavelength side down to 400 nm (Figure 18, inset (a)) was important for amplification, besides the intense part between ~750 nm and ~850 nm. The filament also acted as a spatial filter resulting in an excellent output beam quality (Figure 18, inset (b)). According to measurements using spectral phase interferometry for direct electric field reconstruction (SPIDER, [117]) the seed pulse duration was about 100 fs. Since this was comparable to the duration of the pump pulse, chirped-mirror precompression was used in order to avoid spectral narrowing in the OPA process.

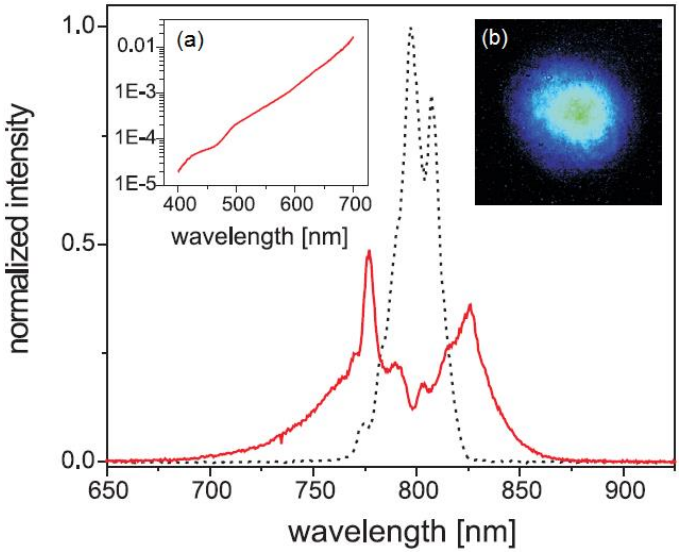

Figure 18. The seed spectrum before (black dashed line) and after (red solid line) broadening. Inset (a) shows the short-wavelength tail of the broadened spectrum in a semi-logarithmic plot. Inset (b) shows the beam profile after the plasma filament. From Ref. [115].

The OPCPA stage was pumped by frequency doubling a small fraction of the output of the ATLAS laser in a 2-mm-thick KDP crystal with ~40% conversion efficiency (Figure 17). In the OPA process the resulting gain sensitively depends on the pump intensity [14, 104, 105]. A pump beam with a sufficiently smooth beam profile was obtained by using a combination of a soft aperture and a vacuum spatial filter with a cone-shaped glass capillary pinhole [118]before the SHG crystal. About 2.5 mJ pulse energy was obtained at 395 nm with an estimated pulse duration of 85 fs.

In order to obtain an amplification bandwidth as large as possible a noncollinear geometry was used for the OPA [5]. This geometry along with short pulse durations and the relatively large beam diameters of a few mm, required matching of the pulse fronts of the pump and the seed beams by tilting one of them [9, 19]. Tilting the pump pulse front was accomplished by a pair of transmission gratings (similar to those in Ref. [119]) followed by a demagnifying reflective telescope.

Results

In our OPCPA experiments we have used BBO crystals of different thicknesses (0.5 mm, 1 mm, and 2 mm) with all of which we were able to observe ultrabroadband amplification. The amplified signal energy varied between 100 μJ and 250 μJ, depending on the amplification range and bandwidth, which was tuneable by changing the orientation of the crystal and thereby the phase-matching condition.

The noncollinear angle between pump and seed (see also Figure 1) was close to $\alpha = 3.7°$ inside the crystal set for type-I phase matching in the visible and near-infrared spectral range with the broadest possible bandwidth. By changing the crystal orientation the amplified region of the spectrum could easily be tuned. The diameter of the pump beam at the OPA crystal was about 3 mm. In order to prevent optical damage at the last telescope mirror and at the OPA crystal the pump energy was attenuated to ~1 mJ. With 85 fs pulse duration this gave a pump peak intensity of about 150 GW/cm^2. Owing to the limited pump energy used in this experiment the seed energy was also attenuated to ~30 μJ before entering the OPA crystal.

A typical amplified signal spectrum (Figure 19a, red solid curve), obtained with the 1-mm BBO crystal, shows a very large amplification bandwidth ranging from below 550 nm to above 800 nm. This spectrum corresponds to a Fourier-limited (FL) pulse duration of less than 5 fs (Figure 19b). In this case the pulse-front matching was achieved by using a 45°-apex-angle BK7 prism. The pump energy was 560 μJ, the seed energy was 21 μJ, which resulted in an amplified pulse energy of 153 μJ. Each of these energies were subject to shot-to-shot fluctuations of about 7%.

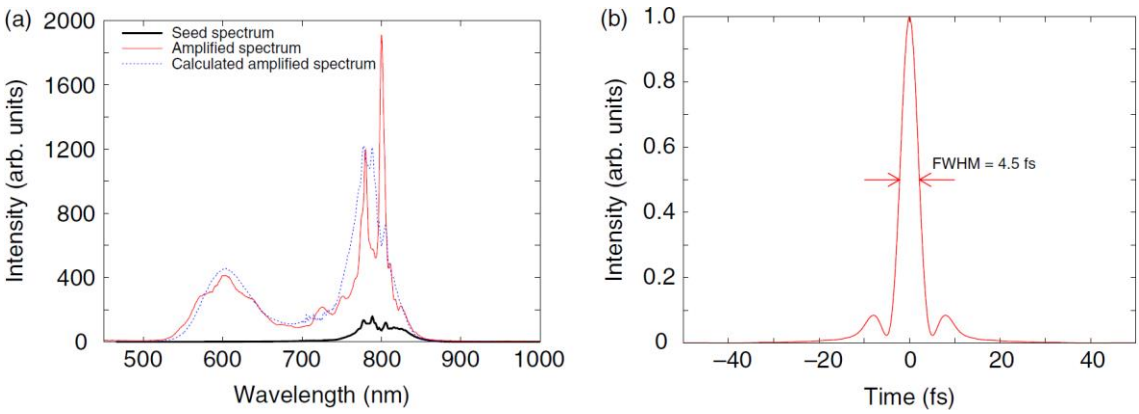

Figure 19. (a) Measured spectra of seed (black solid curve) and amplified signal (red solid curve). Simulation results for the amplification based on the measured seed spectrum as input are also shown (blue dotted curve). (b) Calculated FL temporal pulse form corresponding to the measured amplified signal spectrum shown in (a). From Ref. [115].

Comparing the seed and the amplified signal spectra in Figure 19a clearly indicates the large variations in gain between different spectral ranges. Between 750 nm and 850 nm where the spectral intensity of the seed is large, we see a gain of about 3 to 4, whereas in the weak exponential tail below 700 nm (cf. Figure 18) the gain is several orders of magnitude larger. The reason for this is the different regimes of the amplification process: while the amplification is strongly saturated around the 800 nm peak, the short-wavelength wing, being several orders of magnitude smaller, is unsaturated and experiences a much larger (small-signal) gain. The important consequence is an enhanced

bandwidth and a considerably reduced FL pulse duration (from about 10 fs for the seed to below 5 fs for the signal, Figure 19b).

In order to test the compressibility of the amplified spectrum the output pulses were reflected off a set of chirped mirrors and characterized by our home-built SPIDER apparatus. In these measurements the thickness of the OPA crystal was chosen to be 2 mm, because of the larger output energy. Owing to the limited bandwidth of the chirped mirrors on the short-wavelength side, the OPA crystal was tuned to a narrower amplification bandwidth centred around 770 nm. The amplified spectrum (Figure 20a) in this case supported a transform-limited pulse duration of 6.7 fs (Figure 20b). The pump, seed, and resulting amplified energies were 370 µJ, 60 µJ, and 150 µJ, respectively. The reconstructed spectral phase (Figure 20a, black solid line) is nearly flat across the pulse spectrum indicating a good compression. A Fourier transform into the time domain reveals a compressed amplified-pulse duration of 8.0 fs (Figure 20b), which is reasonably close to the FL pulse duration of 6.7 fs.

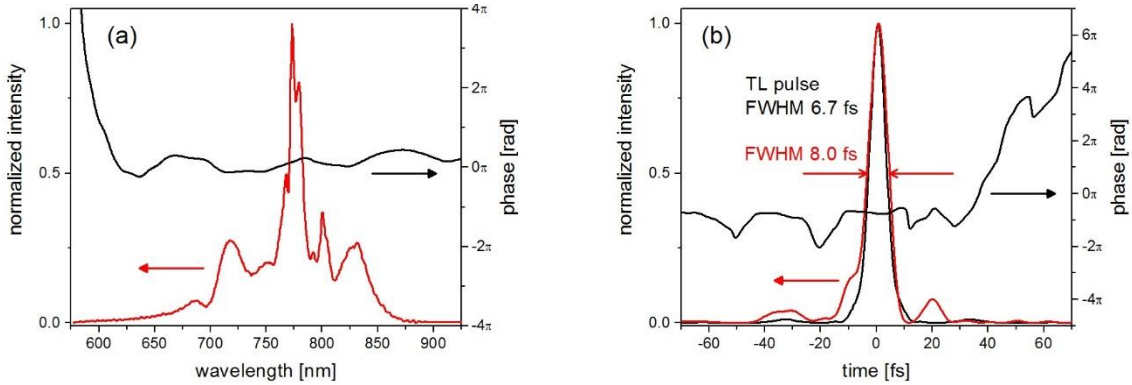

Figure 20. Reconstructed spectral (a) and temporal (b) intensity and phase of amplified and compressed signal pulses based on SPIDER measurements. From Ref. [115].

It shall be noted that the demonstrated pulse parameters do not represent a new regime in terms of pulse duration and peak power. Alternative methods, such as the compression of a spectrally broadened hollow-fibre output [120], have been shown to deliver pulses in the few-cycle regime with a pulse duration of down to 5.6 fs and pulse energy up to 1.2 mJ [121]. However, the scalability of these methods is a known limitation if PW power levels are considered.

The demonstrated ultrabroadband OPCPA with an output energy on the 100-µJ level pumped by short pulses (~100 fs) and compression of the amplified pulses to the sub-10-fs, few-cycle regime constituted the first feasibility test on the way towards boosting the power of few-cycle optical pulses to the PW level (Petawatt Field Synthesizer project at MPQ [116]) based on the short-pulse OPCPA concept. In order to reach higher output energies, high-power pump lasers with a very good spatial uniformity of the beam are necessary to meet the strong requirements of OPCPA pumping. For large-scale system, such as the PFS, few-ps pump pulses are more advantageous, which enable to combine advantages of the short-pulse OPCPA concept with less critical requirements, e.g. for pulse-front matching, making the system design more robust.

5. $LiNbO_3$ THz sources with extremely high energy

Efficient phase-matched THz generation by OR in LN became possible by tilting the pulse front of femtosecond pump pulses [48]. The increase of the THz pulse energy by several orders of magnitude was demonstrated with this technique [58, 59]. The generation of near-single-cycle THz pulses with energies of 10 μJ [60], 30 μJ [61], and 50 μJ [62]were reported, pumped by amplified Ti:sapphire laser systems with pulse energies up to as much as 120 mJ. Despite the substantially increased THz pulse energies, the efficiencies remained at about 0.1% or below. In these experiments, pump pulses with a short FL pulse duration (50 fs to 140 fs) were used.

While 10-μJ scale THz pulse energies and 100-kV/cm scale electric field strength enabled many interesting studies of THz induced nonlinear phenomena, intriguing new applications require THz pulse energies which are one or two orders of magnitude larger than what was available by short-pulse pumped OR in the frequency range of 0.1 THz to 1 THz. Examples of such application possibilities are manipulation of molecules by strong (quasistatic) electric fields, investigation of material properties and processes under the influence of extremely high quasi-static fields, enhancement of attosecond pulse generation [94-97], electron acceleration, undulation, deflection, and spatial as well as temporal focusing [98] (see also Section 3.4).

We note that ultrashort pulses at higher frequencies (several tens of THz, where the conversion efficiency can be higher) with electric field strengths up to 10 MV/cm and 100 MV/cm could be achieved by optical parametric amplification [69] and difference-frequency generation [70] in GaSe, respectively. However, due to the material properties of GaSe, this technique is not easily scalable to higher energies and lower frequencies.

Motivated by the application potential, our goal was to increase the THz generation efficiency and the THz pulse energy in the low-frequency part of the THz spectrum by exploiting the potential of TPFP in LN. This required the detailed theoretical investigation of the THz generation process, discussed in Section 5.1. The investigation of novel optimized pulse-front tilting setups and their impact on the THz beam properties is the subject of Section 5.2. Optimizing the pumping conditions enabled us to demonstrate THz pulse energies approaching the mJ level, discussed in Section 5.3. The high THz field strength can influence the pump pulse propagation, thereby influencing the THz generation process and possibly leading to pulse and beam distortions of the emerging THz radiation. Such effects are investigated in Section 5.4.

5.1. Basic design aspects

It was our goal to give a guideline for the design of high-energy THz pulse sources based on OR of femtosecond pulses and to assess the possibilities of increasing the THz energy further. The key issues are selection of the nonlinear material, crystal length, optimal pumping conditions (wavelength, pulse duration, intensity), and optimization of the pulse-front-tilting setup. Whereas the effect of choice of some of these parameters were discussed to predict the generation of μJ-level THz pulse energies [56], a more complete picture was necessary to explore the feasibility to reach the mJ energy level. A detailed analysis of the TPFP scheme and its design details were not discussed in the literature.

Our study included various materials suitable for optical rectification. The discussion of the basic design aspects in this chapter are general, but the emphasis will be on LN. The case of semiconductors will be discussed in more detail in Chapter 7.

Theoretical model

Efficient THz generation by OR requires phase matching, i.e. matching the group velocity of the optical pump pulse to the phase velocity of the THz radiation [36, 48]. Collinear velocity matching is possible only for specific wavelengths and materials (see Section 3.3). For most of the commonly used laser wavelengths and materials the group velocity $v_g(\omega)$ of the pump pulses differs from the phase velocity $v(\Omega)$ of the THz field, where ω and Ω are the optical pump and THz frequencies, respectively. If $n_g(\omega) < n(\Omega)$, noncollinear velocity matching can be achieved by tilting the pump pulse front [48]. Here, n is the refractive index and $n_g = c/v_g$ is the group index, c is the speed of light in vacuum. In this case, velocity matching reads as $v_g(\omega_0) \cdot \cos\gamma = v(\Omega_0)$ [see Eq. (II.15)], where ω_0 and Ω_0 are the phase-matching pump and THz frequencies, respectively, and γ is the required PFT angle.

In order to assess the suitability of different nonlinear materials for THz generation in the TPFP scheme and to compare them to each other in a quantitative way we performed numerical calculations [41]. In the calculations the following effects were taken into account:

1. The variation of the pump pulse duration (and therefore of the pump intensity) with the propagation distance due to material dispersion and angular dispersion [53, 122].
2. The noncollinear propagation direction of pump and THz beams. For the pump, in the one-dimensional picture, the projected propagation distance onto the THz propagation direction was used in order to account for the noncollinear phase matching in a TPFP scheme.
3. The absorption at THz frequencies due to the complex dielectric function (determined by phonon resonances) and to free carriers generated by pump absorption.

These effects were included into the one-dimensional wave equation for the Fourier component $E(\Omega, z)$ of the THz field at the angular frequency Ω [36, 123], which follows from Maxwell's equations in the slowly varying envelope approximation:

$$\frac{\partial E(\Omega,z)}{\partial z} = -\frac{i\mu_0\Omega c}{2n(\Omega)} P_{\mathrm{NL}}\left(\Omega, \frac{z}{\cos\gamma}\right) e^{i\Delta k z} - \frac{1}{2}\alpha\left(\Omega, \frac{z}{\cos\gamma}\right) E(\Omega,z), \qquad \text{(III.1)}$$

where the Fourier component of nonlinear polarization, P_{NL}, can be expressed through the material nonlinear susceptibility $\chi^{(2)}$ as

$$P_{\mathrm{NL}}\left(\Omega, \frac{z}{\cos\gamma}\right) = \varepsilon_0 \chi^{(2)} \int_0^\infty E\left(\omega+\Omega, \frac{z}{\cos\gamma}\right) E^*\left(\omega, \frac{z}{\cos\gamma}\right) \mathrm{d}\omega. \qquad \text{(III.2)}$$

Here ε_0 and μ_0 are the permittivity and permeability of free space, respectively, α is the intensity absorption coefficient as discussed below, z is the THz propagation coordinate, $z/\cos(\gamma)$ is the coordinate in the pump propagation direction (see Figure 21). We note that for a more accurate simulation of high-power THz generation, also cascaded $\chi^{(2)}$

processes should be taken into account (see e.g. [46, 47, 124]]). However, such effects were neglected here for simplicity (cf. Section 5.4). The temporal shape of the THz field was obtained by Fourier transformation.

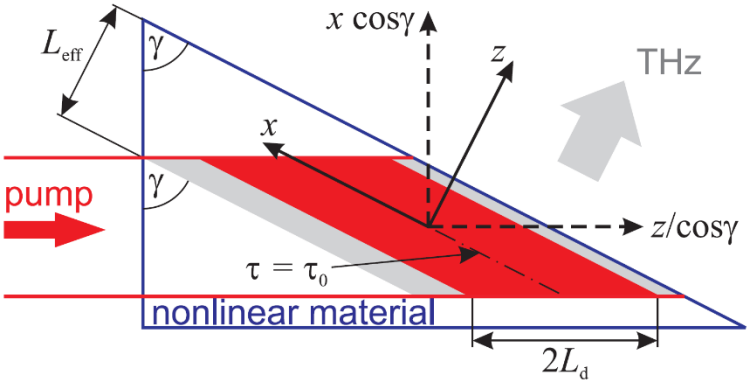

Figure 21. Geometry of noncollinear THz generation and the coordinates used. The origin of the coordinate system is at the position of shortest, FL pump pulse duration ($\tau = \tau_0$) at the pump beam center. The nonlinear material is prism-shaped. From Ref. [41].

In case of collinear THz generation, the wave-vector mismatch Δk is given by the following relation [36]:

$$\Delta k(\Omega) = k(\Omega) + k(\omega_0) - k(\omega_0 + \Omega) \approx k(\Omega) - \Omega \frac{\mathrm{d}k}{\mathrm{d}\omega}\bigg|_{\omega_0} = \frac{\Omega}{c}\left[n(\Omega) - n_{\mathrm{g}}(\omega_0)\right]. \tag{III.3}$$

Here, the approximation was made under the condition $\Omega \ll \omega_0$. For noncollinear geometry this should be modified as

$$\Delta k(\Omega) \approx \frac{\Omega}{c}\left[n(\Omega) - \frac{n_{\mathrm{g}}(\omega_0)}{\cos\gamma}\right], \tag{III.4}$$

since the pump pulse propagation distance is $1/\cos\gamma$ times larger than the THz propagation distance.

Absorption at THz frequencies has two main contributions:

$$\alpha\left(\Omega, \frac{z}{\cos\gamma}\right) = \alpha_{\varepsilon}(\Omega) + \alpha_{\mathrm{fc}}\left(\Omega, \frac{z}{\cos\gamma}\right). \tag{III.5}$$

The first one, α_{ε}, is determined by the complex dielectric function of the material while the second term, α_{fc}, is due to free carriers generated in the medium by the pump pulse (therefore its position dependence). We note that Equation (III.5) represents an approximation to the absorption coefficient and, besides absorption, also the real part of the refractive index is influenced by the free carriers. However, we found that in the range of pump intensities considered here, free-carrier refractive index has only a small effect on the THz generation efficiency, THz spectrum, peak electric field, and waveform. For this reason, the free-carrier contribution to the refractive index was neglected.

The density of free carriers, N_{fc}, generated by the pump pulse can be calculated as

$$N_{\mathrm{fc}}\left(\frac{z}{\cos\gamma}\right)=\frac{I\tau}{hc/\lambda_0}\left(\alpha_0+\frac{1}{2}\beta_2 I+\frac{1}{3}\beta_3 I+\cdots\right). \tag{III.6}$$

Here, $\tau=\tau(z/\cos\gamma)$ is the pump pulse duration, $I=I(z/\cos\gamma)$ is the time-averaged pump intensity, $\lambda_0=2\pi c/\omega_0$ is the pump phase-matching (central) wavelength, $\alpha_0=\alpha_\varepsilon(\omega_0)$, β_2, and β_3 are the linear, two-, and three-photon absorption coefficients, respectively. The FCA coefficient α_{fc} was calculated using the Drude-model [125]:

$$\alpha_{\mathrm{fc}}\left(\Omega,\frac{z}{\cos\gamma}\right)=2\frac{\Omega}{c}\,\mathrm{Im}\left[\sqrt{\varepsilon_\infty\left(1-\frac{\omega_{\mathrm{p}}^2}{\Omega^2+i\,\Omega/\tau_{\mathrm{sc}}}\right)}\right], \tag{III.7}$$

where ε_∞ is the high-frequency dielectric constant, τ_{sc} is the electron scattering time, $\omega_{\mathrm{p}}=e\sqrt{N_{\mathrm{fc}}/(\varepsilon_0\varepsilon_\infty m_{\mathrm{eff}})}$ is the plasma frequency, e and m_{eff} are the electron charge and effective mass, respectively. Note that α_{fc} depends on the pump propagation coordinate $z/\cos\gamma$, since N_{fc} depends on it. The material parameters used in the calculations are listed in Table 1 of Ref. [41].

The model described here is a simplified one-dimensional model of noncollinear THz generation. Effects due to finite pump beam cross section, such as the decrease of interaction length due to spatial walk-off, or variation of pump pulse duration and intensity across the beam, are not included in this model. Despite the simplifications, the model showed a good predictive power to guide the experimental work.

Interaction length for THz generation

In order to analyse the effects of the choice of pump pulse duration and its spatial variation with the propagation coordinate on the THz generation process in the TPFP scheme, we have carried out numerical calculations using the model described above [41]. Stoichiometric LN was chosen as the nonlinear material, pumped at 800 nm wavelength, which is used in many experiments.

Figure 22a shows the variation of the pump pulse duration with the pump propagation distance within the nonlinear material. Each curve corresponds to different FL pulse durations (τ_0). An appropriate amount of initial chirp was assumed in the calculation to ensure that the pulse duration reaches its FL in the middle of the medium. In experiment this can be achieved by adjusting the grating separation of the pulse compressor in a CPA laser system. Since in case of LN a PFT as large as 62.7° is required for phase matching the dominant pulse-stretching effect is GVD originating from angular dispersion [122], which is proportional to $\tan^2(\gamma)$ (see Equation (II.17)). A dispersion length L_{d} can be defined as the propagation length over which the pump pulse duration increases by a factor of $\sqrt{2}$ from its FL [1]. Note that L_{d} is proportional to τ_0^2.

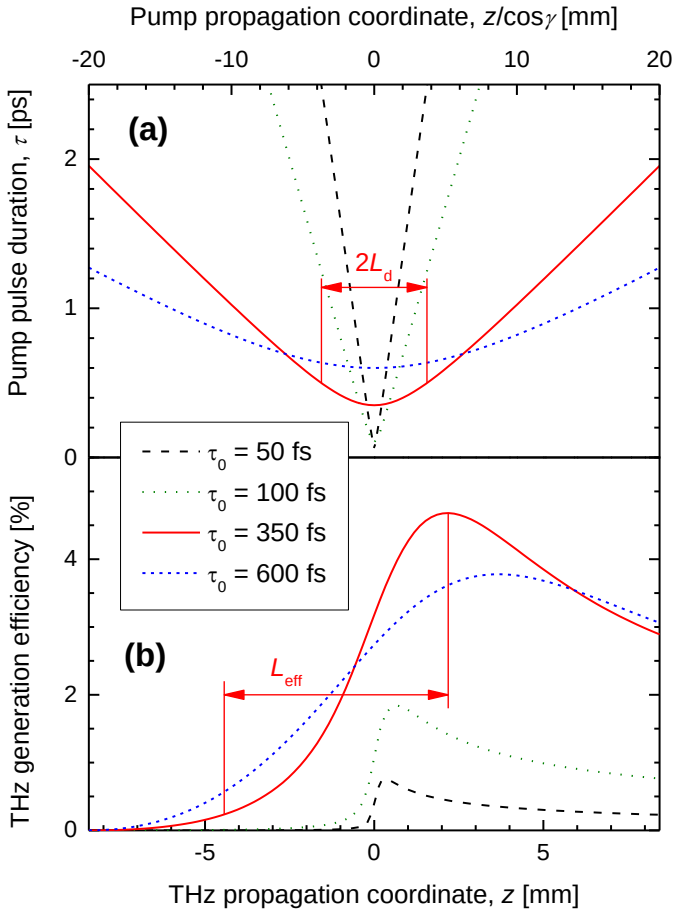

Figure 22. Variation of pump pulse duration (a) and the corresponding THz generation efficiency (b) inside the nonlinear material (LN) for various values of the FL pulse duration τ_0. From Ref. [41].

Figure 22b shows the corresponding build-up of the THz field in terms of pump-to-THz energy conversion efficiency at a constant pump fluence level of 5.1 mJ/cm^2. At this moderate pumping level saturation of THz generation (for example due to three-photon absorption, see e.g. [59]) can be neglected. As can be seen from the curves the THz field experiences a significant gain only in the region where the pump pulse is shortest. Outside this region the pump intensity drops and THz absorption overcomes the gain leading to decreasing THz intensity. We defined an effective THz generation length L_{eff} as the distance measured in the THz propagation direction over which the THz intensity grows from the arbitrarily chosen 5% to its peak value. For a particular pump pulse duration it is useful to choose the crystal dimensions according to this effective length (see Figure 21). The crystal should be positioned along the pump beam such that the maximum of the THz efficiency is reached at the crystal output surface.

For many experiments it is more important to reach the maximum THz field strength rather than the maximum conversion efficiency. An effective length can be defined for the THz peak electric field strength in a similar manner. This length is usually shorter than that defined above for the efficiency since with increasing propagation length dispersion tends to broaden the THz pulse thereby decreasing the peak field strength.

Figure 23 shows the dependence of the THz generation efficiency and the effective THz generation length on the FL pump pulse duration. The useful crystal thickness in the THz propagation direction increases monotonically with the pump pulse

duration. The corresponding THz generation efficiency has a maximum at 350 fs, which indicates the optimal choice of pump pulse duration for high-energy THz pulse generation. For shorter FL pulse duration, the effective length is smaller, reducing the THz yield. Longer FL pulse duration gives larger L_{eff}, however, the role of THz absorption increases, thereby reducing the THz yield.

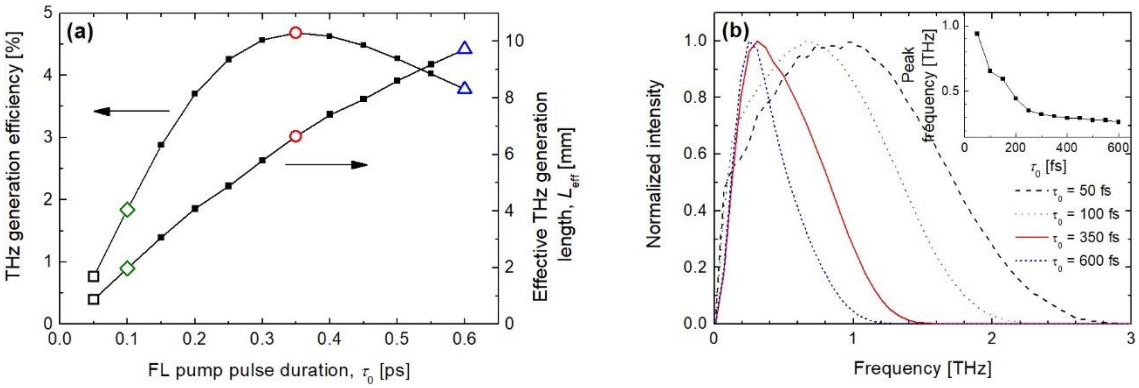

Figure 23. (a) THz generation efficiency and effective THz generation length in LN as functions of the FL pump pulse duration. (b) The THz spectra corresponding to the marked points in (a). The inset shows the dependence of the spectral peak frequency on the FL pump pulse duration. In all cases the pump fluence was 5.1 mJ/cm^2 and the phase matching frequency 1 THz. From Ref. [41].

For many applications the THz spectrum is also important. In case of $\tau_0 = 50$ fs the spectral peak is located at 1.0 THz and the FWHM bandwidth is 1.7 THz (Figure 23b). Pumping with 350-fs pulses the THz generation efficiency can be increased by more than a factor of five (Figure 23a), however the spectrum shifts to lower frequencies with a peak at 0.3 THz (see also inset of Figure 23b) and the bandwidth decreases to 0.7 THz. Hence, the design of a THz source for a specific application requires a suitable trade-off between maximizing the THz energy (or field strength), on the one hand, and providing the required spectral range, on the other hand.

Extremely high THz field strengths and pulse energies

Using the model described above we showed that OR of femtosecond pulses in LN by using the TPFP technique is a promising candidate to reach extremely high THz field strengths and pulse energies [126, 127], crucial for a number of interesting applications. The effect of varying the FL pump pulse duration and the crystal temperature (to minimize its THz absorption) were investigated and optimal conditions were given. We showed that using FL pump pulse durations longer than the commonly used ~100 fs can allow for larger pump-to-THz energy conversion efficiencies by utilizing longer crystal lengths for THz generation. This is in contrast to simply pre-chirping a short FL pump pulse [62], which merely allows to achieve the shortest average pulse duration inside the nonlinear crystal.

In the calculations Gaussian pump pulses with a peak intensity of 40 GW/cm^2 were used, which is about half of the intensity where the onset of FCA was experimentally observed in LN [44]. This choice enables close-to-maximum THz yield, while still avoids the limitations set by FCA on the useful pump intensity [41]. For the pump wavelength 1.06 μm was chosen. A trend towards using such longer wavelengths for OR-based THz sources could be recognized [44, 128-131]], triggered by the development of compact femtosecond laser sources operating in the infrared spectral range.

The FL pump pulse duration was varied between 50 fs and 1 ps. In order to ensure the highest average pump intensity within the crystal, the pump pulses were assumed to be suitably prechirped. The waveform and the peak electric field of the THz pulses were calculated from the amplitude spectra by Fourier transformation. At each value of the pump pulse duration the phase-matching frequency was iteratively fitted to the central frequency of the generated THz spectrum. For the shortest pump pulse durations the crystal length was set to give maximal THz peak electric field strength at the crystal output. For longer pump pulses, the crystal length was set to 10 mm at maximum (see [126], Table 1 for more details). Due to the large PFT angle of ~63°, and the associated walk-off effect, longer crystals are impractical even for cm-size pump beams. As no imaging distortions of the TPFP setup were included in the model used here, the results are most adequate for an optimized-imaging setup up to about 1 cm pump spot size [41], or to a contact-grating device without imaging [132], see also Section 5.2.

In order to avoid photorefraction [55] and to reduce THz absorption [57] sLN doped with 0.7 mol% Mg was assumed as the nonlinear medium. LN has significant absorption in the THz range at room temperature (Figure 24). Since decreasing the crystal temperature decreases the absorption in the THz range [57], our study was also extended to cryogenic temperatures (100 K, 10 K). The refractive index of sLN in the THz range is large ($n \approx 5.0$ at 1 THz) and the significant Fresnel loss at the output surface of the crystal (about 45% for perpendicular incidence) was also taken into account.

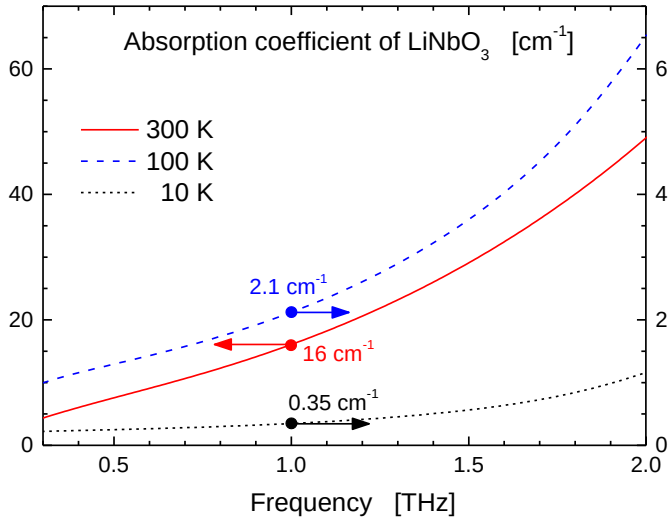

Figure 24. Frequency dependence of the absorption coefficient of LN in the THz range for different temperatures. From Ref. [126].

The calculated peak electric field strength of the THz pulses in air immediately after the output surface of the crystal is shown in Figure 25a for different temperatures as a function of the FL pump pulse duration. The cross symbol indicates 240 kV/cm peak THz electric field for conditions (100-fs pump pulse, 300 K crystal temperature) typically used in experiments pumped by amplified Ti:sapphire laser systems [60, 61, 84, 133]. This exceeds only by about a factor of two the value of 110 kV/cm at the output of the crystal obtained experimentally from the measured peak THz intensity and spot size [84]. Possible reasons for the difference are the shorter than 100 fs FL pump pulse duration in

experiments and imaging errors in the TPFP setup [41]. The peak of the calculated THz spectrum is at 1.1 THz (Figure 25b, red curve), similar to the experimental observation. This approximate agreement indicated that our model gave realistic predictions for the order of magnitude of the THz output in experiments. Our experiments described in Sections 5.2, 7.2, and 7.3 also confirmed the predictive power of the model.

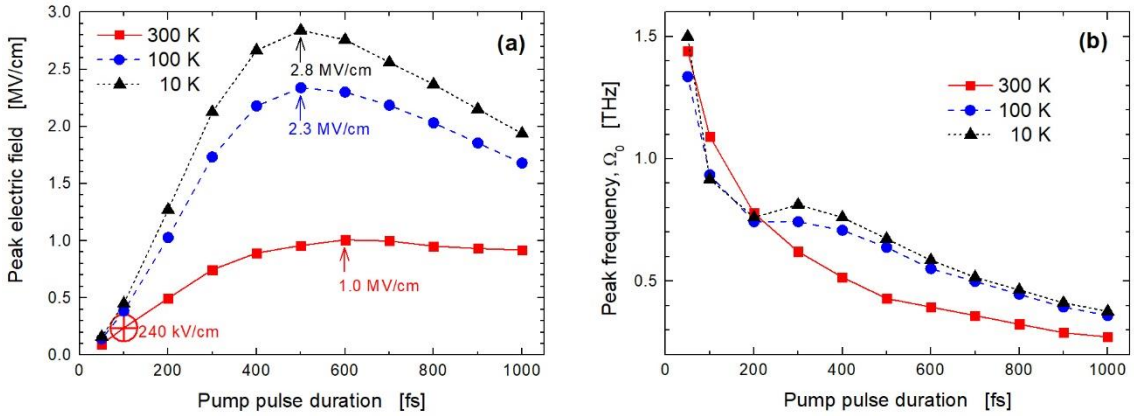

Figure 25. Calculated peak electric field strength (a) and frequency of the spectral peak (b) of the THz pulses at the output of the crystal as function of the FL pump pulse duration at different temperatures. From Ref. [126].

Examples of calculated THz spectra at 100 K for different pump pulse durations are shown in Figure 26a. The peak spectral intensity increases and the position of the spectral peak shifts to lower frequencies with increasing pump pulse duration. This behaviour can be observed for all temperatures, as it is shown for the peak frequencies in Figure 25b (see also Figure 23b). The central THz frequency varies between 1.5 THz and 0.27 THz for the investigated pump pulse duration range. Examples of calculated THz waveforms are shown in Figure 26b, which will be discussed below.

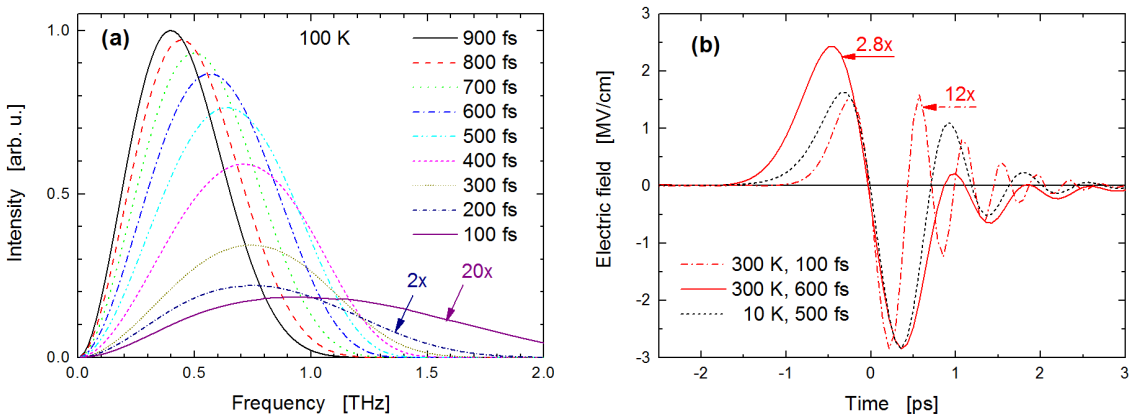

Figure 26. (a) Calculated THz spectra for different FL pump pulse durations at 100 K temperature. (b) Calculated electric field waveforms of the THz pulses at the output of the crystal belonging to the optimal FL pump pulse durations for temperatures of 300 K and 10 K, as well as to 100 fs at 300 K. The curves for 300 K were scaled by the indicated factors for better visibility. From Ref. [126].

Increasing the pump pulse duration from the commonly used 100 fs results in a significant increase of the THz peak electric field (Figure 25a). This increase is as high as a factor of more than four when an optimal pump pulse duration of 600 fs is chosen at

room temperature, resulting in the extremely high value of 1.0 MV/cm at the output of the crystal. The corresponding spectral peak is reduced to 0.4 THz (Figure 25b). The reason of the increase in field strength is twofold: (i) The longer pump pulse causes a shift of the THz spectrum to lower frequencies, which results in reduced absorption within the crystal (see Figure 24). (ii) The longer pump pulse also allows for a longer THz generation length [41].

Even higher electric field can be reached at lower temperatures. At 100 K and 10 K the maxima are located at 500 fs (Figure 25a) with a field strength of 2.3 MV/cm and 2.8 MV/cm, respectively, corresponding to an enhancement of about one order of magnitude as compared to 300 K and 100 fs. The reason for this increase is clearly the reduced THz absorption at cryogenic temperatures (Figure 24). In cases of optimal pump pulse duration the central THz frequency has a value of 0.40 THz at 300 K, 0.64 THz at 100 K and 0.67 THz at 10 K (Figure 25b).

Figure 26b shows the time-dependent electric field for the optimal pump pulse durations at 300 K and 10 K temperatures. For comparison, the THz pulse shape is also shown for 100 fs and 300 K closest to typical experimental parameters, as mentioned above. A 12-fold increase in the peak electric field is predicted over the common 100-fs 300-K case when cooling the crystal to 10 K and using optimal 500-fs pump pulses.

The calculated optical-to-THz energy conversion efficiency as function of the FL pump pulse duration is shown in Figure 27a. The efficiency maxima are located at 400 fs for both cryogenic temperatures. As expected, the difference between the efficiencies belonging to different temperatures is even more pronounced than that between the electric fields. At room temperature the efficiency increases from 0.31% for 100 fs to 2.0% for 500 fs. Cooling the crystal to 100 K gives 8.9% efficiency for 400 fs, and at 10 K the efficiency gets as high as almost 13%.

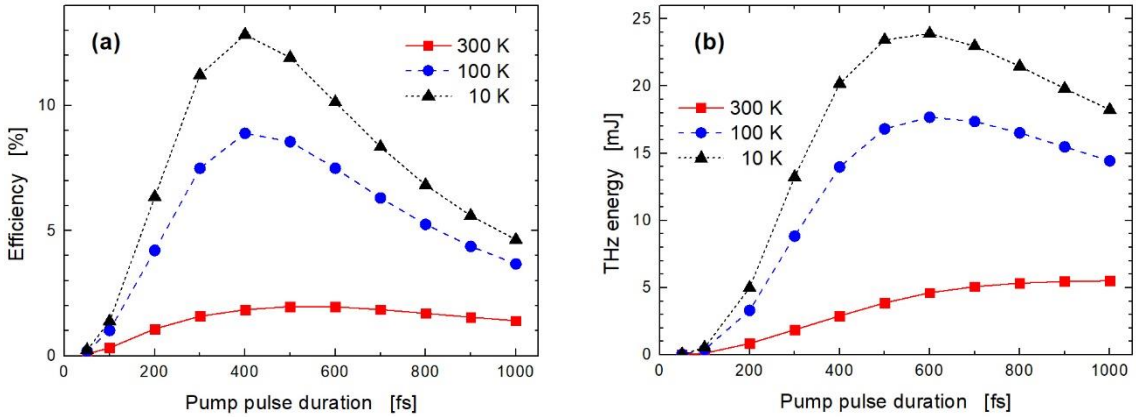

Figure 27. Optical-to-THz energy conversion efficiency (a) and THz pulse energy assuming a pump spot diameter of 5 cm (b) as functions of the FL pump pulse duration at different temperatures. From Ref. [126].

The TPFP technique is scalable to higher THz energies and field strengths by increasing the pump spot size and energy. To fully exploit this scaling potential we proposed a contact-grating technique which is exempt from imaging errors [132] (see Sections 5.2 and 7.2). When utilizing such distortion-free THz sources, our calculations indicated the feasibility of scaling the THz pulse energy to the tens-of-mJ level. Figure 27b shows the calculated THz energy obtained with the efficiencies of Figure 27a, and a

pump beam diameter of 5 cm. As high as 23 mJ THz energy is predicted by pumping a 1-cm thick LN crystal cooled to 10 K with 500-fs pulses, requiring only about 200 mJ of pump energy. This represented an expected increase in THz pulse energy by more than 400 times over the state-of-the art [62]. The predicted THz electric field strength at the output of the crystal was 2.8 MV/cm in this case (Figure 25a). This can be further increased by the use of optimized THz *imaging* optics behind the crystal to the 10-MV/cm level without any significant frequency cut-off. In this case we assumed a 1 cm THz beam diameter at the output of the LN crystal and a THz beam diameter of 1.6 mm in the image plane. Assuming a THz beam diameter of 5 cm and a very good *focusability* from a contact-grating setup, a spot size of 0.57 mm can be reached at the central frequency of 0.67 THz by a 5-cm focal-length parabolic mirror. Even though in this setup the shape of the THz signal will be distorted because of diffraction [134], a peak electric field strength of about 100 MV/cm can be expected.

We note that the extremely high efficiency values predicted by our calculations correspond to pump-to-THz photon conversion efficiencies exceeding 100%. Such high photon conversion efficiencies are caused by cascade effects [135], the importance of which were also indicated by experiments [46, 60, 61, 136, 137]. The influence of the THz field on the pump pulse can be significant in case of the very large efficiency values predicted for optimal pump pulse durations at cryogenic temperatures. Such an influence can cause an increase of the THz generation efficiency under certain conditions [46, 138], but it can also impose limitations [47, 124]. A more accurate numerical study requires to take these effects into account. A study related to such effects is given in Section 5.4. We also note that at very high THz fields the effective nonlinearity of LN might change (future experiments should clarify the sign and magnitude of this behaviour), which can lead to a significant decrease or increase of the THz generation efficiency.

In summary, our numerical calculations for TPFP in LN predicted a significant increase in the THz generation efficiency and peak field strength. Three main factors are contributing to this: (i) longer FL pump pulses, (ii) cooling the LN crystal to reduce its absorption, and (iii) large pump spot size and energy. According to the calculations the THz peak electric field strength can be increased by more than a factor of four to the MV/cm level directly at the crystal output by using 600-fs pump pulses instead of the commonly used 100-fs. The calculations predicted the increase of the THz peak electric field strength by about one order of magnitude when the crystal is cooled to 10 K and 500-fs pump pulses are used, rather than pumping with 100-fs pulses at room temperature. The use of imaging can increase the peak electric field strength to the 10-MV/cm level. An optimized pump pulse duration and a cryogenic crystal temperature in combination with the contact-grating technique was predicted to allow the generation of THz pulses with focused peak electric field strength on the 100-MV/cm level and tens-of-mJ energy, driven by efficient sub-joule class diode-pumped solid-state lasers. The prediction of highly efficient sources of ultra-intense THz pulses presented here opened the perspective for new applications, such as particle acceleration and manipulation [27, 32, 100, 101].

5.2. Pulse-front tilting setups for large pumped area

Our calculations for TPFP in LN presented in Section 5.1 predicted the significant increase of the THz generation efficiency and peak field strength. For such a potential

increase, three main contributions were identified: (i) the use of an optimal (longer) FL pump pulse duration, (ii) cryogenic cooling of the crystal to reduce its absorption, and (iii) a large pump spot size and energy. The scalability by increasing the pump spot size and energy is an important advantage of TPFP over OR based on the electro-optic Cherenkov effect with a focused [35] or line-focused beam [139]. In order to fully exploit this scaling potential for the generation of THz pulses with extremely high (≳1 mJ) energy, a large pump spot size up to several cm is needed.

A conventional TPFP setup consists of a femtosecond pump laser, an optical grating, an imaging lens or telescope, and the nonlinear material [24, 40, 58] (Figure 28). However, the disadvantage of this setup is that imaging is subject to distortions which can influence or even restrict THz generation by limiting the useful pump spot size [41, 132]. Previous ray-tracing analysis of the TPFP setup showed no significant distortions, however, it was restricted to only 1 mm beam diameter on the entrance surface of the crystal [140]. This is much smaller than the spot size used in first benchmarking experiments with μJ-level THz pulse energy [60] and the cm-large spot size required for still higher THz pulse energies.

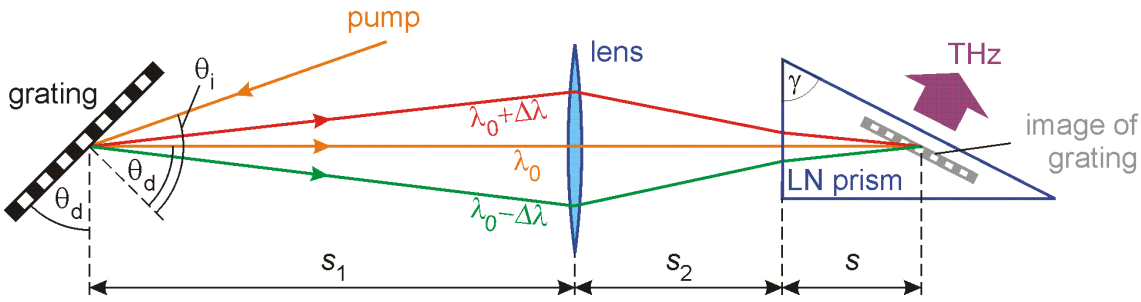

Figure 28. Scheme of a TPFP setup using a reflection grating for PFT, a lens for imaging and a LN prism for THz generation.

The necessity of large pump spot sizes and the possible limitations associated with it prompted us to investigate in more detail the role of imaging errors in a LN-based TPFP setup [41, 132]. A related goal was to reduce or even to eliminate such errors in optimized setups.

With the help of numerical simulations different TPFP setups were characterized in terms of pump pulse distortions and their effect on the THz yield in the plane of grating dispersion. The pulse front and the varying pulse duration across the pump beam were obtained from calculating the group delay by ray tracing [132, 140]. The THz generation was described by a model similar to that described in Section 5.1, however extended to two spatial dimensions in order to account for a finite beam size.

Inside the LN crystal, the pump pulse duration changes with propagation distance due to GVD from angular dispersion. The FL pulse duration is restored along the image of the grating. Ideally, this image surface is a plane, coincident with the pulse front, both of them tilted by the same angle defined by phase matching. Such an ideal case would result in uniform pump intensity, and consequently, in uniform THz generation efficiency along this tilted plane, and also in flat THz wavefronts. However, due to imaging errors, usually both the image surface and the pulse front are curved, and also deviating from

each other. The result can be a strongly non-uniform pump intensity and THz generation efficiency across the tilted pulse front, together with curved THz wavefronts.

The black solid curve in Figure 29a shows the variation of the THz generation efficiency across the pump beam in the plane of angular dispersion, calculated along an assumed ideally flat tilted pulse front (x-axis in Figure 21). Here, a conventional single-lens imaging setup was investigated, as used in earlier experiments [59, 60]. A 2000-lines/mm grating was illuminated by a Gaussian beam of 5 mm $1/e^2$-width and pulses of 100 fs duration. The wavelength was 800 nm. The grating was imaged with a demagnification of two onto a 2 mm thick LN crystal by a 75-mm focal length achromat lens. Phase matching was set to 0.5 THz. As can be seen in Figure 29a, the THz generation efficiency varies by as much as five orders of magnitude across the pump spot. For comparison, the efficiency varies in the perpendicular direction by only a factor of two (not shown).

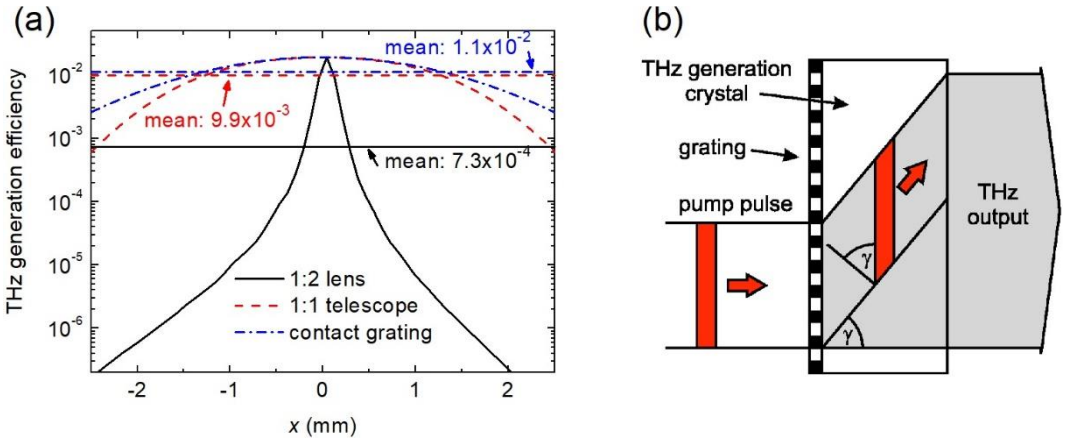

Figure 29. (a) Calculated THz generation efficiency across an extended pump beam for different TPFP setups. (b) The scheme of a contact-grating THz source. From Ref. [132].

The variation of the THz generation efficiency across the pump spot is reduced to less than two orders of magnitude resulting in 14-fold increase of the mean THz generation efficiency with an optimized setup [132] where a 1:1 imaging telescope is used (red dashed curve in Figure 29a). Using a telescope rather than a single lens reduced the pulse front curvature and the variation of the pulse duration across the pump spot.

To fully exploit the scaling potential of TPFP we proposed a contact-grating technique which is exempt from all kinds of imaging errors [132]. In this simple scheme the imaging optics is omitted and the grating for PFT is formed directly on the entrance surface of the nonlinear crystal (Figure 29b). The contact-grating scheme enables the construction of alignment-free monolithic THz sources. It is easily scalable to higher THz energies by simply increasing the pumped area. It can provide an excellent THz beam quality resulting in diffraction-limited focal spots and highest possible electric fields.

The contact-grating setup can provide an even higher efficiency than the setups with imaging (blue dashed-dotted curve in Figure 29a). It is obvious, that in this scheme there is no principal limitation on the pump spot size. A completely uniform THz generation efficiency of 1.1% was obtained over the entire beam, which is 15 times larger than the efficiency of the 1:2 imaging setup. In the calculation, a 2400-lines/mm grating was assumed. More importantly, the contact-grating scheme allows to increase

substantially the pump spot size to several cm without significant pulse distortions, thereby enabling the THz pulse energy to be increased further by several orders of magnitude by using large pump energy. We note that limitations in this scheme can arise from temporal broadening of the pump pulses due to grating angular dispersion [122] and material dispersion in the crystal. Whereas this type of distortion is also present in the setups with imaging, it is negligible with respect to much larger distortions due to imaging errors in case of large beam sizes.

Ideally, in the contact-grating scheme a blazed transmission grating [119] is used. A grating with equal efficiencies in the ±1st orders, such as a holographic grating could also be used. Both orders generate THz radiation with the same phase, and equal intensity. The period of the spatial intensity modulation generated by the interference of the two diffraction orders is on the order of the optical wavelength, and does not influence the THz wave. With all grating types the use of an index matching medium is necessary in LN due to its large refractive index [141, 142]. The realization of an efficient semiconductor contact-grating THz source, without the need for index matching, is demonstrated in Section 7.2.

THz beam profiles

The pulse-front-tilting setup used in many previous experiments [40, 60, 61] consisted of a grating and a lens. However, as discussed above, even if an achromatic lens is used the remaining geometric aberrations can lead to efficiency reduction and to distorted THz phase fronts for an extended pump beam. Such effects can limit experimental applications and high-energy THz pulse generation, which requires an extended pump spot due to pump intensity limitations.

Owing to the noncollinear phase matching scheme, more accurate predictions require at least a two-dimensional (2D) model of THz generation. In the preceding discussion, the THz generation efficiency was estimated inside the LN crystal only along a plane parallel to the ideal tilted pulse front. However, the pump pulse duration not only varies along this plane and the THz output is determined by the interference of contributions from the entire interaction range. Therefore, we developed a more realistic 2D model of THz generation in a TPFP scheme [41], where the variation of the pump pulse duration in the plane of angular dispersion (xy-plane in Figure 21) is accounted for. The pump pulse duration was calculated by the ray tracing method described in [140]. The nonlinear crystal was decomposed into thin slabs of equal thickness parallel to the pump pulse fronts (x-axis) and the wave equation was solved numerically for each slab with varying pump pulse duration across the pump spot. The THz spectral amplitude was summed up in the THz propagation direction (z-axis in Figure 21), thereby accounting for the non-collinearity of the THz generation process. This model enabled us to predict the output THz beam profile.

In the calculations 800 nm wavelength, 100 fs FL pulse duration, and Gaussian beam profile with 5 mm $1/e^2$ diameter were assumed for the pump. The calculated THz beam profiles can be seen in Figure 30d for three different TPFP setups shown in Figure 30a-c. In case of setups (a) and (b) the PFT is introduced by a grating-lens system (not shown in Figure 30). The groove density of the grating was 1800 lines/mm (a), and 1600 lines/mm (b), and the lens focal length was f = 75 mm for both setups. Setup (a) is

an optimized one (for details see [41]), where the tilted pump pulse front (red solid curve inside the LN prism) coincides with the image of the grating (black dashed curve) at the pump beam centre. The colour plot inside the LN prism shows the spatial distribution of the local THz generation efficiency, which is analogous to a long-exposure photo (rather than a snapshot). The local THz generation efficiency is highest along the image of the grating, where the pump pulse duration is shortest (the group delays of short- and long-wavelength spectral components are equal). The image of the grating has stronger curvature than that of the pump pulse front, which introduces asymmetry with respect to the THz wavefronts. This leads to a moderately asymmetric THz beam profile with 9.3 mm $1/e^2$-width (red solid line in Figure 30d).

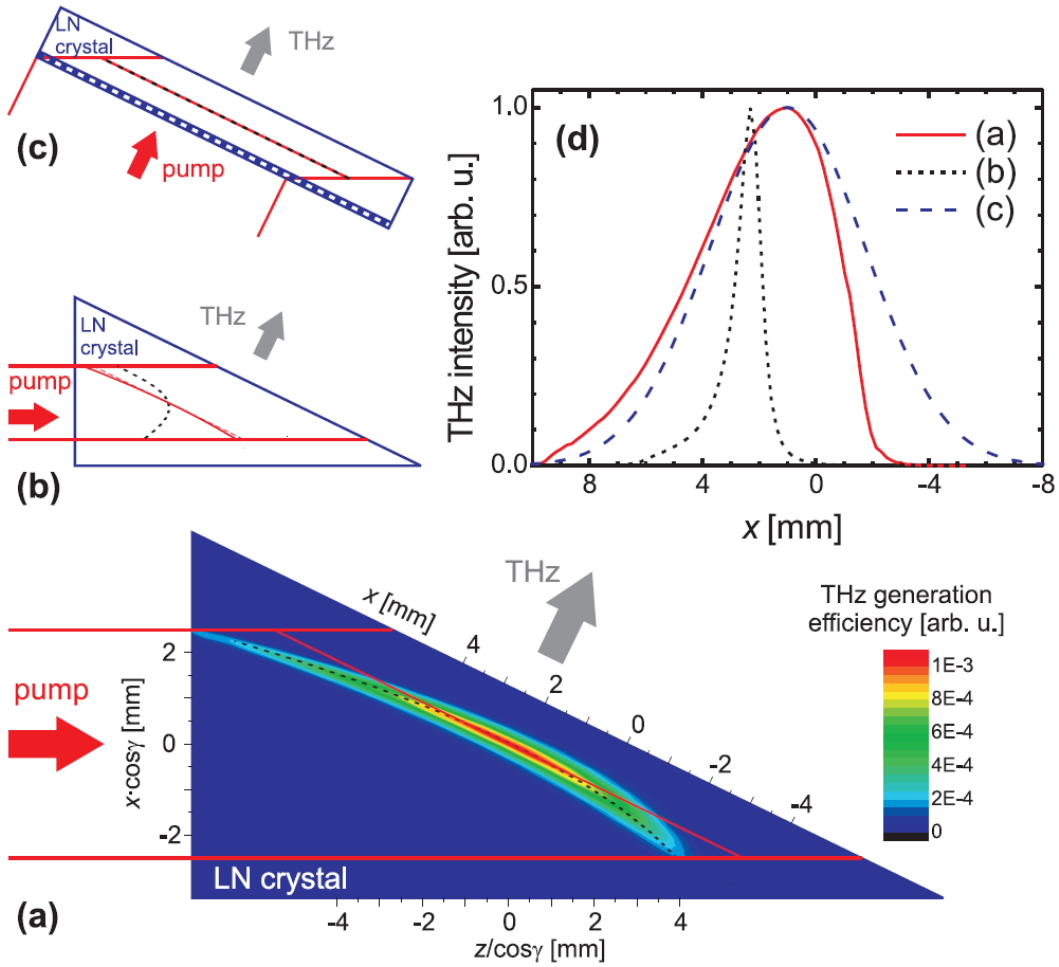

Figure 30. Three different TPFP setups (a-c) with their respective calculated output THz beam profiles (d). From Ref. [41].

By using a non-optimized setup (Figure 30b), where the grating's image has a much stronger curvature, and a different slope at beam centre than the pump pulse front, the asymmetry becomes more pronounced. In addition, a strongly narrowed THz beam can be observed (black dotted curve in Figure 30d), caused by the narrower projection of the THz generating region, extending along the grating's curved image, onto the THz wavefronts. A THz beam with such narrow-peaked (2.5 mm $1/e^2$-width) asymmetric beam profile, and the corresponding large divergence is disadvantageous for many applications even if the THz energy is similar to that in the optimized case. This result clearly reveals THz beam asymmetry and narrowing, in addition to THz wavefront

curvature, as a consequence of imaging distortions. For example, measurements of Stepanov et al. [61] using a nonoptimized TPFP setup revealed a THz beam divergence of 133 mrad, significantly larger than the diffraction limit of 48 mrad (estimated from the spot size), as well as an asymmetric THz beam profile.

In contrast, the contact-grating setup (Figure 30c) contains no imaging optics and therefore is free of imaging errors. The loci of shortest pump pulse duration lie exactly along the plane pump pulse fronts. This results in flat THz wavefronts and a symmetric THz beam profile (blue dashed curve in Figure 30d).

In summary, a two-dimensional model was developed for the simulation of the THz generation in a TPFP scheme with an extended pump beam. Our calculations revealed a strongly varying local THz generation efficiency and distorted output THz beam profile in a conventional TPFP setup with non-optimized imaging. A significantly improved uniformity in the local THz generation efficiency across the beam and reduced THz beam distortion was shown for a TPFP setup with optimized imaging. A novel TPFP setup was introduced based on a contact grating without imaging optics. Such a setup can enable large-area pumping with uniform THz generation efficiency and flat THz wavefronts with excellent focusability. These are essential features for the generation of extremely high THz pulse energies and peak field strengths.

TPFP setups with optimized imaging were used in our high-energy THz pulse generation experiments discussed in Section 5.3. The realization of a LN contact-grating THz source turned out to be very challenging [141, 142]. We carried out successful proof-of-principle THz generation experiments using a prototype ZnTe contact grating with a sinusoidal profile, fabricated by laser ablation and pumped at 1.7 μm wavelength [126]. Further work was needed to optimize the diffraction efficiency of the grating for example by using a binary profile rather than a sinusoidal [119, 143]. The demonstration of a highly efficient contact-grating THz source is discussed in Section 7.2.

5.3. Efficient generation of high-energy THz pulses

In Section 5.1 it was shown by numerical calculations that the THz generation efficiency can be significantly increased by using longer FL pump pulses, cooling of the LN crystal to reduce its THz absorption, and using a large pump spot size and energy. These improvements can enable a more efficient use of a much longer interaction length for THz generation. The typical FL pump pulse duration used in previous experiments was about 100 fs [31, 62, 63, 87, 89]. In contrast, our calculations predicted an optimum FL pump pulse duration of about 500 fs with 6× larger THz generation efficiency at room temperature than for 100 fs [126], with further room for improvement by cryogenic cooling of LN. Furthermore, a detailed theoretical analysis of LN-based TPFP sources was given [41, 126, 144], and optimal parameters for the pulse-front-tilting setup containing imaging optics were defined [41], in order to reduce distortions and to allow increasing the pump spot size. It was our goal to verify in experiments the prospects predicted by these calculations.

In this Section our experimental results on highly efficient generation of THz pulses by OR from a LN-based TPFP source are summarized. These results represented

record high THz pulse energies and pump-to-THz energy conversion efficiencies. The essential point was to use longer (sub-ps and ps) pump pulses, as suggested by our theoretical predictions, rather than the commonly used ~100-fs pulses.

The perspective of long pump pulses

In our first experiment, a diode-pumped high-energy picosecond Yb:YAG CPA laser was used as the pump source. It had 10 Hz repetition rate, 1030 nm central wavelength, and 2.6 nm FWHM spectral bandwidth [145]. The pulses were compressed to about 1.3 ps duration containing a remaining third- (and higher-) order spectral phase. Thus, the pump pulse duration was significantly longer than the FL and the calculated 500 fs optimum for THz generation. Nevertheless, they were suitable to test and verify the general trend in THz generation for increasing the pump pulse duration. Up to about 70 mJ pump pulse energy was used in the experiment.

A TPFP setup with optimized imaging [41] was used for THz generation in a large LN crystal. The intensity front of the pump pulses was tilted by a 1400-lines/mm grating and imaged by a 20-cm focal length lens of 25 mm diameter, with a demagnification of 1.7, into the 0.6% MgO-doped stoichiometric LN crystal. A λ/2 plate was used to rotate the horizontally polarized pump light from the grating to vertical polarization, parallel to the optic axis of the LN crystal. The pump spot size on the crystal surface was 6.8 mm in the horizontal direction and 13.0 mm in the vertical direction (at $1/e^2$-value of the peak intensity). A prism shaped LN crystal was used (inset in Figure 31a). The size of the input surface was 13×16 mm^2 (horizontal×vertical), which allowed a maximum pumped area of 8.1×16 mm^2. After losses at the grating and elsewhere, approximately 53 mJ of maximum pump energy reached the crystal. A calibrated pyroelectric detector (Microtech Instruments) with 2×3 mm^2 active area and a cone-shaped input opening with 15 mm diameter was used for measuring the energy of the THz pulses. Silicon plates were placed in front of the detector in order to attenuate the THz pulses to avoid saturation, and to block the optical radiation. The voltage signal of the detector was fed to a storage oscilloscope and the THz energy W_{THz} was calculated from the voltage modulation V_{m} of the recorded trace according to $W_{\mathrm{THz}} = CV_{\mathrm{m}}\tau/S$, where the sensitivity $S = 700$ V/W was obtained from factory calibration, while the correction factor $C \approx 1$ and the time constant $\tau = 25$ ms were determined from fitting of the recorded trace.

The measured THz energy is shown in Figure 31a as the function of the pump pulse energy before the LN crystal. A continuous increase in the THz energy can be observed up to about 50 mJ pump energy. The increase of THz energy with increasing pump energy followed a power law with a power dependence of about 1.6 up to above 20 mJ pump energy (dashed black line in Figure 31a). Above this pump level the increase in THz yield was weaker. A maximum THz energy of 125 μJ is reached at 50 mJ pump, giving a pump-to-THz energy conversion efficiency of 0.25%. At higher pump energy the decrease of the THz energy was observed. This can be attributed to the occurrence of 4PA at the pump wavelength and the corresponding increase in FCA in the THz range. The conversion efficiency was increasing from 0.08% at 4 mJ pump energy to its maximum of 0.26% at 45 mJ pump energy.

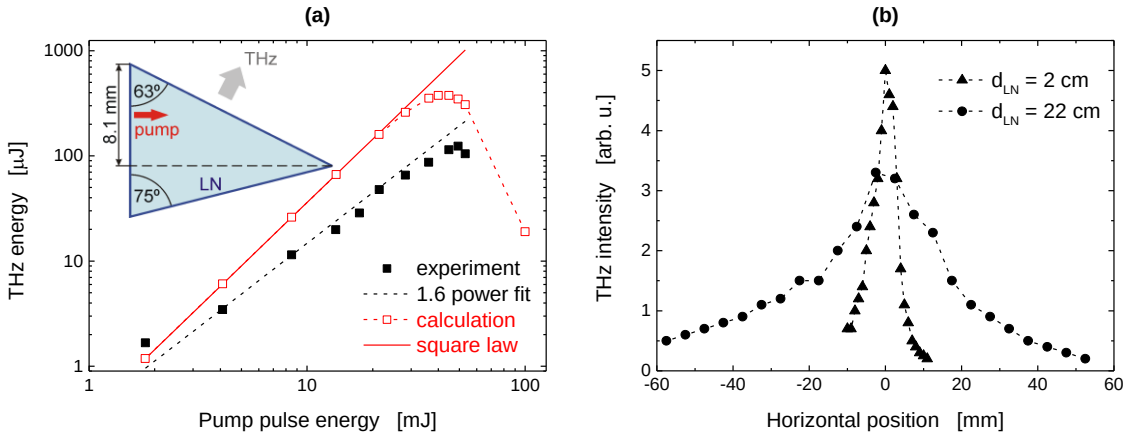

Figure 31. (a) Measured and calculated THz energy as functions of the pump pulse energy. The inset shows the geometry of the LN crystal. (b) Measured THz beam profiles at 2 cm and 22 cm distances behind the output surface of the LN crystal. From Ref. [146].

The model described in Section 5.1 was used for the simulation of the experimental data, including FCA caused by 4PA of the pump. An estimated value of 10^{-7} cm^5/GW^3 was used for the 4PA coefficient [44]. The deviation of the calculated THz pulse energy (red empty-square symbols in Figure 31a) from the square law (red solid line in Figure 31a) above ~20 mJ pump energy is due to 4PA. The theoretical curve shows about three times higher maximum THz energy as the measured maximum, whereas the difference decreases with decreasing pump energy. The pump energy corresponding to the calculated maximum THz energy is about 42 mJ, which is in reasonably good agreement with the experimental finding (50 mJ). Because LN has a bandgap of 3.8 eV at room temperature, at the pump wavelength of 1030 nm only 4PA and higher-order MPA should be possible in a perfectly pure material. However, impurities can cause 2PA. This can be a reason that the observed increase in the THz yield below ~20 mJ pump energy was weaker than the square law.

The pulse shape was not measured. However, previous experience showed that calculated and measured THz pulse shapes and spectra were in reasonably good agreement [39]. Due to the long pump pulse duration the peak of the calculated THz spectrum is at a relatively low value of 0.25 THz, where the dispersion of LN is small. Accordingly, the calculated temporal shape of the THz pulses comprised a single oscillation cycle [43].

Measured THz beam profiles in the horizontal plane (in the plane of pump angular dispersion) are shown in Figure 31b for 2 cm and 22 cm distances behind the output surface of the LN crystal. The measured THz beam diameter is about 33 mm (FWHM) at 22 cm. Assuming a plane THz wavefront at the output surface of the crystal with a Gaussian THz beam waist calculated from the square of the projected input pump beam profile gives only 19 mm THz-beam FWHM at the larger distance, 1.7× smaller than the measured value. If the curvature of the THz phase fronts is also taken into account, which is present even in an optimized TPFP setup, as predicted by ray tracing calculations [41], about 33 mm FWHM is obtained for 22 cm distance, which is in agreement with the experimental finding.

Figure 32 shows the calculated pump-to-THz conversion efficiencies, where the FL pump pulse duration was varied while its peak intensity was kept at the constant value of 20 GW/cm^2. At room temperature the highest efficiency (2%) is predicted for 500 fs pump pulse duration (red curve with empty-square symbols in Figure 32). This is about two times higher than the efficiency calculated for 1.3 ps FL pump pulse duration (1.1%). If we take into account also the uncompensated third-order spectral phase present in the experiment, the calculated THz yield gets further reduced to 0.74% (black empty-square symbol in Figure 32). The reason for the reduced efficiency is the reduced interaction length due to the larger spectral width. In this case the angular dispersion introduced by the TPFP setup causes a faster variation of the pump pulse duration inside the LN crystal [41, 126]. The corresponding experimental value (0.22%), obtained with about 21 mJ pump energy, is also shown in Figure 32.

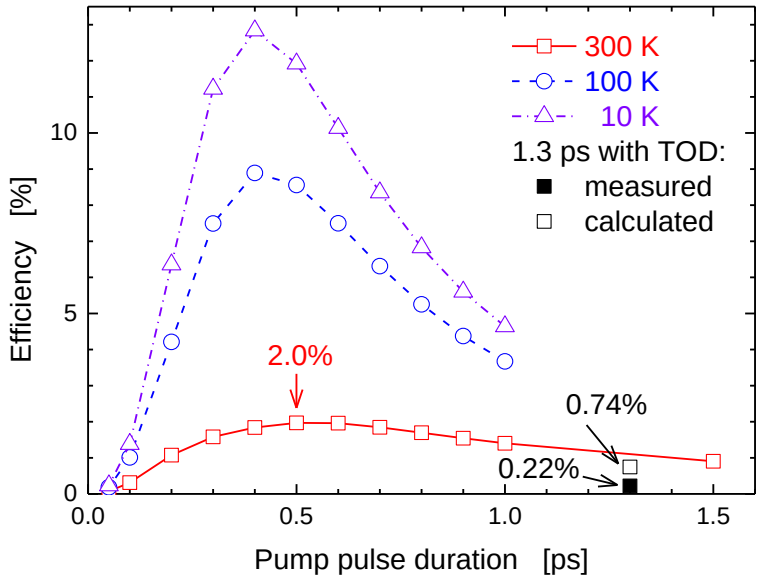

Figure 32. Calculated THz generation efficiency as function of the FL pump pulse duration for various crystal temperatures. TOD: third-order phase. From Ref. [146].

Even though our pump pulses were longer than optimal, the experimentally obtained THz generation efficiency (up to 0.25%) was 2.5 times higher than the previously reported highest value [63], and 5× higher than the efficiency for the previously reported highest THz energy [62]. These results clearly supported the prospects of generating THz pulses with mJ-level energy by using longer pump pulses. The THz generation efficiency can be improved further by cooling the LN crystal to reduce its absorption (Figure 32).

In conclusion, THz pulses with a record-high 125 μJ energy and 0.25% efficiency were generated by OR of 1.3-ps pulses in LN at room temperature. Our experimental findings together with theoretical predictions indicated the feasibility of efficient THz pulse generation with mJ-level output energy by using optimal pump pulse duration, cooling the LN crystal, and using a contact grating for TPFP to allow an even larger pumped area.

THz pulses with >0.4 mJ energy

Increasing the THz pulse energy to 125 μJ was a significant step forward, showing the potential of longer pump pulses. However, the pulse duration was much too long and far

from FL. In order to better exploit the potential of longer pump pulses and to verify the theoretical predictions more directly we carried out further experiments with improved pumping conditions. The result was a further substantial increase of the THz pulse energy to another record-high value exceeding 0.4 mJ [102]. The key point was to use a close-to-optimal pump pulse duration.

A diode-pumped high-energy picosecond Yb:YAG CPA system was used as the pump laser with 10 Hz repetition rate, 1030 nm central wavelength, and 3.4 nm FWHM spectral bandwidth [145]. The pulses were compressed to about 785 fs duration containing a small remaining third- and higher-order spectral phase. This pump pulse duration, while still longer than the theoretically predicted ~500 fs optimum for THz generation in LN, was significantly closer to this optimum and to the FL than the pulses used in our preceding experiment. The amplitude and phase structure of the pump pulses were characterized by a single-shot SHG FROG apparatus. The pump beam diameter was 26 mm (FWHM). Up to about 60 mJ energy was used in the experiment.

The experimental setup is shown in the inset of Figure 33a. The intensity front of the pump pulses was tilted by a 1400-lines/mm grating. A $\lambda/2$ retardation plate was used to rotate the horizontally polarized pump light diffracted from the grating to vertical polarization, parallel to the optic axis of the LN crystal. A TPFP setup with an imaging telescope was used since our ray-tracing calculations predicted smaller curvature of the tilted pulse front than that with single-lens imaging [41, 132]. This feature is beneficial for achieving high conversion efficiency with cm-size large pumped area. The telescope consisted of one 25-cm focal length 50-mm diameter lens and one 15-cm focal length 25-mm diameter lens in confocal arrangement. A vacuum tube, placed between the two lenses, was used to avoid nonlinear beam distortions and plasma formation in air near the focal plane of the first lens. A 0.6% MgO-doped stoichiometric LN prism at room temperature (RT) with a useful input surface of 8.1×16 mm^2 (horizontal × vertical) was used for OR (see inset in Figure 31a). In addition, a spherical mirror telescope with a demagnification of 2.5:1 was used to reduce the incoming pump beam diameter before the TPFP setup in order to achieve a high pump intensity at the LN crystal. The pumped area on the crystal surface was relatively small, its diameter was 5.7 mm in the horizontal direction and 7.0 mm in the vertical direction, both FWHM.

The same calibrated pyroelectric detector was used for measuring the energy of the THz pulses as in our previous experiment described above [146]. A silicon wafer of 0.5 mm thickness with 70% measured transmission and a cardboard plate with 80% transmission were placed in front of the detector to block the optical radiation (the fundamental pump and its second harmonic). In some cases additional cardboard plates were used to further attenuate the THz pulses in order to avoid saturation of the detector. In each case the transmission of the filter assembly was carefully measured. The THz energy was calculated from the voltage modulation of the detector signal in the same way as in the previous experiment [146].

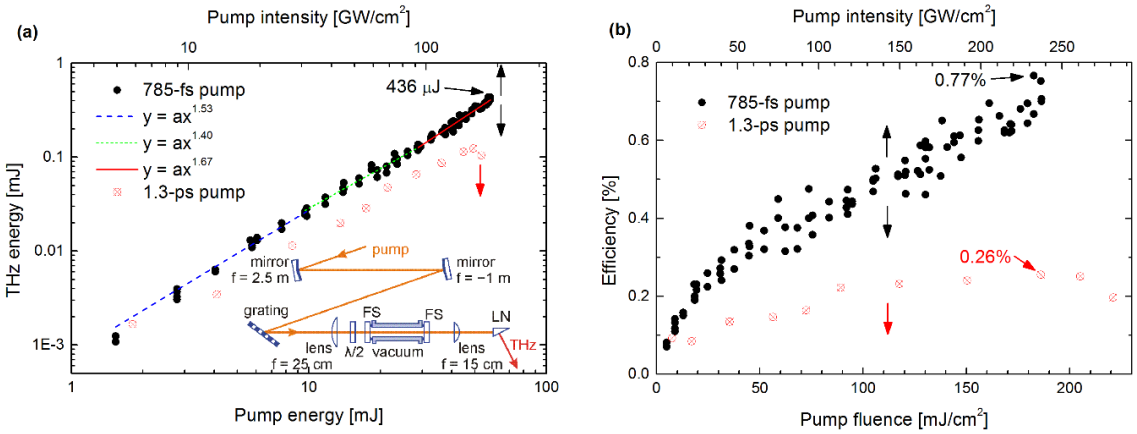

Figure 33. Measured THz energy vs. pump energy and intensity (a), and the corresponding efficiencies vs. pump fluence and intensity (b). The black symbols show measurements with 785-fs pump pulses, whereas the red symbols show our previous experiment using 1.3-ps pump pulses [146]. Both intensity scales refer only to the case of 785-fs pump, as indicated by the vertical arrows. The inset in (a) shows the experimental setup with the shorter pump pulses. From Ref. [102].

The measured THz energy at RT is shown in Figure 33a as function of the pump energy (bottom scale) and intensity (top scale) before entering the LN crystal. The maximum pump energy was 58 mJ, the maximum intensity 237 GW/cm^2. A monotonic increase of the THz energy with increasing pump energy can be observed in the entire range. We note that this behaviour is distinctly different from our previous observation using significantly longer (1.3 ps) pump pulses but similar (only 23% smaller) pumped area [146], where the THz energy started to decrease above 45 mJ pump energy (Figure 31a). By fitting power functions to the measured data in different pump energy ranges (lines in Figure 33a) a decreasing power exponent with increasing pump energy was found. It is about 1.5 below 10 mJ and 1.4 in the range of 10 mJ to 30 mJ. Interestingly, above 30 mJ the exponent rises to almost 1.7. One possible reason for this effect could be the saturation of FCA in LN. Similar behaviour was observed in ZnTe and explained by the saturation of FCA at higher pump intensities [147]. Another possible reason is the nonlinear interaction of the generated intense THz field and the pump pulse, which can lead to a broadening of the pump spectrum and an increased pump intensity [46, 47, 124].

The maximum THz energy achieved in the present experiment was as high as 436 µJ, achieved with only 58 mJ pump energy. Corresponding pump-to-THz energy conversion efficiencies up to 0.77% were observed (Figure 33b). Measured efficiencies are shown in Figure 33b as function of the pump fluence (for better comparison with results from our previous experiment [146]) and intensity. It is monotonically increasing with increasing energy in the entire range. Above about 80 mJ/cm^2 fluence (corresponding to about 25 mJ energy) it is increasing linearly. Up to about 150 mJ/cm^2 (47 mJ), the saturation point of our previous measurement, we obtained about two times higher efficiencies with the presently used shorter pump pulses than with 1.3-ps pulses. This is in good agreement with our calculations [146], which predict 2.3-times increase for the shorter pump pulses being closer to optimum.

Cryogenic cooling

The measurements discussed above were carried out at room temperature. However, at RT a significant part of the generated THz pulse is dissipated inside the crystal due to the strong absorption of LN in the THz range (about 16 cm^{-1} at 1 THz, see Figure 24). The

absorption caused by anharmonic decay of the transverse optical phonon-polariton into two acoustic phonons can be strongly reduced by crystal cooling [148]. The temperature dependence of narrowband THz pulse generation using quasi-phase-matching in periodically poled LN was investigated and a 3-fold increase in conversion efficiency was found when cooling the crystal from RT to 18 K [149]. An increase in efficiency by a factor of 3.3 to about 4×10^{-5} was found for TPFP in LN cooled to 77 K, resulting in 100-pJ THz pulse energy [58]. Later, following our proposal of longer pump pulses [126], a close-to-optimum pump pulse duration of 680 fs was used in combination with cryogenically cooled cLN [150]. The 3-fold enhancement of the efficiency was reported when cooling from RT to 150 K for a pump energy of 1.2 mJ.

Our calculations, presented in Section 5.1, predicted a 3- to 6-fold enhancement in efficiency by cryogenic cooling of LN. It was our goal to experimentally verify the beneficial effect of cryogenic cooling on the THz generation efficiency for close-to-optimal pump pulse durations at high pump and THz pulse energies [102, 151].

Our first measurement series was carried out with a versatile Yb:CaF_2 laser [151]. The unique laser system consisted of a compact ytterbium oscillator, a grating-based stretcher-compressor assembly and a regenerative Yb:CaF_2 amplifier operated at RT. It delivered FL pulses of variable duration (380 fs–650 fs) with pulse energy of up to 15 mJ and centre wavelength of 1030 nm. From our previous theoretical investigations it was expected that such laser parameters are ideally suited for efficient THz generation. Both the conversion efficiency and the THz spectral shape were measured for variable pump pulse durations and for different crystal temperatures down to 25 K.

The maximum conversion efficiencies, 0.12% at RT and 0.36% at 25 K, were reached with the longest pump pulse duration of 650 fs both at RT and cryogenic temperature (CT). At 25 K the largest THz pulse energy reached 45 μJ. For any specific pulse duration, the conversion efficiency for cryogenically cooled LN was three to four times higher than at RT (Figure 34). The measured RT conversion efficiencies were similar to the values measured previously with longer pulses [146], and were below the theoretical predictions [126]. We note that our and other measurements were in contrast to the very high conversion efficiencies up to 3.8% reported in Ref. [150], whereas a similar efficiency enhancement by cryogenic cooling was found.

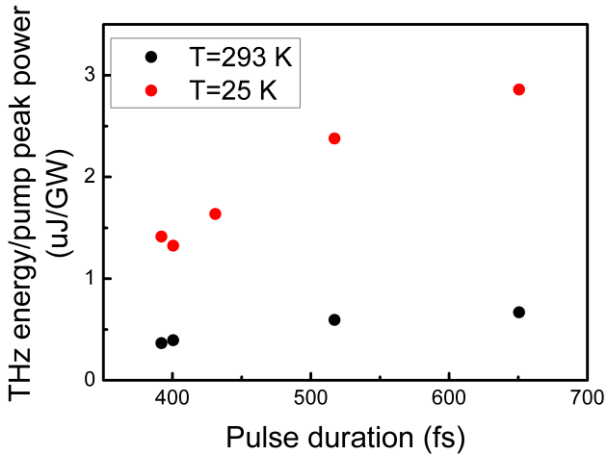

Figure 34. THz pulse energy normalized to the pump peak power as function of the FL laser pulse duration at $T = 293$ K and $T = 25$ K. From Ref. [151].

In Figure 34 the THz energy normalized to the pump peak power is plotted as function of the laser pulse duration for RT and 25 K. As expected from theory [126] the experimental data unravelled a dependence of the THz energy on the FL pump pulse duration. For the range of pump pulse durations available in the experiment the THz energy was increasing monotonically with increasing pump pulse duration. Similar behaviour was observed both at RT and CT. Besides the conversion efficiency, the change of the THz spectrum with the LN temperature and the pulse duration was also investigated. Measurement of the THz spectra by a Fourier-transform spectrometer at RT and CT for different pump pulse durations showed clearly that a shorter pump pulse gives rise to higher-frequency components. The enhancement of higher THz frequencies was observed for cooled LN because the high-frequency THz absorption is significantly reduced at CT. Our investigations also showed that broader THz spectra require shorter pump pulses, which inherently goes along with lower conversion efficiency, in accordance with calculations.

The second measurement series was carried out with the same high-energy Yb:YAG CPA system with a compressed pulse duration of 785 fs [145], which was used for the experiment resulting in the generation of THz pulses with >0.4 mJ energy described above [102]. This pump source enabled us to demonstrate the enhancement of conversion efficiency at CT up to more than 0.18 mJ THz energy. Key characteristics of high-energy THz pulses important for applications are the pulse energy, the temporal waveform, the corresponding spectrum, and the focusability of the THz beam. These parameters also determine the achievable focused peak electric field. In order to characterize these important features for our high-energy THz pulses, we carried out electro-optic sampling (EOS) and focal spot measurements, in addition to pulse energy scaling measurements.

In the TPFP setup (inset in Figure 35a) the same 1400-lines/mm grating and large-size LN prism were used as in the previous experiment with >0.4-mJ THz pulses. To enable an easier adjustment of the velocity-matching PFT angle, which changes with temperature, a 20-cm focal length near-infrared achromat lens was used for imaging. The PFT angle was fine adjusted by slightly shifting the lens (with a telescope one would have to change the input beam direction). As no beam-narrowing telescope was used for the input beam, the FWHM pump spot size at the crystal surface was large, 10.4 mm in the horizontal direction (out of which 8.1 mm was falling on the effective surface of the LN prism) and 15.3 mm in the vertical direction. The maximum useful pump energy was 30 mJ, the maximum intensity was 23.6 GW/cm^2. The latter was one order of magnitude smaller than used in the experiment described above with >0.4 mJ THz pulse energy. In order to compare high-energy THz pulse generation at RT and CT (23 K) the LN crystal was placed inside a closed-cycle helium cryostat with a fused silica input window for the pump and a polymethylpentene (TPX) exit window for THz. The vacuum chamber of the cryostat was equipped with an input port tube, holding the fused silica window, to bring the line focus of the near-infrared achromat lens into vacuum for avoiding nonlinear effects in air. The LN crystal was placed on a small aluminium table holder attached to the cold finger of the cryostat.

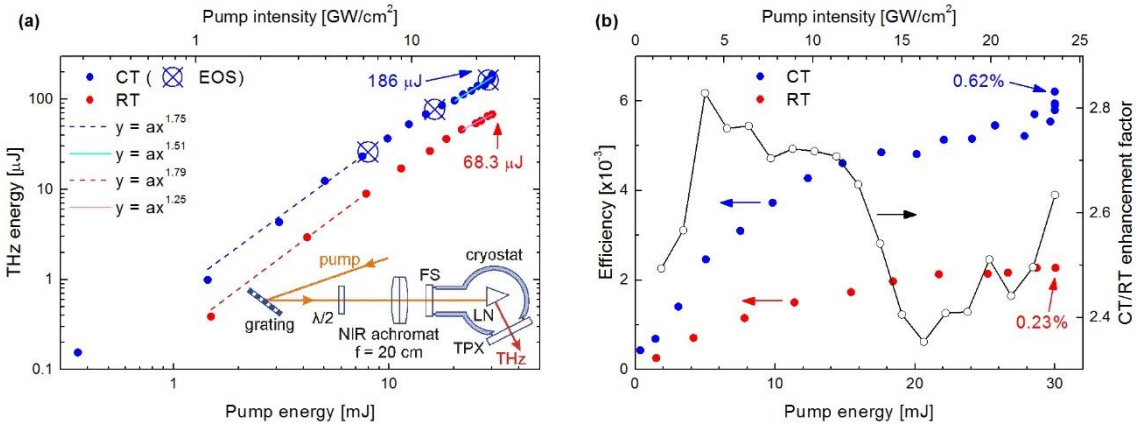

Figure 35. (a) Measured THz energy as function of pump energy and intensity at RT and CT. The crossed symbols refer to measurement points where EOS was also carried out. The inset shows the experimental setup. (b) The corresponding conversion efficiencies as functions of pump energy and intensity at CT and RT. The ratio of the CT and RT efficiencies, obtained by interpolation, is shown by the empty symbols. From Ref. [102].

The THz beam emerging from the LN source was collimated and focused by a pair of one 6-inch and one 2-inch effective-focal-length, 2-inch diameter, 90° deviation off-axis parabolic mirrors. The focal spot size was measured by the knife-edge technique. For measuring the THz temporal waveform by EOS the knife edge was replaced by a 0.1-mm thick (110)-cut ZnTe plate, attached to a 1-mm thick inactive ZnTe substrate. Two wiregrid polarizers were used to attenuate the THz beam in the collimated section to avoid the over-rotation of the induced birefringence in ZnTe [152]. Sampling pulses for EOS were taken from a small, apertured fraction of the pump beam (the zero-order reflection from the grating). Due to geometric constraints in the setup we used a reflection-type EOS setup, where the THz and the sampling pulses entered the detector crystal from opposite directions. It was the sampling pulse reflected internally from the outside surface of the active layer that copropagated with THz, and which was detected. The EOS signal was recorded by balanced detection consisting of a quarter-wave plate, a Wollaston prism, and two photodiodes. A lock-in amplifier with 10 Hz reference signal and 300-ms long integration time (i.e. averaging over 3 pulses) was used to improve the signal-to-noise ratio.

Our calculations predicted that the THz generation efficiency (η) can be enhanced by a factor of 3 to 6 when the LN crystal is cooled to CT [126]; the exact value depends on pump pulse duration and temperature. For 785-fs pump pulses an efficiency-enhancement factor of $\eta_{\mathrm{CT}}/\eta_{\mathrm{RT}} \approx 3$ to 4 can be expected. With such a dedicated measurement series, our goal was to investigate this effect for 100-μJ level THz pulse energies; that is, for energies much higher than that used in previous experimental studies [58, 150, 151].

The measured THz energies at RT and CT are shown in Figure 35a as function of the useful pump energy and intensity. A continuous increase of the THz energy can be observed for both temperatures in the entire range. The maximum THz energy is about 2.7-times higher at CT (186 μJ) than at RT (68 μJ), which is in good agreement with calculations [126]. The fitted power exponent (Figure 35a) decreases with pump energy from 1.8 below 10 mJ to 1.5 above 20 mJ at CT and from 1.8 to 1.3 at RT. Figure 35b shows the corresponding pump-to-THz energy conversion efficiencies as functions of the

useful pump energy and intensity. The conversion efficiencies are increasing with pump energy up to about 15 mJ (12 GW/cm^2 intensity). Above this level the efficiencies increase at reduced rates. The maximum measured efficiencies were 0.62% (CT) and 0.23% (RT). The ratio η_{CT}/η_{RT} of the CT and RT efficiencies (empty symbols in Figure 35b) is about 2.7 below about 15 mJ pump energy (12 GW/cm^2 intensity). This value is slightly smaller but still close to that predicted by the calculations. A pronounced drop of the efficiency enhancement factor to less than 2.4 can be observed in the narrow range between 15 and 20 mJ pump energies (12 GW/cm^2 and 16 GW/cm^2 intensities). The origin of this behaviour needs further investigation. At higher energies the enhancement factor increases slowly from about 2.4 to 2.6.

Examples of measured in-focus waveforms are shown in Figure 36a for three different THz pulse energies: $W_{THz} = 26$ μJ, 77 μJ, and 163 μJ, which correspond to 7.8 mJ, 16 mJ, and 29 mJ pump energies, respectively (see also the crossed symbols in Figure 35a). The waveforms are strongly asymmetric, comprised of less than one full oscillation cycle, with one dominating half-cycle. They show a positive chirp (low frequencies coming first). We note that the relatively strong noise mainly comes from the low repetition rate of the laser. A pronounced shift of the mean frequency to lower values with increasing THz pulse energy can be anticipated from the waveforms. There is also an increasing delay in the time instant of the peak position with increasing THz energy. The peak electric field strengths are 0.26 MV/cm, 0.45 MV/cm, and 0.65 MV/cm, as calculated from the measured waveform, pulse energy, and focal spot size. We note that it is important to take into account the low THz frequencies in our experiment when comparing these peak amplitudes to those in other experiments [63, 70, 76]. To our knowledge, in the low-frequency THz range accessed in our experiment, these results represented the highest reported electric fields.

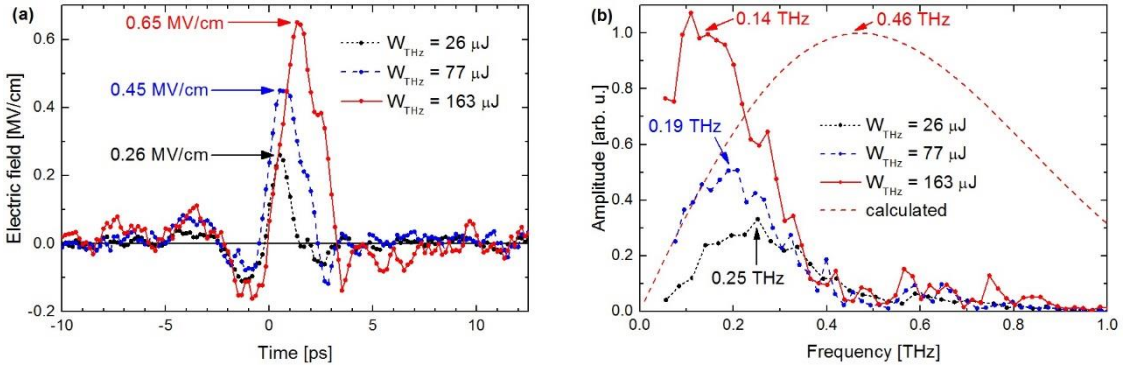

Figure 36. (a) Focused electric field waveforms measured by EOS. (b) Spectral amplitudes obtained from measured waveforms by Fourier transformation, in comparison with the calculated spectrum. From Ref. [102].

The spectral amplitudes of the THz pulses, obtained by Fourier transformation from the measured waveforms, are shown in Figure 36b. In all cases the spectra consisted of an intense low-frequency part, extending up to about 0.4 THz, and an adjoining weak part, with about one order of magnitude smaller spectral amplitude, extending up to about 1 THz. We note that similar spectral distribution was observed in our previous experiment with much smaller pump pulse energies [151]. Simulations based on the model described in our previous work [41] show somewhat broader spectra extending beyond 1 THz, however with the usual more uniform distribution (dashed curve without symbols in

Figure 36b) without any drop at around 0.4 THz. Another interesting feature is the decreasing frequency of the spectral peak with increasing pump and THz energy. It is about 0.25 THz for 26 μJ energy, and reduces to 0.14 THz for 163 μJ. In the simulation, no energy dependence of the THz spectra is present. In contrast to the peak frequency, the widths of the observed spectra show no significant energy-dependence, neither for the entire spectra nor for the more intense low-frequency parts. Gaussian fit to the latter gives spectral FWHMs varying in the 0.27 THz to 0.24 THz range. The reason for the observed spectral features needs further investigation, possibly including the role of impurities in the LN crystal, as well as pump- and THz-induced nonlinear effects.

The focal spot size was measured by the knife-edge method for the highest (29 mJ) pump energy. The measured data could be well fitted by assuming an elliptical Gaussian beam with $1/e^2$-radii of $w_H = 2.4$ mm in the horizontal and $w_V = 2.7$ mm in the vertical directions. A little astigmatism was observed, the horizontal and vertical foci being about 5 mm apart. We also carried out a measurement of the unfocused THz beam profile in the horizontal direction at various distances from the LN crystal. The THz beam size and wavefront curvature directly behind the LN crystal could be estimated from a fit to the measured profiles. A Gaussian beam calculation starting from these fitted values gave $w_{H,\,calculated} = 2.0$ mm for the horizontal focal spot radius, which is only slightly smaller than the measured value. The astigmatism can be attributed to the different THz wavefront curvatures in the horizontal and vertical directions due to imaging errors [41]. Increasing the THz field strength by achieving a focal spot being even closer to the diffraction limit could be expected from the aberration-free contact-grating technique [50, 132].

5.4. Nonlinear distortion of intense THz beams

In the development of intense THz sources primary attention was paid to the generation of ever higher THz pulse energies and field strengths. As the energy of THz pulses increased, limitations of efficiency inherent to the THz generation process were becoming important [136, 137]. For example, the limiting effect of pump angular dispersion was investigated for THz sources using TPFP in LN [41, 126]. The saturation of the conversion efficiency was reported [146, 153] and pump self-phase modulation (SPM) was suggested as explanation [153]. It was shown theoretically that the nonlinear interaction between pump and THz fields can pose a strong limitation on the interaction length for THz generation [47], thereby quenching the efficiency.

Whereas for many applications it is important to increase the THz yield further [27, 98, 154], little attention was paid to spatial characteristics of the generated THz beam, even though different methods are available for the measurement of beam properties [155-157]. The spatial emission characteristics of air plasma THz sources was studied [157, 158], but less detailed experiments were performed for TPFP in LN [159]. It was shown in Section 5.2 theoretically that distortions in the imaging system can lead to strongly distorted THz beam profiles [41], but possible distortion effects arising from nonlinear optical interactions were not considered. It was shown that in the THz range the nonlinear refractive index in LN is about three orders of magnitude larger than in the optical range [90, 92], which might cause some change of the beam through SPM. Here

we show, that in a TPFP source another effect, the nonlinear interaction between pump and THz fields, can lead to serious beam distortions [124]. Such effects can be important in high-field THz sources and application setups.

The nonlinear interaction between pump and THz fields can lead to the broadening of the pump pulse spectrum, implying the shortening of the FL pulse duration and, as a consequence, leading to the change of the interaction length for THz generation. The effective interaction length for THz generation L_{eff} [41] (Section 5.1), was defined as the distance measured in the THz propagation direction over which the THz intensity grows from 5% to its peak value. For large-diameter pump beams and small pump intensities this is determined by the variation of the pump pulse duration (and therefore of the pump intensity) with the propagation distance due to material and angular dispersions, and by the absorption at THz frequencies [41, 126]. Therefore, in this case there is a close relation between L_{eff} and the double dispersion length $2L_{\mathrm{d}}$. The double dispersion length gives the propagation distance, where the pump pulse duration does not exceed $\sqrt{2}\tau_0$ with τ_0 being the FL pulse duration (see also Figure 22).

At larger pump intensities, the generated THz field can be strong enough to significantly modify the pump spectrum [45-47]. In addition, the pump pulse can also be influenced by SPM [153]. In order to assess the influence of such effects on the dispersion and interaction lengths, numerical simulations were carried out on my initiative by solving the one-dimensional coupled wave equations for the pump and the THz fields. The model, similar to that described in Ref. [47], takes into account (i) the variation of the pump pulse duration (and therefore of the pump intensity) with the propagation distance due to material and angular dispersions, (ii) the non-collinear propagation direction of pump and THz beams (see also Section 5.1), (iii) the absorption at THz frequencies due to the complex dielectric function (determined by phonon resonances), (iv) the effect of the generated THz field on the pump field (i.e. sum- and difference-frequency generation between the optical and the THz fields), and (v) pump SPM.

Figure 37 shows the calculated variation of the pump pulse duration inside the LN crystal as function of the THz propagation coordinate z for 200 fs initial FL pulse duration and various fluence levels. At the lowest (0.037 mJ/cm^2) pump fluence it is dominated by the effect of angular dispersion (black solid curve in Figure 37a). As the fluence is increased, the nonlinear coupling between THz and optical fields (and to a smaller extent SPM) leads to an increasing broadening of the pump spectra. The combined effect of spectral broadening and angular dispersion leads to a rapidly decreasing pulse duration well below the original FL. This is shown by the curves in Figure 37a corresponding to higher pump fluence values. After reaching its minimum, an oscillatory variation of the pulse duration can be seen. The minimum pulse duration decreases from the original 200-fs FL at the lowest fluence to as short as 55 fs at the highest (37 mJ/cm^2) fluence. The corresponding double dispersion length $2L_{\mathrm{d}}$ decreases from 1.8 mm to as little as 0.1 mm. Figure 37b shows the corresponding variation of the pump-to-THz conversion efficiency η along the THz propagation coordinate z. Whereas the peak efficiency η_{max} increases with increasing pump fluence, the effective interaction length L_{eff} is decreasing (from 1.2 mm to 0.37 mm), in close correspondence to the dispersion length L_{d} (Figure 37a).

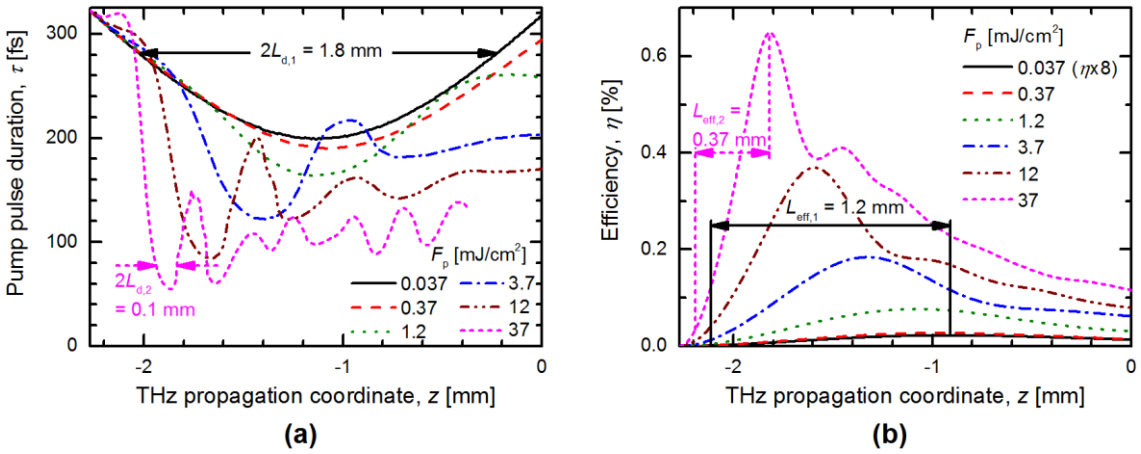

Figure 37. Calculated pump pulse duration (a) and pump-to-THz energy conversion efficiency (b) as functions of the THz propagation coordinate for various pump fluence levels. From Ref. [124].

Based on these simulation results, a simple qualitative reasoning indicates that the variation of the interaction length can results in a variation of the THz beam properties. This is schematically illustrated in Figure 38. With increasing intensity the dispersion length, and correspondingly, the effective length for THz generation decreases. This results in reducing the thickness of the THz-generating active region, with its centre shifting away from the output surface of the LN prism. As indicated in the figure, the consequence is the reduction of the THz beam size in the horizontal (x) direction, accompanied by a shift of the THz beam centre. No change in the beam profile is expected in the direction vertical to the plane of the noncollinear phase matching (y-direction). The reduced near-field horizontal THz beam size leads to an increased THz beam divergence at higher pump fluences. More accurate, quantitative predictions would require complicated two-dimensional simulations.

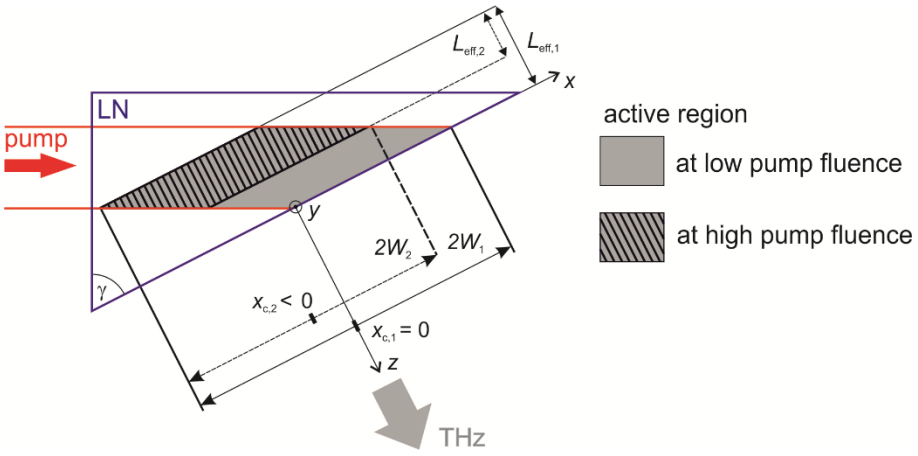

Figure 38. Horizontal beam size variation and beam centre shift originating from the combined effect of intensity-dependent interaction length and the noncollinear phase-matching geometry. From Ref. [124].

In order to validate the existence of such a nonlinear beam distortion effect we investigated experimentally the beam properties of the THz radiation emitted from a LN TPFP source with μJ-level energy [124]. This was the first experimental study carried out entirely in our High-Field Terahertz Laboratory at University of Pécs. We used our Yb:CaF_2 regenerative amplifier emitting 200-fs pulses of 7 mJ maximum energy at 1030 nm wavelength and 1 kHz repetition rate. THz pulses with up to 9 μJ energy were

generated in a LN prism at room temperature using TPFP. Details of the experimental setup can be found in Ref. [124].

Near-field THz beam profiles at various pump fluence levels were measured by a pyroelectric camera, whereby the output surface of the LN crystal was imaged onto the camera by two off-axis parabolic mirrors. Figure 39a shows the measured THz spot size as function of the pump fluence. A monotonic decrease of the horizontal spot size was observed, changing from about 2.5 mm at 5.3 mJ/cm^2 to about 2.1 mm at 31.8 mJ/cm^2. The vertical size remained essentially unchanged. Figure 39b shows the horizontal and vertical beam centre positions as functions of the pump fluence. In the horizontal direction a monotonic shift can be seen towards the crystal apex, corresponding to the $-x$ direction. The maximum shift is about -1 mm with respect to the position at the lowest pump fluence. The vertical position remained essentially unchanged. Such an intensity-dependent variation of the near-field beam profile is in accordance with the predictions from theory and the simple reasoning as discussed above.

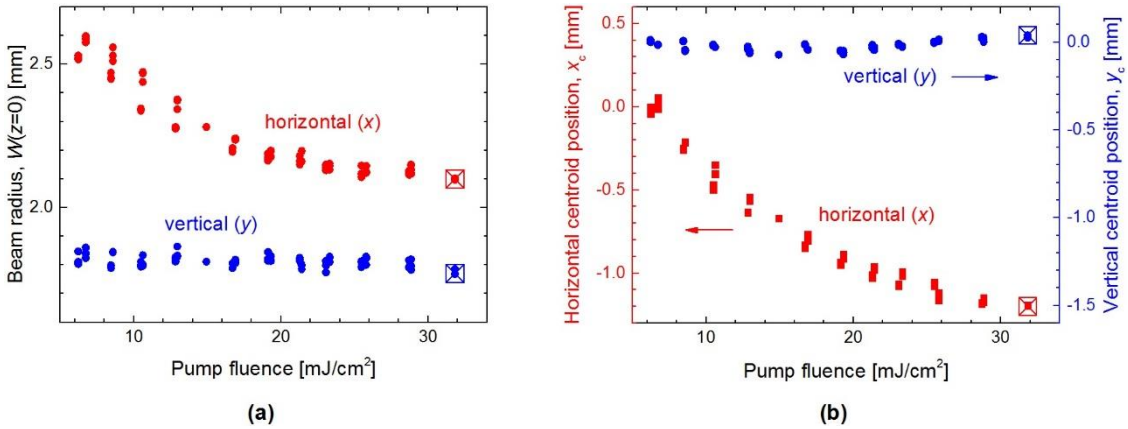

Figure 39. Measured horizontal and vertical near-field THz beam radii (a) and positions of near-field THz beam centroid (b) as functions of the pump fluence. From Ref. [124].

In the far-field, horizontal (x-axis) and vertical (y-axis) cross sections of the THz beam profile at different pump intensity levels were measured by a sensitive pyroelectric detector with xyz-positioning capability. A small-aperture iris diaphragm was placed in front of the detector to restrict spatial averaging effects. In the horizontal direction, the THz beam width increases dramatically with increasing pump fluence (Figure 40a). The horizontal and vertical beam radii and divergence angles at different propagation distances can be seen in Figure 40b and c, respectively. For simplicity, Gaussian beam propagation was assumed, with a frequency of 0.33 THz corresponding to the measured THz spectral peak. Obviously, the THz beam divergence in the horizontal plane increased dramatically (from 5.1° to 12.9°) with increasing pump fluence, whereas it remained essentially unchanged (~5°) in the vertical plane. Such an intensity-dependent variation of the divergence is in accordance with the observed variation of the near-field beam profile.

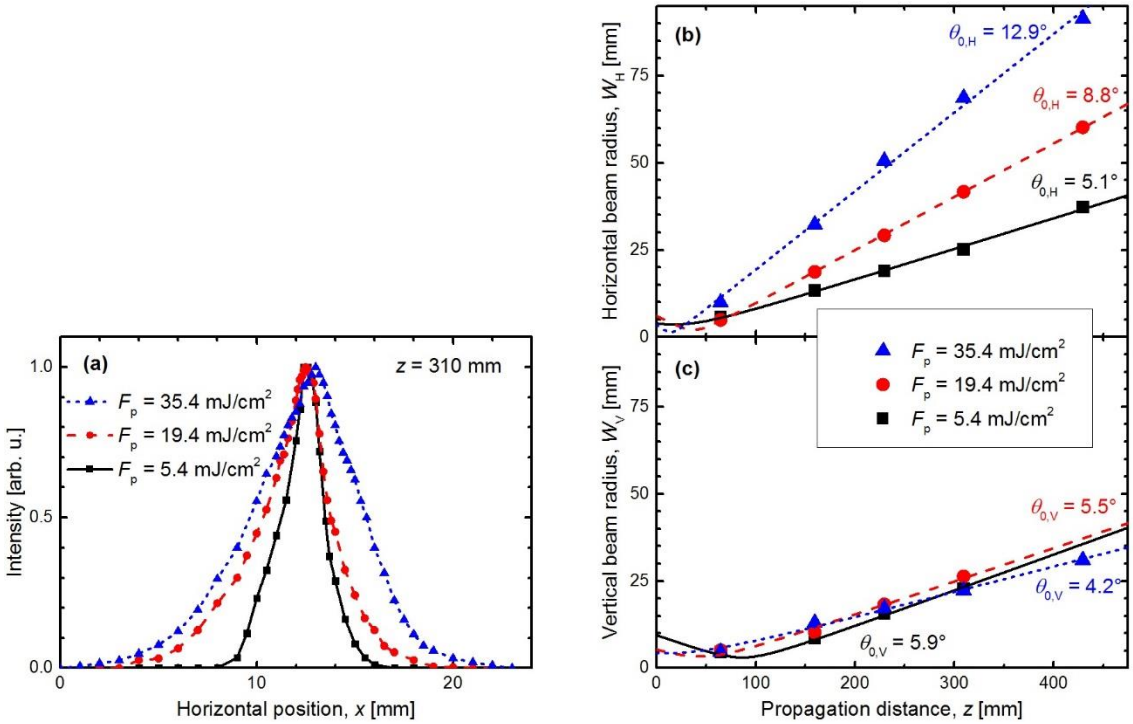

Figure 40. (a) Examples of measured horizontal THz beam profiles for different pump fluences at a z = 310 mm propagation distance behind the output surface of the LN crystal. Observed variation of horizontal (b) and vertical (c) THz beam radii as functions of the propagation distance. The fitted values $\theta_{0,H}$ and $\theta_{0,V}$ give the beam divergence (half opening) angles. From Ref. [124].

In summary, the strong decrease of the pump dispersion length and, consequently, the decrease of the interaction length for THz generation with increasing pump fluence was predicted by calculations for THz generation by TPFP in LN. Owing to the noncollinear phase matching, the changes in the interaction length result in changes in the horizontal THz beam size. This prediction was confirmed by near- and far-field THz beam profile measurements at varying pump fluence. The observed dependence of the THz beam properties on the pump fluence is highly relevant for designing THz sources and application setups, which include focusing or beam transport lines, and for measurement setups with variable pump intensity. The large nonlinear variation of the beam divergence can also seriously affect the spectral transmission of optical systems with limited aperture. These results are important for the rapidly developing research fields of THz nonlinear spectroscopy and high-field THz science.

6. High average power THz sources

Intense pulsed THz sources typically require pump pulses with multi-mJ energy, thereby usually restricting the pulse repetition rate below 10 kHz. Linear and nonlinear THz spectroscopic studies and other applications highly benefit from increased repetition rate, and there is a strong need to develop efficient THz sources with significantly higher (1–100 MHz) repetition rates. Fibre laser technology provides commercially available sources with superior stability and compactness delivering femtosecond pulses at high repetition rates but with moderate pulse energy (up to the 10-μJ level). It is challenging to design efficient THz sources based on optical rectification (OR) at these small or moderate pump pulse energies.

The efficiency of OR can be increased by cylindrical focusing, or by using waveguide or waveguide-like structures [139, 160-167]. In case of materials with high nonlinearity but strong absorption in the THz range, such as LN with $d_{33} = 168$ pm/V nonlinear optical coefficient and an absorption coefficient on the order of 10 cm^{-1}, it is important to suppress absorption. A promising way to achieve this is to sandwich a few μm thick LN layer between layers of significantly smaller absorption [160-164]. A suitable material for such a low-absorption cladding is silicon (Si). The structures reported previously were guiding only the optical pump [160-164] and the selected material parameters and dimensions did not allow wave guiding in the THz range. Therefore, the THz radiation leaves the LN layer through its boundary to the cladding. This reduces the propagation length of the generated THz radiation inside LN, thereby minimizing absorption losses. However, because of the reduced interaction length, the efficiency of THz generation is lower than it could be for a (velocity-matched) structure guiding both pump and THz. In the former case it is the intensity, while in the latter case it is the field strength of the THz components generated at different locations, which is summed up. Latter can enable to achieve a significantly higher THz generation efficiency. Although such double-waveguide structures were already introduced for phase matching of THz generation by parametric interaction [165] or optical rectification [166], the problem of absorption was not addressed in these works.

We introduced and numerically investigated a novel planar absorption-reduced waveguide (ARWG) THz source [168], where both the optical pump as well as the generated THz radiation are guided and, in addition, velocity matching is fulfilled for OR. The key point for efficient THz generation is a cladding of the THz waveguide with orders of magnitude smaller absorption coefficient in the THz range than that of the core. Appropriate waveguide design can ensure that 80%–95% of the THz energy propagates in the cladding. The absorption losses decrease with increasing power fraction propagating in the cladding. Velocity matching is achieved by TPFP.

In more detail, the ARWG THz source has a common core for both the optical pump and the THz radiation (Figure 41a), forming the nonlinear medium for OR. We assumed MgO-doped sLN as the core material, but other materials are also possible (e.g., ZnTe, GaP, CdTe, and DAST), where the absorption may originate from the material's complex dielectric function or from FCA generated by MPA of the pump. LN has a very large nonlinearity, but also strong absorption in the THz range (see Section 3.3), which reduces the pump-to-THz conversion efficiency. A suitable cladding material for guiding

THz radiation generated in the LN core is silicon (Si). The absorption coefficient of Si (~0.05 cm^{-1}) is more than two orders of magnitude smaller than that of LN. The THz refractive indices of both LN and Si are larger than the group index of LN at the typical pump wavelength of 1 μm. In this situation, velocity matching can be achieved by TPFP in the plane of the LN core (Figure 41b). As the typical penetration depth of the THz field into the Si core of the Si-LN-Si waveguide is on the order of 100 μm, in practical situations about 1 mm cladding thickness is sufficient.

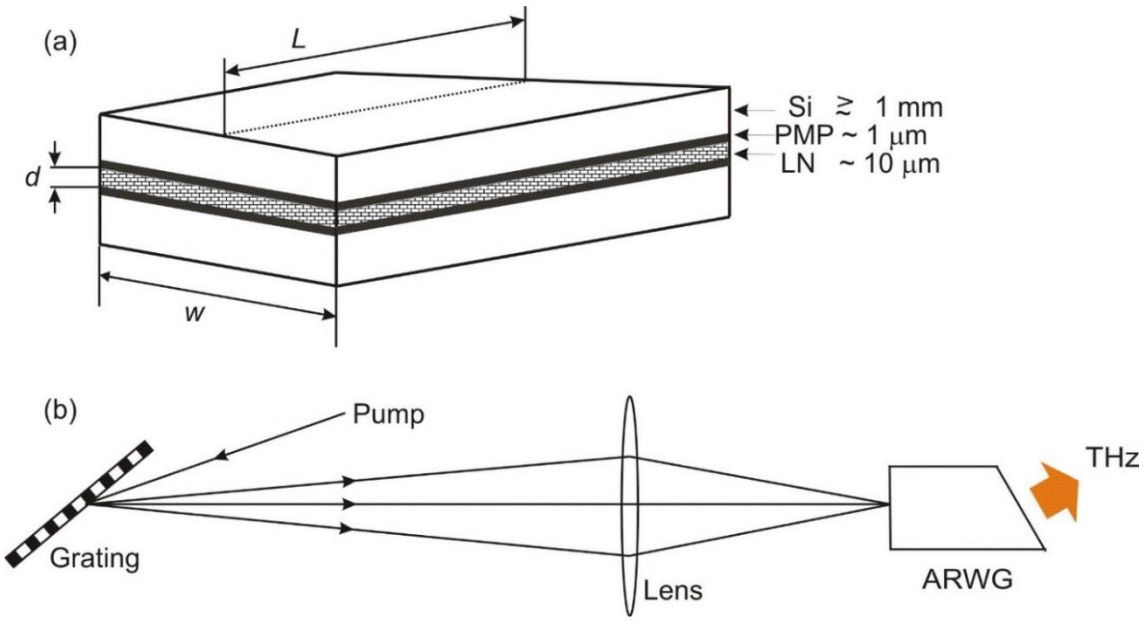

Figure 41. (a) The ARWG structure. (b) The ARWG THz source with TPFP (top view). From Ref. [132].

For typical pump wavelengths, the refractive index of the Si cladding is larger than that of the LN core, which prohibits wave guiding of the optical pump. To solve this problem an inner cladding was introduced between the LN core and the Si outer cladding (Figure 41a). Suitable materials for the inner cladding are, for example, polymers having smaller optical refractive index than that of the LN core and low THz absorption. It should also be transparent in the optical wavelength range of interest. One suitable material is polymethylpentene (PMP, often referred to as TPX), frequently used for THz applications. The thickness of the PMP inner cladding is advantageously chosen in the same order of magnitude as the pump wavelength. By this choice the influence of the PMP layer on the THz wave is negligible. At the same time it also prohibits the penetration of the optical pump into the Si outer cladding, since its penetration depth into the PMP is by one order of magnitude smaller than the PMP thickness. This is important in order to avoid free-carrier generation in Si, which could induce absorption in the THz range. Besides creating the necessary pulse front tilt for velocity matching, the TPFP setup has to provide mode matching of the incoming pump beam to the lowest-order mode of the inner PMP-LN-PMP waveguide. This can be easily achieved by inserting suitable (cylindrical) lenses either in front of or behind the grating.

Numerical simulations were carried out to explore the performance of the ARWG THz source. For the sake of simplicity, a Si-LN-Si waveguide with a LN core and a Si cladding of infinitely large thickness was considered. The influence of the PMP inner cladding on the THz wave was neglected due to its small absorption coefficient and small

thickness. THz waveguide effects of the Si-air outer boundary and waveguide dispersion for the pump were also neglected, justified by the practical limit of about 5 mm to the ARWG length, which is due to the small core thickness. A pump wavelength of 1030 nm was assumed, typical for Yb-doped lasers.

The thickness of the LN core determines the power confinement ratio and the PFT angle. The power confinement ratio is defined as $P_{\mathrm{core}}/P_{\mathrm{total}}$, i.e. the ratio of the THz power inside the LN core and the total THz power, calculated from the transversal intensity distribution of the lowest-order waveguide mode [169]. The PFT angle γ for pump-THz velocity matching can be determined by taking into account waveguide dispersion, which results in an effective refractive index $n_{\mathrm{eff,THz}}$ for the THz radiation [168, 169]. In this case the velocity matching condition reads as $c/n_{\mathrm{eff,THz}} = \left(c/n_{\mathrm{g,pump}}\right) \cdot \cos\gamma$. For an advantageously small power confinement ratio of less than ~25% a small core thickness is required (for details, see Ref. [168]). The corresponding PFT angle varies between 51° and 57° and is smaller than 63°, the value in bulk LN. This is advantageous for increasing the efficiency of the THz source, since a smaller PFT angle enables a larger effective interaction length for THz generation [41]. Besides a reduced absorption, this also contributes to an increased THz generation efficiency, as illustrated in Figure 42 for OR of 10-nJ, 100-fs pulses. Figure 42a shows the variation of the pump pulse duration and Figure 42b the build-up of the THz field, in terms of efficiency, along the propagation distance. The maximum efficiency is almost 20 times larger for the ARWG than for bulk LN.

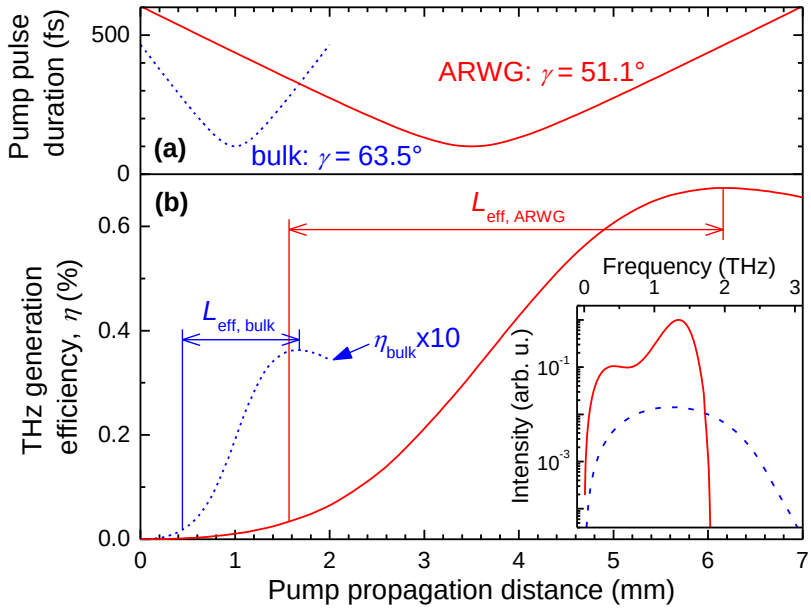

Figure 42. Pump pulse duration (a) and the (cumulative) THz generation efficiency (b) vs. pump propagation distance for bulk and ARWG. The inset shows the THz spectra corresponding to the efficiency peaks. From Ref. [168].

Table 1 summarizes possible ARWG design parameters for various typical laser parameters, together with the basic characteristics of the predicted THz output. To estimate the THz output, a similar model was used as in Ref. [126]. The variation of the

pump pulse duration during propagation owing to angular and material dispersion in LN was taken into account. A frequency-dependent effective refractive index was considered, and an effective absorption coefficient in the THz range was defined as $\alpha_{\mathrm{eff,Thz}} = \alpha_{\mathrm{THz}} \cdot P_{\mathrm{core}}/P_{\mathrm{total}}$, where α_{THz} is the absorption coefficient of bulk LN. The ARWG length was approximately set to the effective interaction length for THz generation, but was limited to ≤5 mm. In each case, the LN core thickness was chosen to fit with the THz frequency of the spectral peak that of the bulk source, in order to facilitate a fair comparison. The core width was set to a minimum such that the peak pump intensity remained below 100 GW/cm^2 or the average below ~40 kW/cm^2 (measured damage threshold at 300 kHz repetition rate [170]), whichever was smaller.

Table 1. Design parameters and predicted performance of the ARWG THz source for various laser types.

Pump	Energy (μJ)	0.01	0.1	1	5
	Repetition rate (MHz)	100	10	1	1
	Pulse duration (fs)	100	200	300	300
	Average power (W)	1	1	1	5
	Average intensity (kW/cm^2)	40	40	30	30
	Peak intensity (GW/cm^2)	4	20	100	100
ARWG	LN core thickness (μm)	5	9	15	15
	Minimum LN core width (mm)	1.8	1.0	0.8	4.1
	ARWG length (mm)	5	5	5	5
THz	THz spectral peak (THz)	1.35	0.92	0.71	0.71
	THz energy (nJ)	0.066	3.2	95	477
	THz average power (mW)	6.6	32	95	477
	Efficiency enhancement factor ($\eta_{\mathrm{ARWG}}/\eta_{\mathrm{bulk}}$)	22×	6.6×	2.5×	2.5×
	Spectral intensity enhancement factor	53×	18×	7.6×	7.6×

The calculations predicted an enhancement of the THz generation efficiency, $\eta_{\mathrm{ARWG}}/\eta_{\mathrm{bulk}}$, by more than a factor of 20 for 10 nJ pump pulse energy, as compared with bulk LN. At higher pump energies the enhancement factor is gradually reduced. It is about 2.5 for μJ-level energies. Clearly, this reduction is due to the limited ARWG length, since the assumed 300 fs pulse duration would allow effective interaction lengths significantly longer than 5 mm. We note that even in case of the largest predicted efficiencies (~10%), the simple model of OR used here can still be adequate, rather than a more complex one taking into account the influence of the THz field on the pump, as the THz field strength is significantly reduced by the penetration into the cladding.

A comparison of the peak THz spectral intensities of the ARWG and bulk cases reveals an enhancement of 53× for 10 nJ pump and 7.6× at the μJ-level (Table 1), much larger than the efficiency enhancement. The reason for this is the larger dispersion of the effective refractive index than that of the bulk refractive index of LN, which leads to a reduced THz spectral width for the ARWG, clearly visible in the inset of Figure 42.

In summary, an absorption-reduced planar waveguide structure driven by TPFP was proposed for increasing the efficiency of THz pulse generation by OR of femtosecond laser pulses. Most of the THz power is propagating in the cladding with low THz

absorption, thereby reducing losses. In case of LN core, it was shown that a smaller pulse front tilt angle is required for velocity matching than in bulk LN, thereby increasing the interaction length and hence the conversion efficiency. Practical considerations and expected performance were presented for the design of an ARWG THz source for a broad range of laser pulse energies and repetition rates. The ARWG structure will expectedly enable highly efficient THz pulse generation in highly nonlinear materials having large absorption coefficient by using moderate pump energy delivered, for example, by compact fibre laser sources. The predicted more than one order of magnitude increase in the conversion efficiency opens up the possibility to build highly efficient and compact THz sources with extremely high average output power. Such sources can find many applications in (nonlinear) THz spectroscopy, imaging, and security.

Application of an ARWG structure for pump pulse energies in the tens-to-hundreds of μJ range and still longer pulse durations up to the ps range becomes impractical, as it is also indicated by the decreasing enhancement factors in Table 1. However, recently very attractive high-power laser sources became available with sub-mJ pulse energies. For example, 800-fs, 330-μJ laser pulses were generated from a 100-W regenerative Yb:YAG thin-disk amplifier at 300 kHz repetition rate [170]. In order to enable the construction of a high-average-power THz source for such a system, we designed a TPFP THz source based on the more conventional grating-imaging-LN prism scheme, rather than on the ARWG concept. The main challenge was to provide a large interaction length enabled by the long pump pulse duration, despite the still moderate pulse energy, and at the same time to avoid optical damage caused by the extremely high average power. The concept proposed was to utilize an elongated pump spot in the plane of angular dispersion. This enables to increase the interaction length and an efficient cooling of the LN prism slab at the same time. A large demagnification of 1:10 was proposed for the imaging optics, rather than the commonly used ~1:2, in order to reduce the heat load and the corresponding damage risk at the grating. A pilot experiment delivered promising results [170], but the implementation of the elongated pump beam still needs to be realized. The realized setup was suitable for experiments for controlling ultrafast electron bunches.

7. Novel semiconductor THz sources

Different parts of the low- (~0.1 THz–2 THz) and mid-frequency (~2 THz–20 THz) bands of the THz range can be accessed by OR in various nonlinear optical materials. DFG, OPA, and THz radiation from gas plasma generated by two-color laser fields can cover the high-frequency (~20 THz–200 THz) part. At medium frequencies OR in organic materials can deliver extremely high field strengths and energies [78].

In the low-frequency THz range OR in LN, using TPFP for phase matching [48], has been providing the highest THz pulse energies [102] and field strengths [63, 64] with reported efficiencies beyond 1% [150]. The generation of THz pulses with more than 0.4 mJ energy was demonstrated with 0.77% efficiency [102]. Recently, limitations of this technology have been investigated [47, 124], showing that further increase of the THz energy and field strength is challenging. The main reason for the limitations is the large PFT angle (~63°) required for phase matching in LN.

Semiconductors, such as ZnTe and GaP are among the nonlinear materials most widely used for THz generation by OR. Collinear phase matching is possible for example in ZnTe, GaP, and GaAs in the vicinity of 0.8 μm, 1 μm, and 1.5 μm wavelengths, corresponding to commonly used Ti:sapphire, Yb-doped, and Er-doped lasers, respectively. Conventionally, semiconductors were considered as less efficient for THz generation than LN [44]. The highest THz energy previously reported from a semiconductor source was 1.5 μJ [68], achieved in ZnTe with 3×10^{-5} efficiency. The reason for the low pump-to-THz energy conversion efficiency was strong 2PA at the pump wavelength of 0.8 μm, and the associated FCA at THz frequencies.

In this Chapter theoretical and experimental studies will be presented which opened up the route for compact, efficient, and scalable THz sources based on semiconductor materials.

7.1. Prospects of efficient semiconductor THz sources

The work described in this Section reconsidered semiconductors for their suitability to high-field, high-energy THz pulse generation. We showed by numerical calculations that semiconductors can compete with LN in terms of efficiency, despite their smaller nonlinear coefficient, and can surpass LN in scalability to extremely high THz field strengths and pulse energies. The key point is to use pump wavelengths sufficiently long to suppress low-order MPA [171] and, consequently, detrimental FCA at THz frequencies. As a result, a higher pump intensity can be used and a higher THz generation efficiency can be expected. Such longer pump wavelengths typically require TPFP.

A scheme of MPA processes of various orders is shown in Figure 43a. Cut-off wavelengths for MPA of various orders are indicated by symbols in Figure 43b for a few different materials. The bandgap of ZnTe is 2.26 eV and that of GaP is 2.27 eV, the latter being an indirect one. These are sufficiently large to avoid both two- and three-photon absorption for pump wavelengths longer than 1.65 μm. GaSe is another suitable material. It has a slightly smaller bandgap of 2.02 eV, requiring a wavelength longer than about 1.85 μm. These wavelength ranges can be accessed by optical parametric amplifiers driven by Ti:sapphire or Yb lasers, available in many laboratories, or by Ho laser

technology operating near 2.05 µm [172, 173]. Other semiconductors, such as CdTe or GaAs [171], with a significantly smaller bandgap (both 1.43 eV) are less advantageous choices as an even longer pump wavelength would be needed to eliminate both 2PA and 3PA. For this reason, in most cases ZnTe and GaP are considered here.

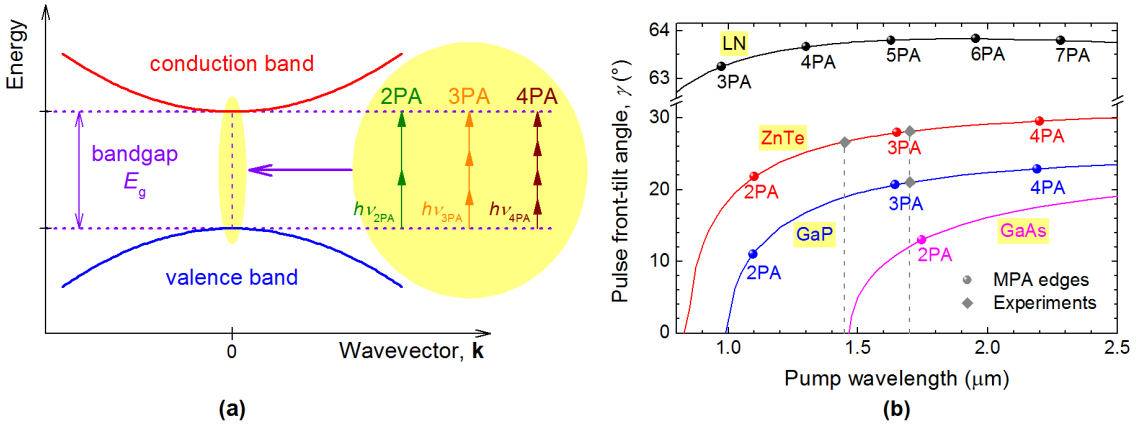

Figure 43. (a) Schematic band structure of a direct-bandgap semiconductor (e.g. ZnTe) indicating free-carrier generation by MPA of various orders (n) pumped at the respective cut-off wavelengths $\lambda_{n\mathrm{PA}} = c/\nu_{n\mathrm{PA}}$, where c is the vacuum speed of light. (b) PFT angle versus pump wavelength for phase matching at 1 THz in LN and selected semiconductors. The symbols indicate the cut-off wavelengths for MPA of various orders. In case of GaP, the indirect bandgap is considered. The dashed vertical lines and the diamond symbols indicate the wavelengths and materials used in the experiment described in Sections 7.2 and 7.3. From Ref. [51].

Simulations and experiments for THz generation in ZnTe and GaP were carried out at 1.45 µm and 1.7 µm pump wavelengths, below and above the 3PA cut-off (1.65 µm), respectively. Around 1.45 µm, where 3PA is still effective, a local minimum of the 3PA coefficient can be expected in ZnTe. Theoretical and experimental studies indicated that in zinc-blende type semiconductors such a minimum is at a 10% to 15% shorter wavelength than the 3PA cut-off [174, 175]. A similar behaviour is expected for GaP, where the indirect (direct) bandgap is 2.27 eV (2.48 eV).

For most of the simulations, the one-dimensional wave equation with the nonlinear polarization was solved in the spectral domain. This model, described in more detail in Section 5.1 and in Ref. [41], takes into account the variation of the pump pulse duration with propagation distance due to material and angular dispersions, the absorption in the THz range due to phonon resonances and FCA, latter caused by MPA of the pump. For the pump, the projected propagation distance onto the THz propagation direction was used in order to account for the noncollinear phase matching in a TPFP scheme. In some cases a more sophisticated model was used [71]. In addition to the effects mentioned above it also took into account nonlinear refraction (Kerr effect) for the pump, leading to SPM. Down- and up-conversion of the pump field by the THz field (cascading effects) were also included [47, 71, 124]. Material data used in the calculations are summarized in Ref. [71].

FCA in the THz range, caused by 3PA of the pump, was taken into account in case of 1.45 µm pump wavelength. In the simulations, the estimated value of $\beta_3 = 1.8 \times 10^{-2}$ cm^3/GW^2 was used for the 3PA coefficient of ZnTe. This value was obtained, in lack of known published data, from matching simulation results to our experimental data. For GaP, the published value of $\beta_3 = 4.2 \times 10^{-2}$ cm^3/GW^2 was used [44, 176]. In some

of the simulations for ZnTe pumped beyond the 3PA edge at 1.7 µm, the estimated 4PA coefficient of $\beta_4 = 3 \times 10^{-5}$ cm^5/GW^3 was taken into account, obtained also from fit to experimental data shown in Section 7.3. The effect of higher-order pump absorption was not taken into account, due to lack of available data for the respective MPA coefficients.

Results of simulations clearly indicate that for obtaining high conversion efficiencies it is not sufficient to avoid only 2PA. Even 3PA can pose a serious limitation on the useful pump intensity, as shown in Figure 44a by dashed curves for ZnTe and GaP in case of pump at 1.45 µm. Strong saturation of the THz generation efficiency is observed already at a low pump intensity of about 6 GW/cm^2 and 3 GW/cm^2 for ZnTe and GaP, respectively. The predicted efficiency is limited to about 2×10^{-3} and 1×10^{-3}, respectively. In contrast, for 1.7 µm pump and omitting 4PA, the THz generation efficiency increases linearly up to significantly higher intensities (solid lines in Figure 44a). Taking into account 4PA in ZnTe results in saturation of the THz generation efficiency even for 1.7 µm pump wavelength (short-dashed line in Figure 44a). Importantly, the predicted maximum efficiency of 0.6% is about 3.4 times higher than in case of pump at 1.45 µm. About 16 GW/cm^2 pump intensity can be used in case of 1.7 µm pump. Similar behaviour can be expected for GaP.

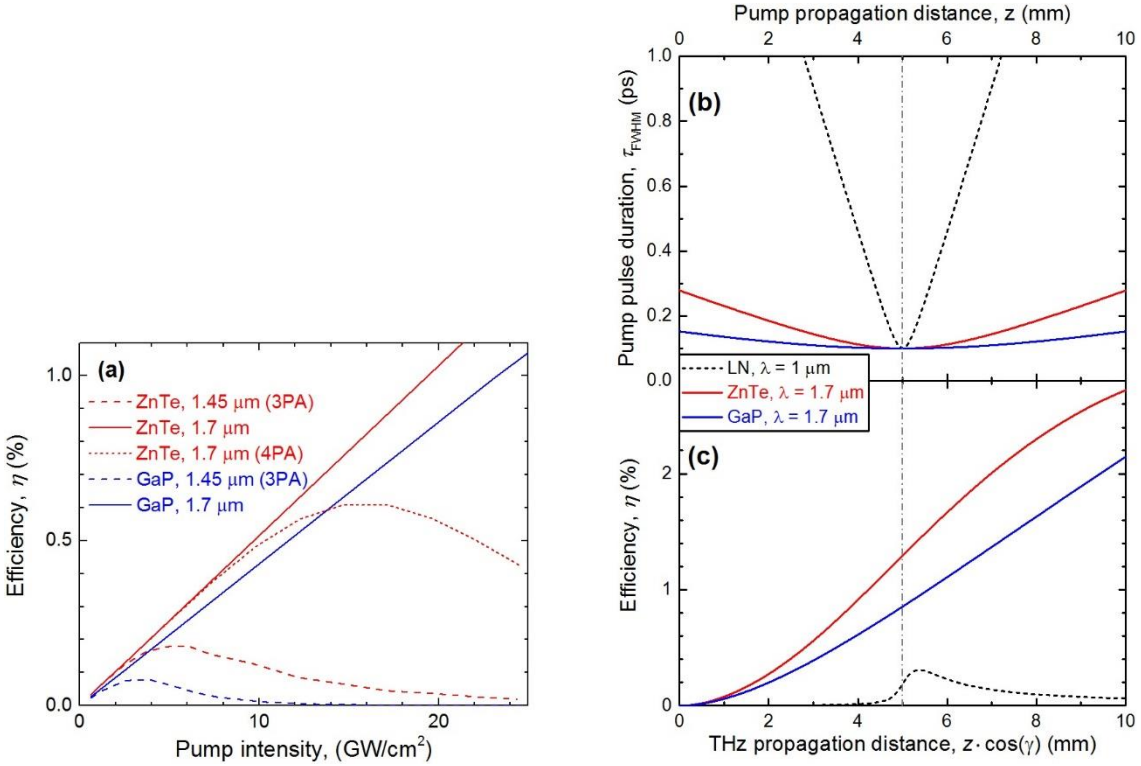

Figure 44. (a) Calculated THz generation efficiencies as function of pump intensity for ZnTe (red lines) and GaP (blue lines) for pump wavelengths set below (dashed lines) and above (solid and short-dashed lines) the 3PA cut-off. The order of MPA process taken into account is indicated in the legend. 100 fs pump pulse duration and a crystal length of 2.9 mm was assumed. The phase matching frequency and the THz spectral peak were matched in each case. (b) Pump pulse duration as function of the pump propagation distance z for LN, ZnTe, and GaP crystals. For LN a pump wavelength of 1 µm, for ZnTe and GaP 1.7 µm were chosen. The position of FL pulse duration was arbitrarily set by prechirp to 5 mm in all cases (indicated by the vertical dashed-dotted line). (c) THz generation efficiency as a function of THz propagation distance. Parameters used in the simulations: 100 fs FL pump pulse duration with a pre-chirp at $z = 0$, pump intensity of 9 GW/cm^2, and phase matching at 1 THz. From Ref. [51].

The dependence of the phase-matching PFT angle on the pump wavelength is shown in Figure 43b for the selected semiconductors and LN. The tilt angle can be calculated from optical and THz refractive index data (see [51] for details). For example, the optical group index at 1.7 μm is 2.78 and the refractive index at 1 THz is 3.16, giving 28.1° for the PFT angle. In general, the PFT angle for semiconductors is about 30° or smaller, while for LN it is about 63°. A smaller tilt angle is advantageous for several reasons. *Firstly*, it causes a smaller variation of the pump pulse duration within the nonlinear medium (Figure 44b) and enables a larger effective length for THz generation (Figure 44c). This can help to compensate for the smaller nonlinear coefficient of semiconductors. *Secondly*, a smaller tilt angle significantly reduces the spatial nonuniformity of the interaction length for THz generation, and consequently that of the THz beam. Such a spatial inhomogeneity is a serious drawback in case of LN [47, 124]. The potentially much better spatial homogeneity in case of semiconductor sources enables an easier increase of the pumped area and the THz energy. *Furthermore*, the small tilt angle is also advantageous for the realization of a contact-grating (CG) THz source [132, 143, 177]. We demonstrated such a CG source in ZnTe (see Section 7.2) [50]. Importantly, the CG technology enables to practically eliminate spatial nonuniformity of the interaction length, which leads to a straightforward scalability of the THz energy and excellent THz beam profile and focusability [50]. CG fabrication technology enables grating sizes on the 5-cm scale. Based on these advantages, it was anticipated that THz pulses with >1 mJ energy and >20 MV/cm electric field strength will be achievable with less than 200 mJ pump energy from a (possibly segmented) CG source [50]. Such pump pulses in the wavelength range of 1.7 μm to 2.5 μm, though not available presently, are definitely feasible in the near future from optical parametric amplifiers or infrared laser technology [172, 173].

We demonstrated in a proof-of-principle experiment the benefit of long-wavelength pumping [51]. A comparative study of THz pulse generation in ZnTe, pumped below (1.45 μm) and above (1.7 μm) the cut-off wavelength for 3PA was carried out using a conventional (grating, imaging, crystal prism) TPFP setup with a ZnTe prism. The comparison also included GaP pumped at 1.7 μm, above the 3PA cut-off. A commercial OPA was used, which was driven by a Ti:sapphire laser system. The pulse length of the OPA output was about 100 fs. Up to 240 μJ and 360 μJ pump energy reached the THz generation crystal at 1.45 μm and 1.7 μm pump wavelengths, respectively. More details of the experiment can be found in Ref. [51].

The measured THz energy and THz generation efficiency as functions of pump energy and intensity, respectively, are shown in Figure 45. In case of ZnTe and 1.45-μm pump a maximum efficiency of about 4×10^{-4} is reached at 6 GW/cm^2 pump intensity, which indicates the onset of 3PA. At higher intensities the efficiency was observed to decrease slowly. At about 14 GW/cm^2 pump intensity the efficiency starts to increase again, which can possibly be caused by the saturation of 3PA. We note that a similar behaviour, owing to the saturation of 2PA, was observed in ZnTe at 0.8 μm pump wavelength [147]. At 1.7 μm, where only 4PA and higher-order absorption were effective, the efficiency was increasing up to a maximum of about 1.4×10^{-3} at 13.5 GW/cm^2 intensity, followed by a decrease. This efficiency is up to 3.5 times higher than in case of 1.45 μm pump wavelength, owing to the elimination of 3PA. A saturation of the efficiency at the level of about 6×10^{-4} was observed for GaP pumped at 1.7 μm.

This is slightly lower than that of ZnTe, and can be explained by the smaller nonlinear coefficient of GaP and possibly by a larger 4PA coefficient. The observed onset of 4PA at 13.5 GW/cm^2 pump intensity in ZnTe, as compared to the onset of 3PA at about 6 GW/cm^2, indicates that avoiding 3PA enables to efficiently use more than two times higher pump intensity. This larger pump intensity was essential for achieving the unprecedented high efficiencies up to 0.7% in ZnTe, presented in Sections 7.2 and 7.3.

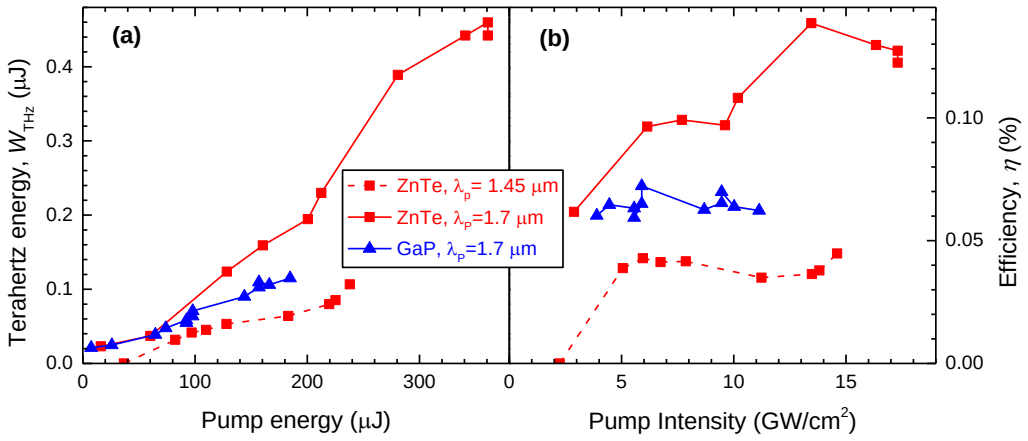

Figure 45. THz energy as function of pump energy (a) and THz generation efficiency as function of pump intensity (b) for ZnTe pumped at 1.45 μm and 1.7 μm wavelengths, and for GaP pumped at 1.7 μm. The pump pulse duration from the tuneable OPA was about 100 fs. From Ref. [51].

A comparison of simulated and measured efficiencies for ZnTe (Figure 44a and Figure 45b) shows that our simple model was able to predict the intensities corresponding to the efficiency maxima both for 1.45 μm and 1.7 μm pump wavelengths. (The measured peak efficiencies are smaller by about a factor of four than the calculated ones, which may be partially explained by the limited interaction length due to a small pump spot size. A better agreement with the experiment was found for larger spot sizes, as discussed in Section 7.3). A comparison of our experimental data for 1.45-μm pump (with 3PA as the lowest-order effective MPA) to data for 0.8 μm (where 2PA is also effective) [68] shows that eliminating 2PA enabled the increase of the THz generation efficiency by more than one order of magnitude. An additional 3.5-fold increase could be achieved with eliminating also 3PA (Figure 45b).

These theoretical and experimental results clearly indicated to potential of infrared-pumped semiconductor sources for the efficient generation of intense THz pulses. Our further numerical studies were aiming at exploring in more detail optimal material parameters, pumping and phase-matching conditions, as well as the expected output characteristics for such sources [41, 71].

In our first numerical study the THz generation performance of various semiconductors was compared to LN [41]. The results showed that for phase matching at 1 THz and pump intensities up to about 20 GW/cm^2 semiconductors such as ZnTe, GaP, GaSe, and GaAs can compete with LN, or even surpass it in terms of THz generation efficiency when pumped at a wavelength sufficiently long to suppress 2PA (but still below the 3PA cut-off). However, in LN only 4PA is effective at the frequently used

pump wavelength of 1 μm and it can be pumped at still higher intensities, giving higher THz generation efficiencies, whereas 3PA in semiconductors results in saturation of THz generation. The saturation of THz generation in LN was observed above 85 GW/cm^2 pump intensity and was attributed to FCA due to 4PA of the pump [44]. In contrast, at the higher phase-matching frequencies (3 THz and 5 THz) semiconductors, such as GaAs or GaP, are competitive even when LN is pumped at much higher intensities up to about 85 GW/cm^2. They can provide higher efficiency than LN even at a much weaker pump intensity level. The reason is that LN has a higher THz absorption in this spectral range, and that a significantly larger interaction length can be utilized for semiconductors. Furthermore, the calculated spectra showed that LN might still be a better choice, when THz pulses with a relatively large bandwidth need to be efficiently produced, despite the eventually higher efficiency of some semiconductors. Semiconductors can be advantageous for efficiently generating THz pulses with higher spectral intensity at higher frequencies.

In another numerical study our aim was to give practical guidelines for the selection of the nonlinear material, the pump wavelength, pulse duration, and intensity, as well as crystal thickness and THz phase matching frequency [71]. ZnTe and especially GaP pumped at a wavelength longer than the 3PA cut-off were shown to be most promising for realizing efficient contact-grating THz sources (see also Section 7.2).

GaP has a significantly smaller absorption and dispersion in the THz range than ZnTe. It can also be manufactured in larger sizes and better quality. Its smaller nonlinear coefficient, as compared to that of ZnTe, may be partially compensated by the larger effective interaction length for OR, enabled by the smaller PFT angle and dispersion. Owing to its higher phonon frequency and small linear absorption coefficient, it can be especially suitable for generating higher frequencies in the range of 2 THz–5 THz or even beyond. The all-over field and efficiency maxima are both predicted at about 20 GW/cm^2 with 150 fs and 100 fs pulse durations, respectively (Figure 46a, d). With increasing intensity FCA due to 4PA shifts the THz spectrum to higher frequencies (Figure 46e). The achievable peak electric field, efficiency, and spectrum are also strongly influenced by the interaction length (Figure 46c, f). Our simulation results clearly showed the importance of the proper choice of the phase-matching frequency and the crystal length (interaction length), but also demonstrated the versatility of GaP as a THz source. It can be suitable to be used as a broadband source with high field strength, but also as a narrowband source with high spectral intensity. In the latter case, broadband tenability can also be provided by changing the PFT angle, possibly even up to as high as 7 THz [72, 178]. The corresponding many-cycle waveform can be of advantage also in interesting new applications like charged-particle acceleration.

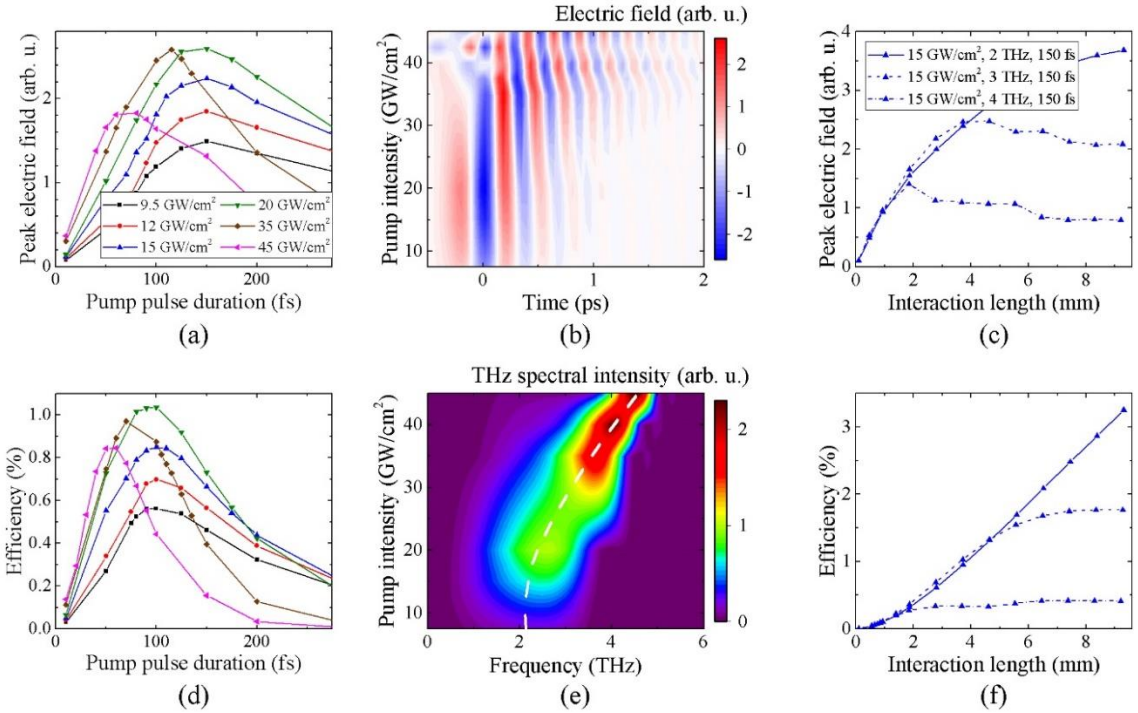

Figure 46. Simulation results for GaP with 2.7 mm interaction length, pumped at 1.7 μm wavelength. Peak electric field (a) and THz generation efficiency (d) as functions of the FL pump pulse duration for different values of the pump intensity. Time dependence of the electric field (b) and spectral intensity (e) of the THz pulses for different pump intensities. The white dashed curve in panel (e) indicates the phase-matching frequency. The THz peak electric field (c) and the efficiency (f) as functions of the interaction length at the indicated pump intensities, pump pulse durations, and phase-matching THz frequencies. Legends for panels (d) and (f) are shown in (a) and (c), respectively. From Ref. [71].

7.2. A monolithic semiconductor THz source

Here, a highly efficient, monolithic, and alignment-free semiconductor THz source is demonstrated [50]. The source is pumped at an infrared wavelength beyond the 3PA cut-off. Such long-wavelength pumping enables the suppression of 2PA and 3PA, together with the associated FCA of THz radiation. The important consequence is that a higher pump intensity can be used and a higher THz generation efficiency can be achieved, as discussed in Section 7.1. At infrared wavelengths, semiconductors typically require tilting the pump pulse front for phase matching. In the work described here it was shown that a highly efficient semiconductor THz source can be constructed by using a contact grating (CG) for tilting the pump pulse front [132, 177, 179]. This allows to eliminate the distortions caused by imaging optics in conventional pulse-front-tilting setups [41]. The small tilt angle, typically in the range of 20° to 30°, makes semiconductor materials ideally suited for the realization of a CG THz source.

The principle of operation of the semiconductor CG source is illustrated in Figure 47a. A grating structure, responsible for tilting the pump pulse front, is formed on the entrance surface of the nonlinear material. In the setup shown here, the pump beam is perpendicularly incident on the CG and two symmetrically propagating diffraction orders $m = \pm 1$ are created [132, 143]. The generated THz beam propagates collinearly with the incident pump beam and leaves the crystal through the back surface.

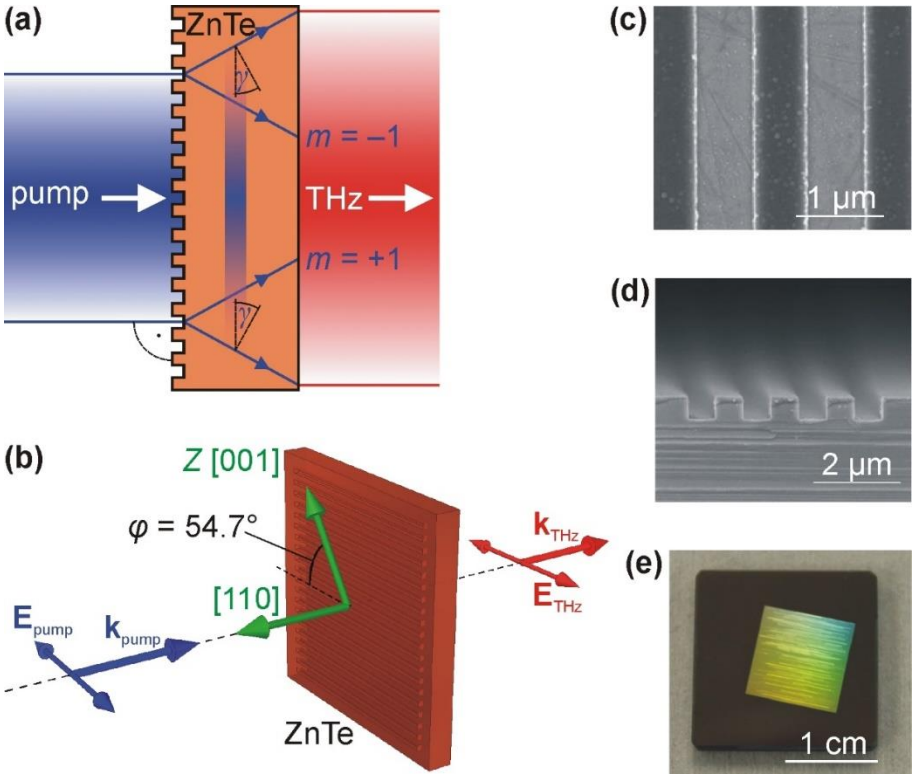

Figure 47. (a) Scheme of the CG THz source with collinear geometry, utilizing the two diffraction orders $m = \pm 1$. The pulse-front tilt angle is γ. (b) Geometry of the CG THz source. E_{pump} and E_{THz}: pump and THz polarization directions, k_{pump} and k_{THz}: pump and THz propagation directions. Crystallographic directions are given in rectangular brackets. φ: angle between grating lines and the crystallographic Z-axis. (c) Top-down scanning electron microscope (SEM) image of the grating surface. (d) SEM micrograph of a cleaved test sample showing the grating profile. (e) Photograph of the CG THz source. From Ref. [50].

ZnTe was chosen as the nonlinear material because of its relatively large nonlinear coefficient ($d_{\text{eff}} = 68.5$ pm/V), but the technique can easily be adopted to other semiconductors. The pump wavelength was 1.7 μm, which is above the 3PA cut-off in ZnTe. The pump PFT angle was set by the grating period of 1275 nm to $\gamma \approx 28°$ for phase matching at 1 THz. The pump and THz polarization and propagation directions, as well as the orientations of the 2 mm thick ZnTe substrate and the grating lines are shown in Figure 47b. The manufactured grating profile (Figure 47c, d) was closely fitting the binary design profile, optimized for highest diffraction efficiency [143]. For 50% filling factor, 400 nm profile depth, and TE polarization about 78% diffraction efficiency was predicted in total for the two orders $m = \pm 1$.

The CG with an area of 10×10 mm^2 (Figure 47e) was fabricated at Scitech Precision Ltd. using a combination of electron beam microlithography and dry (plasma) etching. Initially, the polished ZnTe substrate was coated with an etch-resistant metallic film, followed by a layer of electron beam resist. The resist was patterned by electron beam lithography. The pattern was transferred into the metal layer and subsequently into ZnTe in two different dry etching steps. Finally, the residual metal was stripped, and the substrate cleaned and inspected before use. We note that bubbles in the substrate uncovered as pits in the surface resulted in disruption of the resist film and caused defects of the grating profile (seen as light lines parallel to the invisible grating lines in Figure 47e). Such defects were effecting about 20% of the total grating area. A final grating in ZnTe at the correct dimensions could be created by taking into account the individual

offsets and biases of the lithography and pattern transfer processes, and a careful optimization of the electron beam exposure was necessary during test runs. Nearly perpendicular wall angles could be achieved (Figure 47d), which was important for a high diffraction efficiency.

The THz energy was measured by a calibrated pyroelectric detector (Gentec QS9-THZ-BL). A Teflon plate blocked the infrared pump and transmitted only the THz radiation to the detector. The voltage signal of the detector was fed to a storage oscilloscope and the THz energy W_{THz} was calculated from the voltage modulation V_{m} of the recorded trace according to $W_{\mathrm{THz}} = CV_{\mathrm{m}}\tau/S$, where the sensitivity $S = 1.2$ kV/W was obtained from factory calibration, while the correction factor $C \approx 1$ and the time constant $\tau = 5.1$ ms were determined from fitting of the recorded trace.

Up to 3.9 μJ THz pulse energy was observed from the CG source (Figure 48a, black circles), generated with 0.17% efficiency (Figure 48a, red squares) by using pump pulses of 144 fs duration delivered by an OPA available at the Photonics Institute of the Technical University of Vienna. For comparison, the previously reported highest THz pulse energy from a semiconductor source was 1.5 μJ [68]. As high as 0.3% maximum conversion efficiency was achieved (Figure 48a), corresponding to 2.3 μJ THz pulse energy. This efficiency was 6 times higher than the highest value reported previously from any semiconductor source [49], and 97 times higher than the highest previously reported value for a ZnTe source [68]. The former was achieved with GaAs, pumped above the 2PA, but below the 3PA cut-off wavelength, and the latter was achieved with ZnTe pumped collinearly at 0.8 μm, suffering from strong 2PA. We note that in a LN CG source, partly because of technical reasons, only a very small THz generation efficiency (1.5×10^{-4}) was demonstrated previously [179]. The potential of the semiconductor CG THz source is clearly demonstrated here by the significant increase both in energy and efficiency.

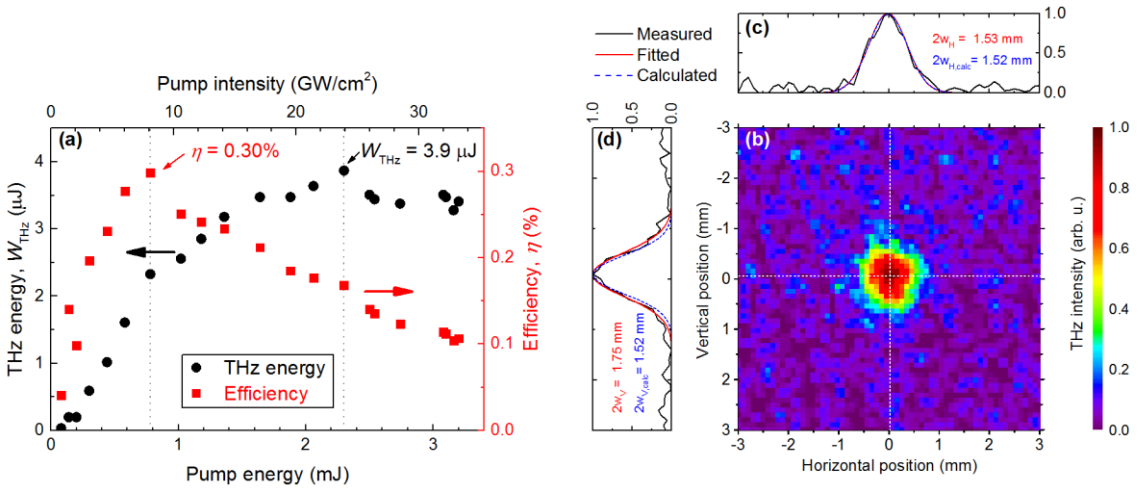

Figure 48. (a) Measured THz energy (black circles) and THz generation efficiency (red squares) versus pump energy and intensity. (b) Pyroelectric camera image of the THz beam in the focus of a 10-cm focal length Teflon lens, placed at a 50-cm distance behind the CG source. The pump energy was 1.2 mJ. Black solid lines in (c) and (d) show the horizontal and vertical cross sections of the THz beam profile along the white dashed lines in (b), respectively. Red solid lines: Gaussian fit. Blue dashed lines: estimated diffraction-limited profiles. w_{H}, w_{V}, $w_{\mathrm{H,calc}}$, $w_{\mathrm{V,calc}}$: horizontal and vertical fitted and calculated beam radii at $1/e^2$ of the peak intensity, respectively. From Ref. [50].

One important consequence of the collinear setup geometry is the very good focusability of the THz beam. This is illustrated by the pyroelectric camera image of the THz focal spot (Figure 48b, c, d), where the relative deviation of the spot size from the estimated diffraction limit was only about 15%. For estimating the diffraction-limit, Gaussian beam propagation was assumed with an initial THz spot size at the CG equal to that of the pump. The estimation of the initial THz spot size corresponds to a linear, rather than quadratic, dependence of the THz energy on pump energy, justified by the observed saturation of the THz generation (Figure 48a).

EOS using a (110)-cut ZnTe crystal of 0.1 mm thickness, contacted to a 2 mm thick inactive substrate, revealed a nearly single-cycle THz waveform (Figure 49a). A small fraction of the 200-fs pulses, driving the OPA at 1.03 μm wavelength, were used as sampling pulses. The peak electric field was about 0.57 MV/cm, as estimated from the measured 3.9 μJ pulse energy, 2.1 mm^2 focal spot size, and the waveform. Fourier transform spectroscopy was used to measure the THz spectrum, in order to avoid distortions due to the relatively long sampling pulses. For this purpose, the field autocorrelation (Figure 49b) was recorded with a Michelson interferometer, containing a silicon beam splitter and the pyroelectric energy meter as detector. The THz spectrum was obtained by Fourier transformation of the interferogram. The maximum of the spectral intensity was at 0.9 THz and the spectrum extended up to about 2.3 THz (Figure 49c).

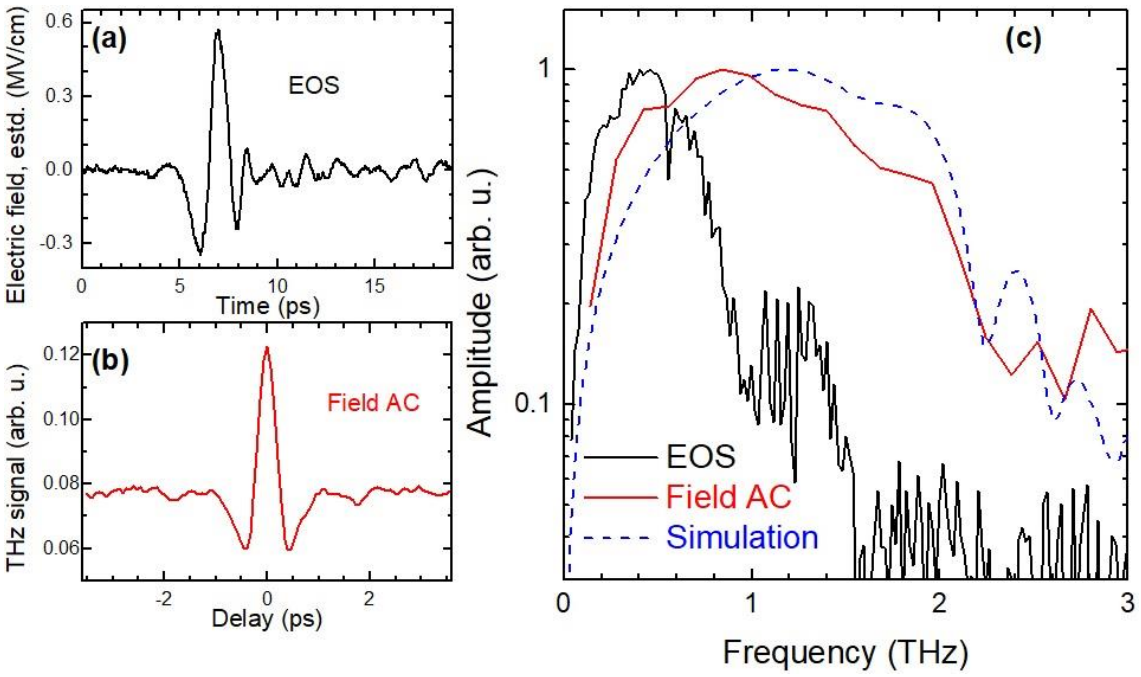

Figure 49. (a) Temporal waveform of the THz pulses, measured by EOS at 2.4 mJ pump energy. (b) Field autocorrelation (AC) of the THz pulses measured by a Michelson interferometer at 1.8 mJ pump energy. (c) Spectral amplitude of the THz pulses obtained by Fourier transformation from EOS (black solid line), field autocorrelation (red solid line), and simulation (blue dashed line). From Ref. [50].

The scalability of the CG THz source to higher energies and field strengths is important for applications. In this experiment, about 20% of the grating surface was ineffective due to defects in the substrate (seen as light lines in Figure 47e). A better substrate quality can eliminate such efficiency-reducing defects. Most importantly,

scaling to higher energies is possible simply by increasing the pumped area and the pump energy. A segmented source, similarly to organic crystals [79], could be used to circumvent possible limitations of substrate size and grating manufacturing technology. Another possibility is to increase the efficiency by increasing the material thickness. Calculations predict 2.3× (3.7×) higher efficiency by doubling (tripling) the substrate length. The expectation of an increased efficiency was supported by our measurements using a conventional (external) pulse-front-tilting setup to pump a prism-shaped ZnTe crystal of 1.5× larger average (centre) thickness than that of the CG (see Section 7.3). As high as 0.7% maximum conversion efficiency and 6.6 μJ THz energy were measured at 15 GW/cm^2 pump intensity [51]. Furthermore, cooling the crystal reduces the THz absorption and can enhance the spectral amplitude especially above 1 THz, where ZnTe absorbs stronger. Crystals with smaller absorption and dispersion, such as GaP, can be more advantageous for generating high field strengths (see Section 7.3).

In summary, a compact, monolithic, and alignment-free THz source was demonstrated (Figure 50). It utilizes a semiconductor nonlinear material, pumped beyond the 3PA cut-off, and a CG for tilting the pump pulse front. The collinear setup geometry is of great advantage for user experiments and ensures an excellent focusability of the THz beam. The efficiency demonstrated with the ZnTe CG source was as much as 6 times higher than the highest previously reported value from any semiconductor THz source, and the enormous two orders of magnitude higher than previously reported from a ZnTe source. The observed high efficiencies, similar to values reported for lithium niobate at high pulse energies [102], clearly demonstrate the potential of semiconductors as future high-energy THz pulse sources and support the expectation that THz pulses with 1 mJ energy can be generated with less than 200 mJ pump energy from a (possibly segmented) CG source of about 5 cm diameter. This new type of THz source, in combination with novel efficient infrared pump sources in the 1.7 to 2.5 μm wavelength range based, for example, on Holmium laser technology [172], opened up new perspectives for THz high-field applications. These range from strong-field control of matter to compact sources of particle and X-ray beams, key technologies for medicine and materials science.

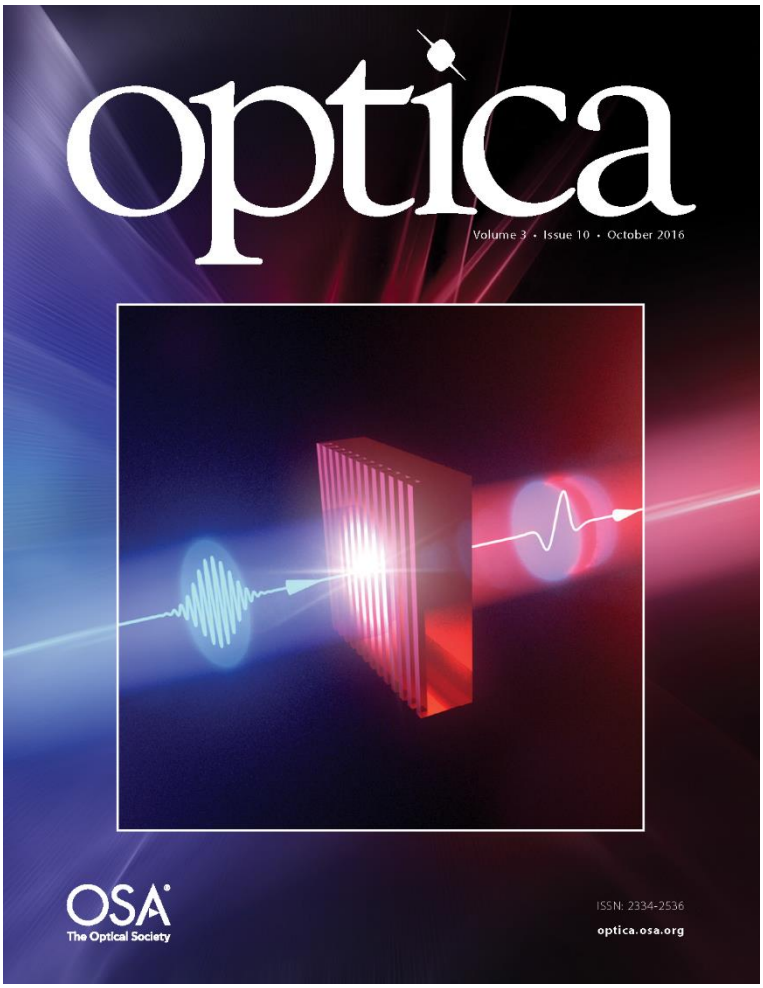

Figure 50. Artistic view of the ZnTe CG THz source on the cover of the October 2016 issue of Optica.

7.3. Scaling potential

The demonstration of a highly efficient ZnTe CG with 0.3% THz generation efficiency opened new perspectives for extremely intense THz sources [50]. It was predicted by our calculations that the THz generation efficiency can be increased further by increasing the crystal length [50, 51, 71] (see Figure 46f). In the work presented here, we experimentally demonstrated a further significant increase of the THz generation efficiency from a ZnTe source pumped at a wavelength longer than the 3PA cut-off [51]. Furthermore, we gave an estimation for the 4PA coefficient of ZnTe, which is important for the design of optimized semiconductor THz sources and for the estimation of their limits [51, 71].

The experimental setup is shown in Figure 51. For the generation of high-energy THz pulses in ZnTe, pump pulses were generated in a home-built supercontinuum-seeded four-stage OPA system, delivering 144-fs, 2.7-mJ pulses centred at 1.7 μm wavelength, available at the Photonics Institute of the Technical University of Vienna. This high-energy OPA was driven at 1.03 μm wavelength by a cryogenically cooled Yb:CaF_2 CPA laser system, built for our laboratory in Pécs, and consisting of an oscillator, a stretcher, a regenerative amplifier, a multipass power amplifier, and a compressor [180]. The system delivered 200-fs pulses with 90 mJ pulse energy at 50 Hz repetition rate. The pump spot size on the ZnTe prism was about 4.4×3.2 mm^2 (horizontal × vertical) at $1/e^2$

level. THz pulses were generated in (110)-oriented ZnTe and GaP prisms at room temperature, using conventional TPFP setups, consisting of a grating and a lens and optimized for minimum imaging distortions [41]. For ZnTe a 600 lines/mm, for GaP a 450 lines/mm grating was used. (The GaP prism was used for the measurement presented in Figure 45 in Section 7.1.) A half-wave plate rotated the horizontal polarization of the pump light, diffracted off the grating, to vertical, parallel to the $[1\bar{1}1]$ axis of the crystals. The focal length of the fused silica lens was 200 mm.

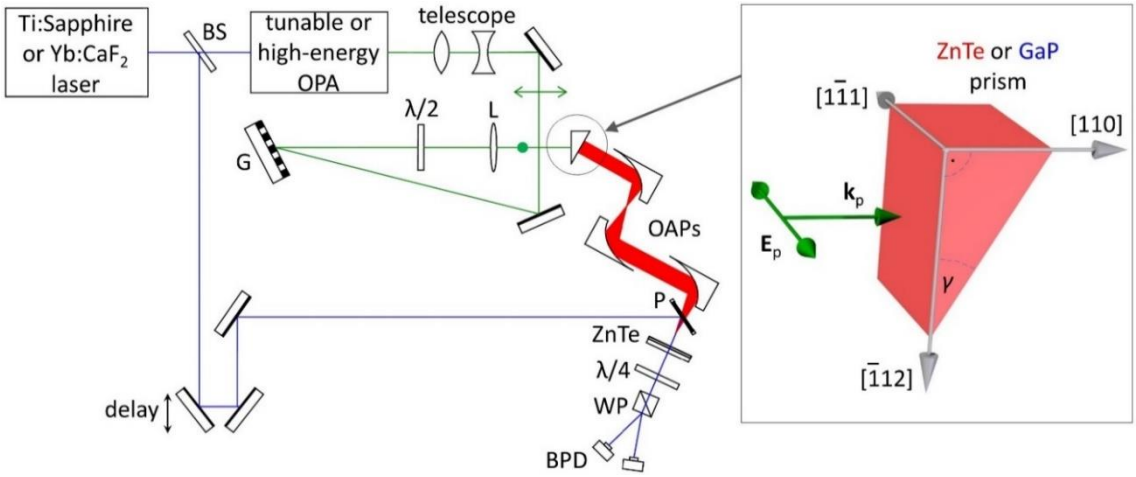

Figure 51. Experimental setup. BS: beam splitter, G: grating, λ/2: half-wave plate, L: lens, OAPs: off-axis parabolic mirrors, P: pellicle beam splitter, ZnTe: sandwiched ZnTe crystal for electro-optic sampling, λ/4: quarter-wave plate, WP: Wollaston prism, BPD: balanced photodiodes. The inset shows the orientation of crystal axes in the semiconductor prisms. From Ref. [51].

The THz pulse energy was measured by a calibrated pyroelectric detector (Gentec, QS9-THZ-BL). A Teflon plate blocked the infrared pump and transmitted only the THz radiation to the detector. The voltage signal of the detector was fed to a storage oscilloscope and the THz energy W_{THz} was calculated from the voltage modulation V_{m} of the recorded trace according to $W_{\mathrm{THz}} = CV_{\mathrm{m}}\tau/S$, where the sensitivity $S = 1.2$ kV/W was obtained from factory calibration, while the correction factor $C \approx 1$ and the time constant $\tau = 5.1$ ms were determined from fitting of the recorded trace. The THz waveform was measured by EOS. A small fraction of the 200-fs, 1.03-μm pump pulses was used for sampling in a 0.1 mm thick, (110)-cut ZnTe crystal, contacted to a 2 mm thick inactive substrate of the same material. As the sampling pulses were relatively long, which distorted the measured spectrum, Fourier transform spectroscopy was also used. For this purpose, the field autocorrelation was measured with a Michelson interferometer, containing a 4 mm thick silicon beam splitter and a pyroelectric energy meter as detector. The THz spectrum was obtained by Fourier transformation of the interferogram.

The high-energy OPA as pump source enabled a significantly higher pump energy at 1.7 μm wavelength than in our previous experiment shown in Section 7.1 (Figure 45). The measured THz energy and THz generation efficiency as functions of pump energy and intensity are shown in Figure 52. The larger pump energy enabled a larger pump spot and resulted in significantly increased THz energy and efficiency. THz pulses with up to 14 μJ energy were observed, generated with 0.5% efficiency. For comparison, the previously reported highest THz pulse energy from a semiconductor source was 1.5 μJ [68]. As high as 0.7% maximum conversion efficiency was achieved at about 15 GW/cm^2

pump intensity, corresponding to 6.6 µJ THz energy. The achieved maximum efficiency is 14 times higher than the highest value reported previously from any semiconductor source [49], and the enormous 220 times higher than the highest previously reported value for a ZnTe source [68]. In Ref. [49], GaAs was pumped above the 2PA, but below the 3PA cut-offs, whereas in Ref. [68], ZnTe was collinearly pumped at 0.8 µm, which caused strong 2PA. Our control measurement at 0.8 µm pump wavelength using a 2 mm thick (110)-cut ZnTe plate, pumped by 100-fs pulses at 15 GW/cm^2 intensity, resulted in only 5×10^{-6} efficiency. This is about five times lower than that in [68] at the same pump intensity. The difference between efficiencies could be caused by the different pump pulse durations (30 fs in [68]) and the difference in detector calibrations.

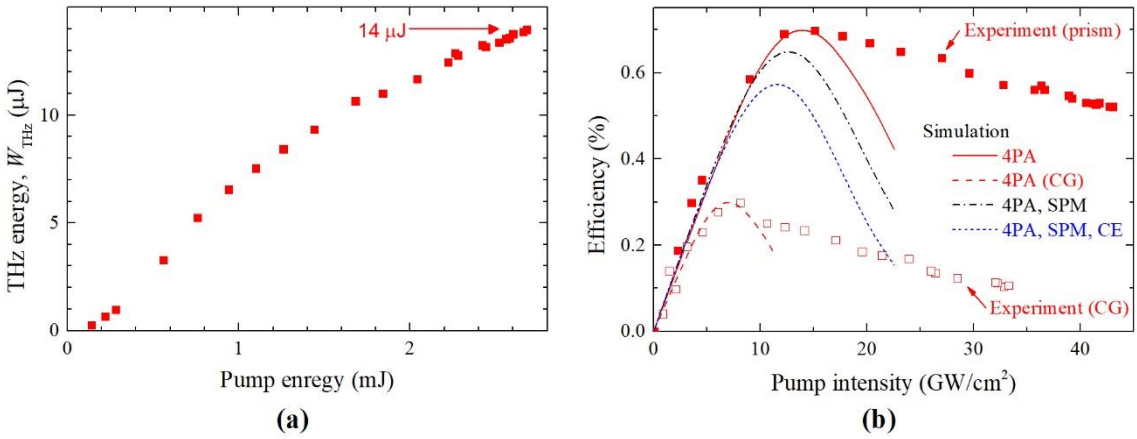

Figure 52. Measured THz energy as function of pump energy (a) and THz generation efficiency as function of pump intensity (b) for ZnTe pumped at 1.7 µm. Full square symbols: measured data with a TPFP setup consisting of a grating, a lens, and a ZnTe prism [51]; empty square symbols: measured data with a ZnTe CG source [50]. The curves show simulation results including the effect of 4PA (red solid line), including SPM but excluding cascading effects (black dashed-dotted line), and including both SPM and cascading effects (blue short-dashed line). The red dashed line shows the simulation results for the CG including 4PA only.

The observed saturation of the THz generation efficiency in ZnTe can be attributed to FCA due to 4PA of the pump at 1.7 µm. Both measurement series at 1.7 µm pump, presented in Figure 45 and Figure 52, are consistent with an estimated value of the 4PA coefficient of $\beta_4 = (3 \pm 1) \times 10^{-5}$ cm^5/GW^3. This value was obtained by fitting simulation results to the experimental data of Figure 52 in terms of the pump intensity at which the efficiency maximum occurs. The saturation of the efficiency, caused by 4PA, with a maximum at about 15 GW/cm^2 was observed and well reproduced by the simulation (Figure 52b). At increasingly higher pump intensities the simulation predicts a more rapidly decreasing efficiency than the observed one. (Because of this deviation between simulation and experiment, measured data corresponding to >15 GW/cm^2 pump intensity were discarded from fitting the value of β_4.) For comparison, a relatively small value of $\beta_4 = 10^{-7}$ cm^5/GW^3 was estimated for LN when pumped at 1.03 µm [44]. Therefore, our value for ZnTe is consistent with the general trend of increasing nonlinearity with decreasing bandgap energy [181].

As a possible reason for the deviation between experiment and simulation at higher pump intensities we considered nonlinear refraction (Kerr effect). The nonlinear refractive index of ZnTe is $n_2 = 1.2 \times 10^{-4}$ cm^2/GW [182], which is more than two orders of magnitude larger than that of LN with a significantly larger bandgap [181]. The

comparison of a calculation using a model with 4PA only (red solid line in Figure 52b) and a model with 4PA and pump SPM due to nonlinear refraction (black dashed-dotted line in Figure 52b) reveals a small effect of SPM with a slightly reduced efficiency maximum. Including also cascading effects (blue short-dashed line in Figure 52b) further reduces the efficiency maximum. However, in both models with SPM, a similarly rapid drop in efficiency is predicted at high pump intensities than with the simpler, 4PA-only model, in contrast to the measured slower drop. Varying the value of β_4 in the simulation did not lead to any improvement in this respect. Therefore, we conclude that to predict the location of the maximum THz generation efficiency it is sufficient to consider 4PA only.

The saturation of 2PA-induced FCA was observed in ZnTe at high pump fluences [147]. Similarly, saturation of 4PA-induced FCA may also influence THz generation at higher pump intensities and can be the reason for the observed deviation between experiment and theory. This requires further investigation including the study of ultrafast carrier dynamics, which was beyond the scope of our work. The pump intensity range most interesting for applications is that up to the maximum of THz generation efficiency. In this range, the simple model of FCA [41, 44, 71] used here gave a reasonably good agreement with experimental efficiency data (Figure 52b).

We note that the same value of β_4 can be used to fit (Figure 52b, red dashed line) the results of another measurement (Figure 52b, empty square symbols), carried out with a ZnTe CG source [50], described in Section 7.2. The observed dependence of the THz generation efficiency is very similar to the previous case [51]. However, the maximum efficiency is located at about half of the pump intensity for the efficiency maximum in the previous case, i.e. at about 8 GW/cm^2 rather than about 15 GW/cm^2. The reason is the interference of the two diffraction orders ± 1 from the CG, which doubles the maximum pump intensity. The smaller efficiency is mainly caused by the smaller crystal length for the CG.

EOS revealed a nearly single-cycle THz waveform (Figure 53a). In order to avoid distortions due to the relatively long sampling pulses, Fourier transform spectroscopy was used to measure the THz spectrum. For this purpose, the field autocorrelation was recorded with a Michelson interferometer (Figure 53b). The THz spectrum (Figure 53c), obtained by Fourier transformation of the interferogram, has a maximum of the spectral intensity at 0.7 THz and the spectrum extends up to about 2.0 THz. A reasonably good qualitative agreement with the simulated spectrum was found.

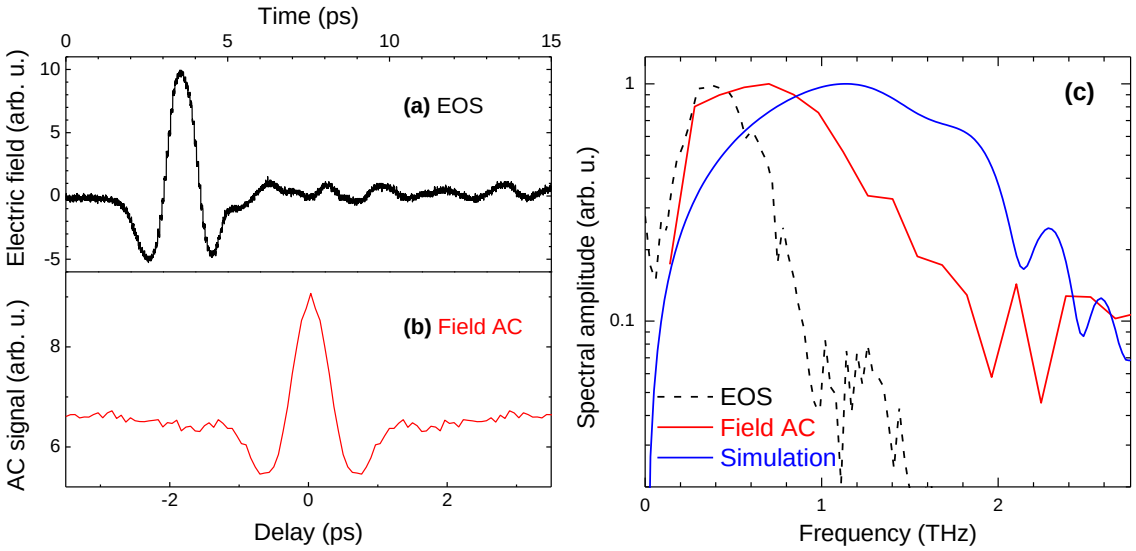

Figure 53. (a) Temporal waveform of THz pulses generated in ZnTe pumped at 1.7 μm, measured by EOS. (b) Field autocorrelation (AC) of THz pulses measured by a Michelson interferometer. (c) Spectral amplitude of THz pulses obtained by Fourier transformation of EOS data (black line) and field AC (red line), and from simulation (blue line). From Ref. [51].

Table 2 summarizes THz pulse generation results with semiconductor nonlinear materials reported by us and compares them to previously published data. The data are classified according to the lowest-order effective MPA, determined by the pump photon energy compared to bandgap. Comparison of the data with 2PA and 3PA as the lowest-order effective MPA shows that eliminating 2PA enables the increase of THz generation efficiency by more than one order of magnitude. Comparing the data of this work with 3PA and 4PA as the lowest-order effective MPA, respectively, indicates that an additional 3.5× increase can be gained by eliminating also 3PA. Semiconductors can compete in efficiency even with LN when optimal conditions (pump wavelength, intensity, pulse duration, material thickness) are applied. The significantly smaller effective nonlinear coefficient of semiconductors, as compared to that of LN, can be compensated for by a larger effective interaction length, enabled by the much smaller PFT angle. Furthermore, a small tilt angle is very advantageous for the realization of a semiconductor contact-grating THz source with exceptionally favourable energy scaling properties [50, 132, 143, 177].

In conclusion, it was demonstrated both numerically and experimentally that semiconductor materials, pumped at an infrared wavelength sufficiently long to suppress 2PA and 3PA, offer a new route to efficient generation of THz pulses with high-energy. The suppression of FCA at THz frequencies, associated with low-order MPA, enables high-intensity pumping, which consequently leads to unprecedentedly high THz generation efficiencies. At such long pump wavelengths TPFP is needed for phase matching.

Using a ZnTe TPFP source, pumped at 1.7 μm wavelength, as high as 0.7% THz generation efficiency was demonstrated. This is 14 times higher than the highest previously reported value for any semiconductor [49], and the vast 220 times higher than previously reported for ZnTe [68]. Such a high efficiency is comparable to that achieved with LN at high pulse energies [102]. Furthermore, it was shown that the THz generation

efficiency in semiconductors can be increased by more than one order of magnitude in case of pumping beyond the 2PA cut-off, as compared to pumping below it [68]. The measurements also indicate the saturation of 3PA. Further increase of the efficiency by a factor of 3.5 was observed in case of pumping above the 3PA edge, as compared to pumping below it. An estimation of $\beta_4 = (3 \pm 1) \times 10^{-5}$ cm^5/GW^3 for the 4PA coefficient was given for ZnTe.

THz pulses with as high as 14 μJ energy were generated, 9× higher than the highest previously reported value for semiconductors [68]. Further increase of the THz pulse energy to the mJ level can be expected by increasing the pump spot size to a few cm and scaling the pump pulse energy to the 100-mJ level, in combination with the scalable monolithic contact-grating technology [50]. Such new THz sources, in combination with novel efficient infrared pump sources in the 1.7 to 2.5 μm wavelength range based, for example, on Holmium laser technology [172, 173], opens new perspectives for THz high-field applications. These range from strong-field control of matter to compact sources of high-energy particles and X-ray beams, key technologies in medicine and materials science.

Table 2. Comparison of THz generation results. Data are classified according to the lowest-order effective MPA, determined by the pump photon energy compared to bandgap. λ_{pump}: pump wavelength, γ: PFT angle. (The efficiency and THz pulse energy values in parentheses refer to those presented in Figure 45.)

Lowest-order effective MPA	2PA	3PA		4PA		
Material	ZnTe	ZnTe	GaAs	ZnTe	GaP	LN
Ref.	[68]	[51]	[49]	[51]	[51]	[102]
λ_{pump} [μm]	0.8	1.45	1.8	1.7	1.7	1.03
γ	0° (collinear)	27°	14°	28°	21°	63°
Max. efficiency [$\times 10^{-5}$]	3.1	(40)	50	700 (140)	(60)	770
Max. THz energy [μJ]	1.5	(0.11)	0.6	14 (0.46)	(0.11)	436

IV. Summary

1. Temporal shaping of the pump pulses enables to increase the efficiency of optical parametric amplification and to reduce distortions of the amplified spectrum. For this purpose, a novel pulse-stacking interferometer setup was proposed for the shaping of picosecond pulses, using birefringent prism pairs for beam splitting and recombination. This device enabled the fully flexible synthesis of any pulse shape allowed by the pulse-stacking principle by independently adjusting the relative intensities and delays (both on interferometric as well as on larger time scales) of the individual pulses. The shaping and amplification of picosecond pulses to the 100-mJ level was demonstrated [105].

2. Ultrabroadband optical parametric chirped-pulse amplification (OPCPA) of few-cycle pulses up to 250 μJ energy was demonstrated pumped by short pulses of about 100 fs duration [115]. The amplified pulses were compressed to 8 fs, close to the Fourier limit, with the help of specifically designed chirped mirrors. These results demonstrated the feasibility of the short-pulse pumped OPCPA concept for the generation of high-power few-cycle pulses, and showed that it can enable the construction of PW-scale OPCPA systems.

3. A numerical model was developed [41], which enabled the detailed analysis of the prospects and limitations of THz sources based on optical rectification by tilted-pulse-front pumping [24, 52]. The model takes into account the variation of the pump pulse duration caused by material and angular dispersion, the linear and free-carrier absorption in the THz range, the latter caused by multi-photon absorption of the pump. With this model, the dependence of the THz generation efficiency, peak electric field strength, and spectrum was studied on the Fourier limited pump pulse duration, crystal temperature, and crystal length [127]. Optimal pump pulse durations were given for maximizing the THz generation efficiency [41] and peak electric field strength [126]. A 6-fold increase of the THz generation efficiency was predicted for $LiNbO_3$ by using 500-fs pump pulses rather than the commonly used ~100 fs [126]. An additional 4 to 6-fold increase was predicted by cryogenic cooling of the crystal [126].

4. For the generation of THz pulses with extremely high energy a pump spot size as large as up to several cm is needed. A two-dimensional model, accounting for the noncollinear phase-matching geometry, was developed for the simulation of the THz generation in a TPFP scheme with an extended pump beam [41]. It was shown with numerical simulations that for a pulse-front tilting setup containing a lens, imaging errors can significantly reduce the THz generation efficiency in $LiNbO_3$ [132]. The THz generation efficiency was shown to increase significantly by using a telescope for imaging or a contact grating without imaging, newly proposed by us [132]. Furthermore, it was shown that imaging errors can results in a strong distortion of the THz beam [41]. Such distortions can be significantly reduced by optimized imaging, and eliminated by using a contact grating for pulse-front tilt.

5. The efficiency of THz generation in $LiNbO_3$ at room temperature was increased significantly by using pump pulses with a duration longer than the commonly used ~100 fs. THz pulses with a record-high 125 μJ energy were generated at 0.25%

efficiency [146] by using 1.3-ps pump pulses, longer than the theoretically predicted optimum of about 500 fs, and optimized imaging for pulse-front tilt. Both THz pulse energy and generation efficiency were about 2.5 times higher than the highest previously demonstrated values. By using pump pulses with a nearly optimal duration of 785 fs, THz pulses with more than 0.4 mJ energy could be generated at 0.77% efficiency [102]. The achieved THz pulse energy exceeded by about one order of magnitude the highest value previously demonstrated by others.

6. It was experimentally demonstrated for high pump and THz pulse energies that the THz generation efficiency can be increased significantly by cryogenic cooling of the $LiNbO_3$ crystal, in accordance with our calculations. The increase in efficiency was fourfold up to a THz pulse energy of 45 μJ [151], at higher energies up to 100 μJ it was about threefold, whereas at still higher energies up to 186 μJ the increase was about 2.5-fold [102]. Furthermore, THz pulses with low (<0.4 THz) frequency and extremely high field strength on the order of 1 MV/cm were generated in cryogenically cooled $LiNbO_3$ using pump pulses with a nearly optimal pulse duration and optimized imaging for pulse-front tilt [102]. This was the first demonstration of THz pulses suitable for proton acceleration in the optimally fitting low-frequency THz range.

7. An intense THz pulse can cause the spectral broadening of the pump pulse by nonlinear interaction (e.g. by sum- and difference-frequency generation). Our numerical calculations for $LiNbO_3$ showed that such a spectral broadening can result in a strong decrease of the interaction length for THz generation. In consequence, owing to the noncollinear phase matching geometry, the intensity-dependent variation of the THz beam size can be expected. Such a variation was confirmed by near- and far-field THz beam profile measurements [124]. The observed nonlinear distortion of the THz beam can be important for intense THz sources and their applications.

8. High-average-power THz sources with tilted-pulse-front pumping were investigated and designed, which can be advantageous for applications in linear and nonlinear THz spectroscopy or THz imaging. For small ($\lesssim$10 μJ) pump pulse energy and high (1 MHz–100 MHz) repetition rate, a THz source based on a new absorption-reduced planar waveguide structure was investigated and optimized by numerical simulations, taking into account waveguide dispersion and an effective absorption coefficient in the THz range [168]. In the proposed waveguide structure the core is formed by a material with a high nonlinearity but strong THz absorption, such as $LiNbO_3$. Most of the THz power is propagating in the cladding with a weak THz absorption, thereby reducing losses. It was shown that a smaller pulse front tilt angle is required for velocity matching and a larger interaction length can be achieved than in bulk material. Up to 20 times higher conversion efficiency and 50 times higher spectral intensity was predicted than in bulk $LiNbO_3$. For larger (10 μJ–300 μJ) pulse energy with 50 kHz–300 kHz repetition rate a THz source based on bulk $LiNbO_3$ crystal was designed and tested [170].

9. The highly efficient generation of intense THz pulses in semiconductor nonlinear optical materials was predicted by numerical simulations [41, 51, 71]. Using a sufficiently long infrared pump wavelength enables the elimination of lower-order

(second- and possibly third-order) multiphoton absorption. Consequently, the detrimental effect of free-carrier absorption in the THz range can be avoided and a significantly higher pump intensity can be efficiently utilized for optical rectification. Phase matching at longer wavelengths requires tilting the pump pulse front. Up to two orders of magnitude increases in THz generation efficiency was predicted when both two- and three-photon absorption are eliminated in a semiconductor [41, 51]. Thus, semiconductors can compete in efficiency with $LiNbO_3$. Increasing the efficiency by one order of magnitude (as compared to previous work) was experimentally demonstrated in ZnTe by eliminating two-photon absorption, and a further 3.5-fold increase was achieved by eliminating also three-photon absorption [51].

10. A semiconductor (ZnTe) contact-grating THz source was realized and highly efficient (0.3%) generation of THz pulses was demonstrated [50]. The collinear pumping geometry is advantageous for applications and enables good focusability of the THz beam. The source can be scaled to mJ-level energies by increasing the pumped area and the pump energy.

11. According to our simulations, the THz generation efficiency, and the energy and field strength of THz pulses can be significantly further increased by utilizing longer semiconductor crystals, optimal pump pulse duration and intensity, and the more advantageous material GaP, rather than ZnTe [50, 51, 71]]. The efficient generation of high-energy THz pulses in ZnTe semiconductor was experimentally demonstrated [51], in good agreement with theoretical predictions. Two- and three-photon absorption were eliminated by pumping at 1.7 μm wavelength, and a pulse-front-tilting setup with imaging was applied. As high as 0.7% efficiency was achieved, 220 times higher than reported previously in the same material. The THz pulse energy reached 14 μJ, one order of magnitude higher than previously reported. Based on our measurements, an estimation was given for the four-photon absorption coefficient of ZnTe [71].

8. Magyar nyelvű összefoglaló

1. Optikai parametrikus erősítők nagyobb hatásfokú pumpálása, valamint az erősítés spektrumot torzító hatásának csökkentése elérhető a pumpáló impulzusok megfelelő időbeli alakformálásával. Ebből a célból keskenysávú pikoszekundumos impulzusok alakformálására javasoltam egy interferométert, amely kettőstörő anyagú prizmapárokat alkalmaz nyalábosztóként és a nyalábok újraegyesítésére. Az eszközzel az impulzusok replikálásán alapuló impulzusformálás által megengedett minden szabadsági fok – relatív intenzitások, impulzusok közötti késleltetések interferometrikus és nagyobb léptékű skálán – függetlenül állítható. Megépítettem egy prototípust és demonstráltam a flexibilis impulzusformálás lehetőségét 100 mJ szintű impulzusenergiáig [105].

2. Demonstráltam kevés ciklusú impulzusok ultranagy sávszélességű csörpölt impulzusú optikai parametrikus erősítését (OPCPA) 250 μJ impulzusenergiáig rövid impulzusú (~100 fs), 395 nm központi hullámhosszú pumpálást használva [115]. Egyedi tervezésű dielektrikumtükrök segítségével az erősített impulzusokat összenyomtam 8 fs időtartamra, a Fourier-limit közelébe. Ezzel megmutattam, hogy a rövid impulzusokkal pumpált OPCPA alkalmas nagyintenzitású, kevés ciklusú impulzusok előállítására és így alapja lehet TW–PW teljesítményű OPCPA rendszereknek is.

3. Kifejlesztettem egy numerikus modellt [41], amely alkalmas döntött impulzusfrontú gerjesztéssel történő optikai egyenirányításon alapuló THz-es források lehetőségeinek és korlátainak vizsgálatára [24, 52]. A modell figyelembe veszi a pumpáló impulzus hosszának anyagi és szögdiszperzió miatt bekövetkező változását, a THz-es tartományban a közeg lineáris abszorpcióját, valamint a gerjesztő fényimpulzusok többfotonos abszorpciója révén keletkező szabad töltéshordozók okozta THz-es abszorpciót. A modell segítségével tanulmányoztam a THz keltés hatásfokának, valamint a THz-es impulzusok térerősségnek és spektrális intenzitáseloszlásnak a függését a Fourier-limitált pumpáló impulzushossztól, a kristály hőmérsékletétől és hosszától [127]. Megmutattam, hogy megadható optimális impulzushossz, amellyel a THz keltés hatásfoka [41] illetve térerőssége [126] maximalizálható. Megmutattam, hogy $LiNbO_3$ esetében a mások által jellemzően használt ~100 fs helyett hosszabb, 500 fs körüli pumpáló impulzushosszat használva a hatásfok hatszorosra növelhető [126]. További 4–6-szoros növekedés várható a kristály alacsony hőmérsékletre való hűtésétől [126].

4. Extrém nagy energiájú THz-es impulzusok előállításához szükséges a pumpált foltméret jelentős, akár több cm-re való növelése. Kifejlesztettem egy kétdimenziós modellt döntött impulzusfrontú pumpálással való THz keltés leírására, amely figyelembe vette a pumpa és a THz-es nyalábok nemkollineáris terjedését kiterjedt nyalábok esetében [41]. Numerikus számításokkal megmutattam, hogy a rácsból és lencséből álló impulzusfront-döntő elrendezésnél a leképezési hibák a THz-keltés hatásfokát jelentősen csökkenthetik $LiNbO_3$-ban [132]. Megmutattam, hogy a teleszkópot, illetve az általunk újonnan javasolt kontakt rácsot alkalmazó elrendezéseknél ez a hatásfokcsökkenés nagymértékben enyhíthető, illetve kiküszöbölhető [132]. Megmutattam továbbá, hogy a leképezési hibák a THz-es

nyaláb torzulását okozhatják [41]. A leképezés optimalizálásával ez a torzulás jelentősen csökkenthető, a kontaktrácsos elrendezéssel keltett THz-es impulzusok pedig mentesek az ilyen torzulásoktól.

5. Kísérletileg megmutattam, hogy $LiNbO_3$ kristályban a THz keltés hatásfoka jelentősen megnövelhető, ha a széles körben használt ~100 fs-os pumpáló impulzushossz helyett hosszabb pumpáló impulzusokat használunk. Az elméletileg jósolt ~500 fs-os optimumnál hosszabb, 1,3 ps-os impulzushosszú pumpálással és optimalizált leképezéssel 125 μJ energiájú THz-es impulzusokat állítottam elő 0,25% hatásfokkal [146]. Mind az elért energia, mind a hatásfok mintegy 2,5-szer nagyobb volt, mint a mások által korábban elért legnagyobb értékek. Az optimumhoz közelebb eső, 785 fs-os hosszúságú pumpálással sikerült több mint 0,4 mJ energiájú THz-es impulzusokat előállítani 0,77% hatásfokkal [102]. Az elért impulzusenergia közel egy nagyságrenddel haladta meg a korábban mások által elért legnagyobb értéket.

6. Nagy THz-es impulzusenergiákra kísérletileg megmutattuk, hogy a THz keltés hatásfoka a $LiNbO_3$ kristály hűtésével jelentősen növelhető, összhangban a számításokkal. Ez a növekmény mintegy négyszeres volt 45 μJ impulzusenergiáig [151], efölött 100 μJ impulzusenergiáig közel háromszoros, efölött 186 μJ energiáig pedig 2,5-szeres [102]. Hűtött $LiNbO_3$ kristályt, közel optimális pumpáló impulzushosszat és optimalizált leképező elrendezést használva előállítottam és jellemeztem extrém nagy, 1 MV/cm nagyságrendbe eső térerősségű, alacsony (<0,4 THz) frekvenciájú THz-es impulzusokat [102]. Ezzel elsőként demonstráltunk evaneszcens terű protongyorsításra alkalmas THz-es impulzusokat az ehhez optimálisan illeszkedő alacsony frekvenciás tartományban.

7. Egy intenzív THz-es impulzus nemlineáris kölcsönhatás (pl. összeg- és különbségi-frekvencia keltés) révén az őt keltő pumpáló impulzus spektrális kiszélesedését okozhatja. A kezdményezésemre elvégzett numerikus szimulációk szerint $LiNbO_3$-ban ez a spektrális kiszélesedés jelentősen lecsökkentheti a THz keltés effektív kölcsönhatási hosszát, amely – a nemkollineáris fázisillesztési geometria miatt – a THz nyalábméret intenzitásfüggő változását okozhatja. Kísérletileg kimutattuk ezt a nyalábméret-változást mind a közeli, mind a távoli zónában [124]. A THz-es nyaláb ilyen nemlineáris torzulásának figyelembevétele nagyintenzitású THz-es forrásoknál és ezek alkalmazásainál fontos lehet.

8. Nagy átlagteljesítményű THz-es forrásokat vizsgáltam és terveztem, amelyek lineáris és nemlineáris THz-es spektroszkópiai vizsgálatokban vagy THz-es képalkotásban lehetnek előnyösek. Kis ($\lesssim$10 μJ) impulzusenergiájú, nagy (1 MHz–100 MHz) ismétlési frekvenciájú lézerekkel való pumpáláshoz kettős (pumpa és THz) hullámvezető struktúrájú, döntött impulzusfrontú pumpálással gerjesztett THz-es forrást vizsgáltam és optimalizáltam numerikus szimulációk segítségével, a THz-es hullámvezető diszperzió és effektív abszorpciós együttható figyelembevételével [168]. Ebben az általunk javasolt elrendezésben a THz-es hullámvezető magját nagy nemlinearitású, de egyben nagy abszorpciójú anyag alkotja (pl. $LiNbO_3$). Az abszorpció hatása a kismértékben elnyelő hullámvezető köpennyel jelentősen csökkenthető. Megmutattam, hogy a hullámvezető diszperzióját kihasználva növelhető az effektív kölcsönhatási hossz és a THz keltés hatásfoka több mint

húszszorosra, a spektrális intenzitás több mint ötvenszeresre növelhető a tömbi $LiNbO_3$ kristálybelihez képest. Nagyobb (10 μJ–300 μJ) impulzusenergiájú, 50 kHz–300 kHz ismétlési frekvenciájú pumpáláshoz tömbi $LiNbO_3$ kristályon alapuló THz-es forrást terveztem és teszteltem [170].

9. Numerikus számításokkal megmutattam, hogy félvezető anyagok alkalmasak lehetnek nagy intenzitású THz-es impulzusok hatékony előállítására [41, 51, 71]. Ennek feltétele az alacsonyrendű többfotonos (a két- és lehetőleg a háromfotonos) abszorpció kiküszöbölése elegendően hosszú hullámhosszú infravörös pumpálás alkalmazásával. Így jelentősen csökkenthető a szabad töltéshordozók okozta abszorpció a THz-es tartományban és nagyobb pumpáló intenzitás használható. A pumpáló és a THz-es impulzusok közötti sebességillesztés a pumpa impulzusfrontjának megdöntésével lehetséges. Számításokkal megmutattam, hogy a félvezetőkkel elérhető hatásfok akár két nagyságrenddel megnövelhető, ha a két- és háromfotonos abszorpció hatását kiküszöböljük [41, 51] és így a $LiNbO_3$-belit elérő vagy akár meghaladó hatásfok várható. Kísérletileg megmutattam, hogy ZnTe-ban a THz keltés hatásfoka több mint egy nagyságrenddel megnövelhető (mások korábbi eredményeihez képest) a kétfotonos abszorpció kiküszöbölésével és további 3,5-szeres növekedése érhető el, ha a háromfotonos abszorpciót is kiküszöböljük [51].

10. Megvalósítottam egy félvezető anyagú kontaktrácsos THz-es forrást és demonstráltam THz-es impulzusok nagy (0,3%) hatásfokú keltését [50]. A kollineáris pumpálási geometria az alkalmazások szempontjából igen előnyös és a THz-es nyaláb jó fókuszálhatóságát is biztosítja. A forrás egyszerűen – a felület és a pumpáló energia növelésével – skálázható akár mJ-szintű energiára.

11. Számolásaink szerint a THz keltés hatásfoka, valamint a THz-es impulzusok energiája és térerőssége jelentősen tovább növelhetőek, többek között nagyobb kristályvastagság, optimális pumpáló impulzushossz és intenzitás, illetve a ZnTe-nál várhatóan kedvezőbb tulajdonságú GaP alkalmazásával [50, 51, 71]. Kísérletileg megmutattam, hogy – a számolásokkal összhangban – félvezető anyagok alkalmasak nagy energiájú THz-es impulzusok hatékony előállítására [51]. ZnTe-ban a két- és háromfotonos abszorpciót egyaránt kiküszöbölő 1,7 μm hullámhosszú, leképezést alkalmazó döntött impulzusfrontú pumpálást használva 0,7% hatásfokot értem el, amely 220-szor nagyobb, mint amit korábban mások ugyanebben az anyagban elértek. Az elért 14 μJ THz-es impulzusenergia egy nagyságrenddel haladta meg a korábbi legnagyobb értéket. Méréseink alapján becslést adtam a ZnTe négyfotonos abszorpciós együtthatójára [71].

Acknowledgements

A large part of the work presented in this dissertation was carried out at the Institute of Physics, University of Pécs. I would like to thank the leader of the institute and the MTA-PTE High-Field Terahertz Research Group, János Hebling for his support. Part of the work was carried out at the Max Planck Institute of Quantum Optics in Garching, Germany and at the Ludwig Maximilians University in Munich. I would like to thank the leader of the group and director of the institute, Ferenc Krausz for his support.

The publications forming the basis of this dissertation are the results of common efforts with a number of coauthors. I would like to thank them all for the fruitful cooperation. I would like to thank my colleagues at the Institute of Physics and the Szentágothai Research Centre at University of Pécs for their kind support. Essential ingredient in achieving the presented results was a close collaboration with our colleagues from a number of institutes and industrial partners, especially in carrying out experiments. The most important partners were (in alphabetic order): Amplitude Systemes (Bordeaux, France), ELI-ALPS (Szeged, Hungary), Ludwig Maximilians University (Munich, Germany), Max Planck Institute of Quantum Optics (Garching, Germany), MTA Wigner Research Centre for Physics (Budapest, Hungary), Paul Scherrer Institute (Villigen, Switzerland), SciTech Precision, Ltd. (Oxford, UK), University of Szeged (Szeged, Hungary), Technical University of Vienna (Vienna, Austria), and University of Bern (Bern, Switzerland). I would like to thank all colleagues for the collaboration.

References

[1] J.-C. Diels, W. Rudolph, Ultrashort laser pulse phenomena: fundamentals, techniques, and applications on a femtosecond time scale (Elsevier / Academic Press, Amsterdam; Boston, 2006).

[2] Y.-S. Lee, Principles of terahertz science and technology (Springer, New York, NY, 2009).

[3] R.W. Boyd, Nonlinear optics (Academic Press, Amsterdam; Boston, 2008).

[4] T. Brabec, F. Krausz, Intense few-cycle laser fields: Frontiers of nonlinear optics, Reviews of Modern Physics 72 (2000) 545-591.

[5] G.M. Gale, M. Cavallari, T.J. Driscoll, F. Hache, Sub-20-fs tunable pulses in the visible from an 82-MHz optical parametric oscillator, Optics Letters 20 (1995) 1562-1564.

[6] T. Wilhelm, J. Piel, E. Riedle, Sub-20-fs pulses tunable across the visible from a blue-pumped single-pass noncollinear parametric converter, Optics Letters 22 (1997) 1494-1496.

[7] I.N. Ross, P. Matousek, M. Towrie, A.J. Langley, J.L. Collier, The prospects for ultrashort pulse duration and ultrahigh intensity using optical parametric chirped pulse amplifiers, Optics Communications 144 (1997) 125-133.

[8] G. Cerullo, M. Nisoli, S. Stagira, S. De Silvestri, Sub-8-fs pulses from an ultrabroadband optical parametric amplifier in the visible, Optics Letters 23 (1998) 1283-1285.

[9] A. Shirakawa, I. Sakane, M. Takasaka, T. Kobayashi, Sub-5-fs visible pulse generation by pulse-front-matched noncollinear optical parametric amplification, Applied Physics Letters 74 (1999) 2268-2270.

[10] A. Baltuška, T. Kobayashi, in: Few-cycle laser pulse generation and its applications, ed F.X. Kärtner (Springer Berlin Heidelberg, Berlin, Heidelberg, 2004).

[11] N. Ishii, L. Turi, V.S. Yakovlev, T. Fuji, F. Krausz, A. Baltuška, R. Butkus, G. Veitas, V. Smilgevičius, R. Danielius, A. Piskarskas, Multimillijoule chirped parametric amplification of few-cycle pulses, Optics Letters 30 (2005) 567-569.

[12] S. Witte, R.T. Zinkstok, W. Hogervorst, K.S.E. Eikema, Generation of few-cycle terawatt light pulses using optical parametric chirped pulse amplification, Optics Express 13 (2005) 4903-4908.

[13] S. Witte, R.T. Zinkstok, A.L. Wolf, W. Hogervorst, W. Ubachs, K.S.E. Eikema, A source of 2 terawatt, 2.7 cycle laser pulses based on noncollinear optical parametric chirped pulse amplification, Optics Express 14 (2006) 8168-8177.

[14] G. Cerullo, S. De Silvestri, Ultrafast optical parametric amplifiers, Review of Scientific Instruments 74 (2003) 1-18.

[15] G. Tóth, L. Pálfalvi, L. Tokodi, J. Hebling, J.A. Fülöp, Scalable broadband OPCPA in lithium niobate with signal angular dispersion, Optics Communications 370 (2016) 250-255.

[16] A. Dubietis, G. Jonušauskas, A. Piskarskas, Powerful femtosecond pulse generation by chirped and stretched pulse parametric amplification in BBO crystal, Optics Communications 88 (1992) 437-440.

[17] O.V. Chekhlov, J.L. Collier, I.N. Ross, P.K. Bates, M. Notley, C. Hernandez-Gomez, W. Shaikh, C.N. Danson, D. Neely, P. Matousek, S. Hancock, L. Cardoso, 35 J broadband femtosecond optical parametric chirped pulse amplification system, Optics Letters 31 (2006) 3665-3667.

[18] F. Tavella, A. Marcinkevičius, F. Krausz, 90 mJ parametric chirped pulse amplification of 10 fs pulses, Optics Express 14 (2006) 12822-12827.

[19] T. Kobayashi, A. Shirakawa, Tunable visible and near-infrared pulse generator in a 5 fs regime, Applied Physics B 70 (2000) S239-S246.

[20] A. Shirakawa, I. Sakane, T. Kobayashi, Pulse-front-matched optical parametric amplification for sub-10-fs pulse generation tunable in the visible and near infrared, Optics Letters 23 (1998) 1292-1294.

[21] G. Cerullo, M. Nisoli, S. Stagira, S. De Silvestri, G. Tempea, F. Krausz, K. Ferencz, Mirror-dispersion-controlled sub-10-fs optical parametric amplifier in the visible, Optics Letters 24 (1999) 1529-1531.

[22] P. Tzankov, J. Zheng, M. Mero, D. Polli, C. Manzoni, G. Cerullo, 300 μJ noncollinear optical parametric amplifier in the visible at 1 kHz repetition rate, Optics Letters 31 (2006) 3629-3631.

[23] H. Fattahi, H.G. Barros, M. Gorjan, T. Nubbemeyer, B. Alsaif, C.Y. Teisset, M. Schultze, S. Prinz, M. Haefner, M. Ueffing, A. Alismail, L. Vámos, A. Schwarz, O. Pronin, J. Brons, X.T. Geng, G. Arisholm, M. Ciappina, V.S. Yakovlev, D.-E. Kim, A.M. Azzeer, N. Karpowicz, D. Sutter, Z. Major, T. Metzger, F. Krausz, Third-generation femtosecond technology, Optica 1 (2014) 45-63.

[24] M.C. Hoffmann, J.A. Fülöp, Intense ultrashort terahertz pulses: generation and applications, Journal of Physics D: Applied Physics 44 (2011) 083001.

[25] T. Kampfrath, K. Tanaka, K.A. Nelson, Resonant and nonresonant control over matter and light by intense terahertz transients, Nature Photonics 7 (2013) 680.

[26] D. Nicoletti, A. Cavalleri, Nonlinear light–matter interaction at terahertz frequencies, Advances in Optics and Photonics 8 (2016) 401-464.

[27] L. Pálfalvi, J.A. Fülöp, G. Tóth, J. Hebling, Evanescent-wave proton postaccelerator driven by intense THz pulse, Physical Review Special Topics - Accelerators and Beams 17 (2014) 031301.

[28] S. Fleischer, Y. Zhou, R.W. Field, K.A. Nelson, Molecular orientation and alignment by intense single-cycle THz pulses, Physical Review Letters 107 (2011) 163603.

[29] M. Jewariya, M. Nagai, K. Tanaka, Ladder climbing on the anharmonic intermolecular potential in an amino acid microcrystal via an intense monocycle terahertz pulse, Physical Review Letters 105 (2010) 203003.

[30] T. Kampfrath, A. Sell, G. Klatt, A. Pashkin, S. Mährlein, T. Dekorsy, M. Wolf, M. Fiebig, A. Leitenstorfer, R. Huber, Coherent terahertz control of antiferromagnetic spin waves, Nature Photonics 5 (2010) 31.

[31] H. Hirori, M. Nagai, K. Tanaka, Excitonic interactions with intense terahertz pulses in ZnSe/ZnMgSSe multiple quantum wells, Physical Review B 81 (2010) 081305.

[32] E.A. Nanni, W.R. Huang, K.-H. Hong, K. Ravi, A. Fallahi, G. Moriena, R.J. Dwayne Miller, F.X. Kärtner, Terahertz-driven linear electron acceleration, Nature Communications 6 (2015) 8486.

[33] J.R. Morris, Y.R. Shen, Far-infrared generation by picosecond pulses in electro-optical materials, Optics Communications 3 (1971) 81-84.

[34] K.H. Yang, P.L. Richards, Y.R. Shen, Generation of far- infrared radiation by picosecond light pulses in LiNbO3, Applied Physics Letters 19 (1971) 320-323.

[35] D.H. Auston, K.P. Cheung, J.A. Valdmanis, D.A. Kleinman, Cherenkov radiation from femtosecond optical pulses in electro-optic media, Physical Review Letters 53 (1984) 1555-1558.

[36] K.L. Vodopyanov, Optical generation of narrow-band terahertz packets in periodically-inverted electro-optic crystals: conversion efficiency and optimal laser pulse format, Optics Express 14 (2006) 2263-2276.

[37] R.L. Sutherland, D.G. McLean, S. Kirkpatrick, Handbook of nonlinear optics (Marcel Dekker, New York, 2003).

[38] Q. Wu, X.C. Zhang, Ultrafast electro- optic field sensors, Applied Physics Letters 68 (1996) 1604-1606.

[39] J. Hebling, A.G. Stepanov, G. Almási, B. Bartal, J. Kuhl, Tunable THz pulse generation by optical rectification of ultrashort laser pulses with tilted pulse fronts, Applied Physics B 78 (2004) 593-599.

[40] J. Hebling, K.-L. Yeh, M.C. Hoffmann, B. Bartal, K.A. Nelson, Generation of high-power terahertz pulses by tilted-pulse-front excitation and their application possibilities, Journal of the Optical Society of America B 25 (2008) B6-B19.

[41] J.A. Fülöp, L. Pálfalvi, G. Almási, J. Hebling, Design of high-energy terahertz sources based on optical rectification, Optics Express 18 (2010) 12311-12327.

[42] J.-H. Jeong, B.-J. Kang, J.-S. Kim, M. Jazbinsek, S.-H. Lee, S.-C. Lee, I.-H. Baek, H. Yun, J. Kim, Y.S. Lee, J.-H. Lee, J.-H. Kim, F. Rotermund, O.P. Kwon, High-power broadband organic THz generator, Scientific Reports 3 (2013) 3200.

[43] K. Wynne, J.J. Carey, An integrated description of terahertz generation through optical rectification, charge transfer, and current surge, Optics Communications 256 (2005) 400-413.

[44] M.C. Hoffmann, K.-L. Yeh, J. Hebling, K.A. Nelson, Efficient terahertz generation by optical rectification at 1035 nm, Optics Express 15 (2007) 11706-11713.

[45] T. Hattori, K. Takeuchi, Simulation study on cascaded terahertz pulse generation in electro-optic crystals, Optics Express 15 (2007) 8076-8093.

[46] M. Jewariya, M. Nagai, K. Tanaka, Enhancement of terahertz wave generation by cascaded $\chi^{(2)}$ processes in LiNbO3, Journal of the Optical Society of America B 26 (2009) A101-A106.

[47] K. Ravi, W.R. Huang, S. Carbajo, X. Wu, F. Kärtner, Limitations to THz generation by optical rectification using tilted pulse fronts, Optics Express 22 (2014) 20239-20251.

[48] J. Hebling, G. Almási, I.Z. Kozma, J. Kuhl, Velocity matching by pulse front tilting for large-area THz-pulse generation, Optics Express 10 (2002) 1161-1166.

[49] F. Blanchard, B.E. Schmidt, X. Ropagnol, N. Thiré, T. Ozaki, R. Morandotti, D.G. Cooke, F. Légaré, Terahertz pulse generation from bulk GaAs by a tilted-pulse-front excitation at 1.8 μm, Applied Physics Letters 105 (2014) 241106.

[50] J.A. Fülöp, G. Polónyi, B. Monoszlai, G. Andriukaitis, T. Balciunas, A. Pugzlys, G. Arthur, A. Baltuska, J. Hebling, Highly efficient scalable monolithic semiconductor terahertz pulse source, Optica 3 (2016) 1075-1078.

[51] G. Polónyi, B. Monoszlai, G. Gäumann, E.J. Rohwer, G. Andriukaitis, T. Balciunas, A. Pugzlys, A. Baltuska, T. Feurer, J. Hebling, J.A. Fülöp, High-energy terahertz pulses from semiconductors pumped beyond the three-photon absorption edge, Optics Express 24 (2016) 23872-23882.

[52] J.A. Fülöp, J. Hebling, in: Recent optical and photonic technologies, ed K.Y. Kim (InTech, Rijeka, 2010).

[53] J. Hebling, Derivation of the pulse front tilt caused by angular dispersion, Optical and Quantum Electronics 28 (1996) 1759-1763.

[54] O.E. Martinez, J.P. Gordon, R.L. Fork, Negative group-velocity dispersion using refraction, Journal of the Optical Society of America A 1 (1984) 1003-1006.

[55] L. Pálfalvi, J. Hebling, J. Kuhl, Á. Péter, K. Polgár, Temperature dependence of the absorption and refraction of Mg-doped congruent and stoichiometric $LiNbO_3$ in the THz range, Journal of Applied Physics 97 (2005) 123505.

[56] B. Bartal, I.Z. Kozma, A.G. Stepanov, G. Almási, J. Kuhl, E. Riedle, J. Hebling, Toward generation of μJ range sub-ps THz pulses by optical rectification, Applied Physics B 86 (2007) 419-423.

[57] L. Pálfalvi, J. Hebling, G. Almási, Á. Péter, K. Polgár, K. Lengyel, R. Szipöcs, Nonlinear refraction and absorption of Mg doped stoichiometric and congruent $LiNbO_3$, Journal of Applied Physics 95 (2004) 902-908.

[58] A.G. Stepanov, J. Hebling, J. Kuhl, Efficient generation of subpicosecond terahertz radiation by phase-matched optical rectification using ultrashort laser pulses with tilted pulse fronts, Applied Physics Letters 83 (2003) 3000-3002.

[59] A.G. Stepanov, J. Kuhl, I.Z. Kozma, E. Riedle, G. Almási, J. Hebling, Scaling up the energy of THz pulses created by optical rectification, Optics Express 13 (2005) 5762-5768.

[60] K.L. Yeh, M.C. Hoffmann, J. Hebling, K.A. Nelson, Generation of 10 μJ ultrashort terahertz pulses by optical rectification, Applied Physics Letters 90 (2007) 171121.

[61] A.G. Stepanov, L. Bonacina, S.V. Chekalin, J.-P. Wolf, Generation of 30 μJ single-cycle terahertz pulses at 100 Hz repetition rate by optical rectification, Optics Letters 33 (2008) 2497-2499.

[62] A.G. Stepanov, S. Henin, Y. Petit, L. Bonacina, J. Kasparian, J.P. Wolf, Mobile source of high-energy single-cycle terahertz pulses, Applied Physics B 101 (2010) 11-14.

[63] H. Hirori, A. Doi, F. Blanchard, K. Tanaka, Single-cycle terahertz pulses with amplitudes exceeding 1 MV/cm generated by optical rectification in $LiNbO_3$, Applied Physics Letters 98 (2011) 091106.

[64] M. Sajadi, M. Wolf, T. Kampfrath, Terahertz-field-induced optical birefringence in common window and substrate materials, Optics Express 23 (2015) 28985-28992.

[65] D. You, R.R. Jones, P.H. Bucksbaum, D.R. Dykaar, Generation of high-power sub-single-cycle 500-fs electromagnetic pulses, Optics Letters 18 (1993) 290-292.

[66] R.R. Jones, D. You, P.H. Bucksbaum, Ionization of Rydberg atoms by subpicosecond half-cycle electromagnetic pulses, Physical Review Letters 70 (1993) 1236-1239.

[67] X. Ropagnol, F. Blanchard, T. Ozaki, M. Reid, Intense terahertz generation at low frequencies using an interdigitated ZnSe large aperture photoconductive antenna, Applied Physics Letters 103 (2013) 161108.

[68] F. Blanchard, L. Razzari, H.C. Bandulet, G. Sharma, R. Morandotti, J.C. Kieffer, T. Ozaki, M. Reid, H.F. Tiedje, H.K. Haugen, F.A. Hegmann, Generation of 1.5 μJ single-cycle terahertz pulses by optical rectification from a large aperture ZnTe crystal, Optics Express 15 (2007) 13212-13220.

[69] F. Junginger, A. Sell, O. Schubert, B. Mayer, D. Brida, M. Marangoni, G. Cerullo, A. Leitenstorfer, R. Huber, Single-cycle multiterahertz transients with peak fields above 10 MV/cm, Optics Letters 35 (2010) 2645-2647.

[70] A. Sell, A. Leitenstorfer, R. Huber, Phase-locked generation and field-resolved detection of widely tunable terahertz pulses with amplitudes exceeding 100 MV/cm, Optics Letters 33 (2008) 2767-2769.

[71] G. Polónyi, M.I. Mechler, J. Hebling, J.A. Fülöp, Prospects of semiconductor terahertz pulse sources, IEEE Journal of Selected Topics in Quantum Electronics 23 (2017) 8501508.

[72] A. Leitenstorfer, S. Hunsche, J. Shah, M.C. Nuss, W.H. Knox, Detectors and sources for ultrabroadband electro-optic sampling: Experiment and theory, Applied Physics Letters 74 (1999) 1516-1518.

[73] X.C. Zhang, X.F. Ma, Y. Jin, T.M. Lu, E.P. Boden, P.D. Phelps, K.R. Stewart, C.P. Yakymyshyn, Terahertz optical rectification from a nonlinear organic crystal, Applied Physics Letters 61 (1992) 3080-3082.

[74] T.J. Carrig, G. Rodriguez, T. Sharp Clement, A.J. Taylor, K.R. Stewart, Generation of terahertz radiation using electro- optic crystal mosaics, Applied Physics Letters 66 (1995) 10-12.

[75] T. Taniuchi, S. Okada, H. Nakanishi, Widely tunable terahertz-wave generation in an organic crystal and its spectroscopic application, Journal of Applied Physics 95 (2004) 5984-5988.

[76] C.P. Hauri, C. Ruchert, C. Vicario, F. Ardana, Strong-field single-cycle THz pulses generated in an organic crystal, Applied Physics Letters 99 (2011) 161116.

[77] C. Vicario, M. Jazbinsek, A.V. Ovchinnikov, O.V. Chefonov, S.I. Ashitkov, M.B. Agranat, C.P. Hauri, High efficiency THz generation in DSTMS, DAST and OH1 pumped by Cr:forsterite laser, Optics Express 23 (2015) 4573-4580.

[78] C. Vicario, A.V. Ovchinnikov, S.I. Ashitkov, M.B. Agranat, V.E. Fortov, C.P. Hauri, Generation of 0.9-mJ THz pulses in DSTMS pumped by a Cr:Mg_2SiO_4 laser, Optics Letters 39 (2014) 6632-6635.

[79] C. Vicario, B. Monoszlai, C.P. Hauri, GV/m single-cycle terahertz fields from a laser-driven large-size partitioned organic crystal, Physical Review Letters 112 (2014) 213901.

[80] C. Ruchert, C. Vicario, C.P. Hauri, Scaling submillimeter single-cycle transients toward megavolts per centimeter field strength via optical rectification in the organic crystal OH1, Optics Letters 37 (2012) 899-901.

[81] A. Schneider, M. Neis, M. Stillhart, B. Ruiz, R.U.A. Khan, P. Günter, Generation of terahertz pulses through optical rectification in organic DAST crystals: theory and experiment, Journal of the Optical Society of America B 23 (2006) 1822-1835.

[82] C. Vicario, B. Monoszlai, M. Jazbinsek, S.H. Lee, O.P. Kwon, C.P. Hauri, Intense, carrier frequency and bandwidth tunable quasi single-cycle pulses from an organic emitter covering the terahertz frequency gap, Scientific Reports 5 (2015) 14394.

[83] M. Walther, K. Jensby, S.R. Keiding, H. Takahashi, H. Ito, Far-infrared properties of DAST, Optics Letters 25 (2000) 911-913.

[84] M.C. Hoffmann, J. Hebling, H.Y. Hwang, K.-L. Yeh, K.A. Nelson, Impact ionization in InSb probed by terahertz pump—terahertz probe spectroscopy, Physical Review B 79 (2009) 161201.

[85] P. Gaal, K. Reimann, M. Woerner, T. Elsaesser, R. Hey, K.H. Ploog, Nonlinear terahertz response of n-type GaAs, Physical Review Letters 96 (2006) 187402.

[86] L. Razzari, F.H. Su, G. Sharma, F. Blanchard, A. Ayesheshim, H.C. Bandulet, R. Morandotti, J.C. Kieffer, T. Ozaki, M. Reid, F.A. Hegmann, Nonlinear ultrafast modulation of the optical absorption of intense few-cycle terahertz pulses in n-doped semiconductors, Physical Review B 79 (2009) 193204.

[87] J. Hebling, M.C. Hoffmann, H.Y. Hwang, K.-L. Yeh, K.A. Nelson, Observation of nonequilibrium carrier distribution in Ge, Si, and GaAs by terahertz pump—terahertz probe measurements, Physical Review B 81 (2010) 035201.

[88] A. Dienst, M.C. Hoffmann, D. Fausti, J.C. Petersen, S. Pyon, T. Takayama, H. Takagi, A. Cavalleri, Bi-directional ultrafast electric-field gating of interlayer charge transport in a cuprate superconductor, Nature Photonics 5 (2011) 485.

[89] S. Watanabe, N. Minami, R. Shimano, Intense terahertz pulse induced exciton generation in carbon nanotubes, Optics Express 19 (2011) 1528-1538.

[90] J. Hebling, K.L. Yeh, M.C. Hoffmann, K.A. Nelson, High-power THz generation, THz nonlinear optics, and THz nonlinear spectroscopy, IEEE Journal of Selected Topics in Quantum Electronics 14 (2008) 345-353.

[91] B.S. Dastrup, J.R. Hall, J.A. Johnson, Experimental determination of the interatomic potential in $LiNbO_3$ via ultrafast lattice control, Applied Physics Letters 110 (2017) 162901.

[92] C.L. Korpa, T. Gy, J. Hebling, Interplay of diffraction and nonlinear effects in the propagation of ultrashort pulses, Journal of Physics B: Atomic, Molecular and Optical Physics 49 (2016) 035401.

[93] I. Katayama, H. Aoki, J. Takeda, H. Shimosato, M. Ashida, R. Kinjo, I. Kawayama, M. Tonouchi, M. Nagai, K. Tanaka, Ferroelectric soft mode in a $SrTiO_3$ thin film impulsively driven to the anharmonic regime using intense picosecond terahertz pulses, Physical Review Letters 108 (2012) 097401.

[94] W. Hong, P. Lu, P. Lan, Q. Zhang, X. Wang, Few-cycle attosecond pulses with stabilized-carrier-envelope phase in the presence of a strong terahertz field, Optics Express 17 (2009) 5139-5146.

[95] E. Balogh, K. Kovacs, P. Dombi, J.A. Fulop, G. Farkas, J. Hebling, V. Tosa, K. Varju, Single attosecond pulse from terahertz-assisted high-order harmonic generation, Physical Review A 84 (2011) 023806.

[96] K. Kovács, E. Balogh, J. Hebling, V. Toşa, K. Varjú, Quasi-phase-matching high-harmonic radiation using chirped THz pulses, Physical Review Letters 108 (2012) 193903.

[97] E. Balogh, J.A. Fülöp, J. Hebling, P. Dombi, G. Farkas, K. Varjú, Application of high intensity THz pulses for gas high harmonic generation, Central European Journal of Physics 11 (2013) 1135-1140.

[98] J. Hebling, J.A. Fülöp, M.I. Mechler, L. Pálfalvi, C. Tőke, G. Almási, Optical manipulation of relativistic electron beams using THz pulses, arXiv (2011).

[99] P. Baum, A.H. Zewail, Breaking resolution limits in ultrafast electron diffraction and microscopy, Proceedings of the National Academy of Sciences 103 (2006) 16105-16110.

[100] W.R. Huang, E.A. Nanni, K. Ravi, K.-H. Hong, A. Fallahi, L.J. Wong, P.D. Keathley, L.E. Zapata, F.X. Kärtner, Toward a terahertz-driven electron gun, Scientific Reports 5 (2015) 14899.

[101] W. Ronny Huang, A. Fallahi, X. Wu, H. Cankaya, A.-L. Calendron, K. Ravi, D. Zhang, E.A. Nanni, K.-H. Hong, F.X. Kärtner, Terahertz-driven, all-optical electron gun, Optica 3 (2016) 1209-1212.

[102] J.A. Fülöp, Z. Ollmann, C. Lombosi, C. Skrobol, S. Klingebiel, L. Pálfalvi, F. Krausz, S. Karsch, J. Hebling, Efficient generation of THz pulses with 0.4 mJ energy, Optics Express 22 (2014) 20155-20163.

[103] A. Sharma , Z. Tibai, J. Hebling, Intense tera-hertz laser driven proton acceleration in plasmas, Physics of Plasmas 23 (2016).

[104] I.N. Ross, P. Matousek, G.H.C. New, K. Osvay, Analysis and optimization of optical parametric chirped pulse amplification, Journal of the Optical Society of America B 19 (2002) 2945-2956.

[105] J.A. Fülöp, Z. Major, B. Horváth, F. Tavella, A. Baltuška, F. Krausz, Shaping of picosecond pulses for pumping optical parametric amplification, Applied Physics B 87 (2007) 79-84.

[106] L.J. Waxer, V. Bagnoud, I.A. Begishev, M.J. Guardalben, J. Puth, J.D. Zuegel, High-conversion-efficiency optical parametric chirped-pulse amplification system using spatiotemporally shaped pump pulses, Optics Letters 28 (2003) 1245-1247.

[107] J. Desbois, F. Gires, P. Turnois, A new approach to picosecond laser pulse analysis shaping and coding, IEEE Journal of Quantum Electronics 9 (1973) 213-218.

[108] P. Emplit, J.P. Hamaide, F. Reynaud, Passive amplitude and phase picosecond pulse shaping, Optics Letters 17 (1992) 1358-1360.

[109] B. Colombeau, M. Vampouille, C. Froehly, Shaping of short laser pulses by passive optical Fourier techniques, Optics Communications 19 (1976) 201-204.

[110] C. Froehly, B. Colombeau, M. Vampouille, in: Progress in Optics, ed E. Wolf (Elsevier, 1983).

[111] W.E. Martin, D. Milam, Interpulse interference and passive laser pulse shapers, Applied Optics 15 (1976) 3054-3061.

[112] C.E. Thomas, L.D. Siebert, Pulse shape generator for laser fusion, Applied Optics 15 (1976) 462-465.

[113] C.W. Siders, J.L.W. Siders, A.J. Taylor, S.-G. Park, A.M. Weiner, Efficient high-energy pulse-train generation using a 2n-pulse Michelson interferometer, Applied Optics 37 (1998) 5302-5305.

[114] L.M. Frantz, J.S. Nodvik, Theory of pulse propagation in a laser amplifier, Journal of Applied Physics 34 (1963) 2346-2349.

[115] J.A. Fülöp, Zs. Major, A. Henig, S. Kruber, R. Weingartner, T. Clausnitzer, E.B. Kley, A. Tünnermann, V. Pervak, A. Apolonski, J. Osterhoff, R. Hörlein, F. Krausz, S. Karsch, Short-pulse optical parametric chirped-pulse amplification for the generation of high-power few-cycle pulses, New Journal of Physics 9 (2007) 438.

[116] Z. Major, S.A. Trushin, I. Ahmad, M. Siebold, C. Wandt, S. Klingebiel, T.-J. Wang, J.A. Fülöp, A. Henig, S. Kruber, R. Weingartner, A. Popp, J. Osterhoff, R. Hörlein, J. Hein, V. Pervak, A. Apolonski, F. Krausz, S. Karsch, Basic concepts and current status of the Petawatt Field Synthesizer－A new approach to ultrahigh field generation, The Review of Laser Engineering 37 (2009) 431-436.

[117] C. Iaconis, I.A. Walmsley, Spectral phase interferometry for direct electric-field reconstruction of ultrashort optical pulses, Optics Letters 23 (1998) 792-794.

[118] P.M. Celliers, K.G. Estabrook, R.J. Wallace, J.E. Murray, L.B. Da Silva, B.J. MacGowan, B.M. Van Wonterghem, K.R. Manes, Spatial filter pinhole for high-energy pulsed lasers, Applied Optics 37 (1998) 2371-2378.

[119] T. Clausnitzer, J. Limpert, K. Zöllner, H. Zellmer, H.-J. Fuchs, E.-B. Kley, A. Tünnermann, M. Jupé, D. Ristau, Highly efficient transmission gratings in fused silica for chirped-pulse amplification systems, Applied Optics 42 (2003) 6934-6938.

[120] M. Nisoli, S. Stagira, S. De Silvestri, O. Svelto, S. Sartania, Z. Cheng, M. Lenzner, C. Spielmann, F. Krausz, A novel-high energy pulse compression system: generation of multigigawatt sub-5-fs pulses, Applied Physics B 65 (1997) 189-196.

[121] H. Mashiko, C.M. Nakamura, C. Li, E. Moon, H. Wang, J. Tackett, Z. Chang, Carrier-envelope phase stabilized 5.6 fs, 1.2 mJ pulses, Applied Physics Letters 90 (2007) 161114.

[122] O.E. Martinez, Pulse distortions in tilted pulse schemes for ultrashort pulses, Optics Communications 59 (1986) 229-232.

[123] A. Yariv, Quantum electronics (Wiley, New York, 1989).

[124] Cs. Lombosi, Gy. Polónyi, M. Mechler, Z. Ollmann, J. Hebling, J.A. Fülöp, Nonlinear distortion of intense THz beams, New Journal of Physics 17 (2015) 083041.

[125] P.Y. Yu, M. Cardona, Fundamentals of semiconductors: physics and materials properties (Springer, Berlin ; New York, 2010).

[126] J.A. Fülöp, L. Pálfalvi, M.C. Hoffmann, J. Hebling, Towards generation of mJ-level ultrashort THz pulses by optical rectification, Optics Express 19 (2011) 15090-15097.

[127] J.A. Fülöp, L. Pálfalvi, G. Almási, J. Hebling, High energy THz pulse generation by tilted pulse front excitation and its nonlinear optical applications, Journal of Infrared, Millimeter, and Terahertz Waves 32 (2011) 553-561.

[128] G. Imeshev, M.E. Fermann, K.L. Vodopyanov, M.M. Fejer, X. Yu, J.S. Harris, D. Bliss, C. Lynch, High-power source of THz radiation based on orientation-patterned GaAs pumped by a fiber laser, Optics Express 14 (2006) 4439-4444.

[129] G. Chang, C.J. Divin, C.-H. Liu, S.L. Williamson, A. Galvanauskas, T.B. Norris, Power scalable compact THz system based on an ultrafast Yb-doped fiber amplifier, Optics Express 14 (2006) 7909-7913.

[130] G. Chang, C.J. Divin, J. Yang, M.A. Musheinish, S.L. Williamson, A. Galvanauskas, T.B. Norris, GaP waveguide emitters for high power broadband THz generation pumped by Yb-doped fiber lasers, Optics Express 15 (2007) 16308-16315.

[131] M.C. Hoffmann, K.-L. Yeh, H.Y. Hwang, T.S. Sosnowski, B.S. Prall, J. Hebling, K.A. Nelson, Fiber laser pumped high average power single-cycle terahertz pulse source, Applied Physics Letters 93 (2008) 141107.

[132] L. Pálfalvi, J.A. Fülöp, G. Almási, J. Hebling, Novel setups for extremely high power single-cycle terahertz pulse generation by optical rectification, Applied Physics Letters 92 (2008) 171107.

[133] K.-L. Yeh, J. Hebling, M.C. Hoffmann, K.A. Nelson, Generation of high average power 1kHz shaped THz pulses via optical rectification, Optics Communications 281 (2008) 3567-3570.

[134] A.E. Kaplan, Diffraction-induced transformation of near-cycle and subcycle pulses, Journal of the Optical Society of America B 15 (1998) 951-956.

[135] M. Cronin-Golomb, Cascaded nonlinear difference-frequency generation of enhanced terahertz wave production, Optics Letters 29 (2004) 2046-2048.

[136] F. Blanchard, X. Ropagnol, H. Hafez, H. Razavipour, M. Bolduc, R. Morandotti, T. Ozaki, D.G. Cooke, Effect of extreme pump pulse reshaping on intense terahertz emission in lithium niobate at multimilliJoule pump energies, Optics Letters 39 (2014) 4333-4336.

[137] X. Wu, S. Carbajo, K. Ravi, F. Ahr, G. Cirmi, Y. Zhou, O.D. Mücke, F.X. Kärtner, Terahertz generation in lithium niobate driven by Ti:sapphire laser pulses and its limitations, Optics Letters 39 (2014) 5403-5406.

[138] M. Nagai, M. Jewariya, Y. Ichikawa, H. Ohtake, T. Sugiura, Y. Uehara, K. Tanaka, Broadband and high power terahertz pulse generation beyond excitation bandwidth limitation via $\chi^{(2)}$ cascaded processes in $LiNbO_3$, Optics Express 17 (2009) 11543-11549.

[139] A.G. Stepanov, J. Hebling, J. Kuhl, THz generation via optical rectification with ultrashort laser pulse focused to a line, Applied Physics B 81 (2005) 23-26.

[140] I.Z. Kozma, G. Almási, J. Hebling, Geometrical optical modeling of femtosecond setups having angular dispersion, Applied Physics B 76 (2003) 257-261.

[141] N. Keisuke, K. Atsushi, Design of rectangular transmission gratings fabricated in $LiNbO_3$ for high-power terahertz-wave generation, Japanese Journal of Applied Physics 49 (2010) 122504.

[142] Z. Ollmann, J. Hebling, G. Almási, Design of a contact grating setup for mJ-energy THz pulse generation by optical rectification, Applied Physics B 108 (2012) 821-826.

[143] Z. Ollmann, J.A. Fülöp, J. Hebling, G. Almási, Design of a high-energy terahertz pulse source based on ZnTe contact grating, Optics Communications 315 (2014) 159-163.

[144] M.I. Bakunov, S.B. Bodrov, E.A. Mashkovich, Terahertz generation with tilted-front laser pulses: dynamic theory for low-absorbing crystals, Journal of the Optical Society of America B 28 (2011) 1724-1734.

[145] S. Klingebiel, C. Wandt, C. Skrobol, I. Ahmad, S.A. Trushin, Z. Major, F. Krausz, S. Karsch, High energy picosecond Yb:YAG CPA system at 10 Hz repetition rate for pumping optical parametric amplifiers, Optics Express 19 (2011) 5357-5363.

[146] J.A. Fülöp, L. Pálfalvi, S. Klingebiel, G. Almási, F. Krausz, S. Karsch, J. Hebling, Generation of sub-mJ terahertz pulses by optical rectification, Optics Letters 37 (2012) 557-559.

[147] S.A. Ku, C.M. Tu, W.C. Chu, C.W. Luo, K.H. Wu, A. Yabushita, C.C. Chi, T. Kobayashi, Saturation of the free carrier absorption in ZnTe crystals, Optics Express 21 (2013) 13930-13937.

[148] A.G. Stepanov, J. Hebling, J. Kuhl, Frequency and temperature dependence of the TO phonon-polariton decay in GaP, Physical Review B 63 (2001) 104304.

[149] Y.S. Lee, T. Meade, M. DeCamp, T.B. Norris, A. Galvanauskas, Temperature dependence of narrow-band terahertz generation from periodically poled lithium niobate, Applied Physics Letters 77 (2000) 1244-1246.

[150] S.-W. Huang, E. Granados, W.R. Huang, K.-H. Hong, L.E. Zapata, F.X. Kärtner, High conversion efficiency, high energy terahertz pulses by optical rectification in cryogenically cooled lithium niobate, Optics Letters 38 (2013) 796-798.

[151] C. Vicario, B. Monoszlai, C. Lombosi, A. Mareczko, A. Courjaud, J.A. Fülöp, C.P. Hauri, Pump pulse width and temperature effects in lithium niobate for efficient THz generation, Optics Letters 38 (2013) 5373-5376.

[152] Y. Shen, T. Watanabe, D.A. Arena, C.C. Kao, J.B. Murphy, T.Y. Tsang, X.J. Wang, G.L. Carr, Nonlinear cross-phase modulation with intense single-cycle terahertz pulses, Physical Review Letters 99 (2007) 043901.

[153] S.B. Bodrov, A.A. Murzanev, Y.A. Sergeev, Y.A. Malkov, A.N. Stepanov, Terahertz generation by tilted-front laser pulses in weakly and strongly nonlinear regimes, Applied Physics Letters 103 (2013) 251103.

[154] L.J. Wong, A. Fallahi, F.X. Kärtner, Compact electron acceleration and bunch compression in THz waveguides, Optics Express 21 (2013) 9792-9806.

[155] M.T. Reiten, S.A. Harmon, R.A. Cheville, Terahertz beam propagation measured through three-dimensional amplitude profile determination, Journal of the Optical Society of America B 20 (2003) 2215-2225.

[156] J.F. Molloy, M. Naftaly, R.A. Dudley, Characterization of terahertz beam profile and propagation, IEEE Journal of Selected Topics in Quantum Electronics 19 (2013) 8401508-8401508.

[157] T.I. Oh, Y.J. Yoo, Y.S. You, K.Y. Kim, Generation of strong terahertz fields exceeding 8 MV/cm at 1 kHz and real-time beam profiling, Applied Physics Letters 105 (2014) 041103.

[158] K. Pernille, C.S. Andrew, I. Krzysztof, J. Peter Uhd, Experimental three-dimensional beam profiling and modeling of a terahertz beam generated from a two-color air plasma, New Journal of Physics 15 (2013) 075012.

[159] P. Klarskov, A.C. Strikwerda, T. Wang, M. Zalkovskij, P.U. Jepsen, in: SPIE OPTO, (SPIE, 2013).

[160] S.B. Bodrov, A.N. Stepanov, M.I. Bakunov, B.V. Shishkin, I.E. Ilyakov, R.A. Akhmedzhanov, Highly efficient optical-to-terahertz conversion in a sandwich structure with $LiNbO_3$ core, Optics Express 17 (2009) 1871-1879.

[161] S.B. Bodrov, M.I. Bakunov, M. Hangyo, Efficient Cherenkov emission of broadband terahertz radiation from an ultrashort laser pulse in a sandwich structure with nonlinear core, Journal of Applied Physics 104 (2008) 093105.

[162] S.B. Bodrov, I.E. Ilyakov, B.V. Shishkin, A.N. Stepanov, Efficient terahertz generation by optical rectification in Si-$LiNbO_3$-air-metal sandwich structure with variable air gap, Applied Physics Letters 100 (2012) 201114.

[163] M.I. Bakunov, E.A. Mashkovich, M.V. Tsarev, S.D. Gorelov, Efficient Cherenkov-type terahertz generation in Si-prism-$LiNbO_3$-slab structure pumped by nanojoule-level ultrashort laser pulses, Applied Physics Letters 101 (2012) 151102.

[164] K. Suizu, K. Koketsu, T. Shibuya, T. Tsutsui, T. Akiba, K. Kawase, Extremely frequency-widened terahertz wave generation using Cherenkov-type radiation, Optics Express 17 (2009) 6676-6681.

[165] W. Shi, Y.J. Ding, Designs of terahertz waveguides for efficient parametric terahertz generation, Applied Physics Letters 82 (2003) 4435-4437.

[166] K.L. Vodopyanov, Y.H. Avetisyan, Optical terahertz wave generation in a planar GaAs waveguide, Optics Letters 33 (2008) 2314-2316.

[167] Z. Ruan, G. Veronis, K.L. Vodopyanov, M.M. Fejer, S. Fan, Enhancement of optics-to-THz conversion efficiency by metallic slot waveguides, Optics Express 17 (2009) 13502-13515.

[168] L. Pálfalvi, J.A. Fülöp, J. Hebling, Absorption-reduced waveguide structure for efficient terahertz generation, Applied Physics Letters 107 (2015) 233507.

[169] B.E.A. Saleh, M.C. Teich, Fundamentals of photonics (Wiley Interscience, Hoboken, N.J., 2007).

[170] W. Schneider, A. Ryabov, C. Lombosi, T. Metzger, Z. Major, J.A. Fülöp, P. Baum, 800-fs, 330-µJ pulses from a 100-W regenerative Yb:YAG thin-disk amplifier at 300 kHz and THz generation in LiNbO3, Optics Letters 39 (2014) 6604-6607.

[171] K.L. Vodopyanov, Terahertz-wave generation with periodically inverted gallium arsenide, Laser Physics 19 (2009) 305-321.

[172] P. Malevich, G. Andriukaitis, T. Flöry, A.J. Verhoef, A. Fernández, S. Ališauskas, A. Pugžlys, A. Baltuška, L.H. Tan, C.F. Chua, P.B. Phua, High energy and average power femtosecond laser for driving mid-infrared optical parametric amplifiers, Optics Letters 38 (2013) 2746-2749.

[173] M. Hemmer, D. Sánchez, M. Jelínek, V. Smirnov, H. Jelinkova, V. Kubeček, J. Biegert, 2-µm wavelength, high-energy Ho:YLF chirped-pulse amplifier for mid-infrared OPCPA, Optics Letters 40 (2015) 451-454.

[174] D. Peceli, P. Olszak, C. Cirloganu, S. Webster, L. Padilha, T.R. Ensley, H. Hu, G. Nootz, D.J. Hagan, E.W. Van Stryland, in: Nonlinear Optics, (Optical Society of America, Kohala Coast, Hawaii, 2013).

[175] C.M. Cirloganu, P.D. Olszak, L.A. Padilha, S. Webster, D.J. Hagan, E.W.V. Stryland, Three-photon absorption spectra of zinc blende semiconductors: theory and experiment, Optics Letters 33 (2008) 2626-2628.

[176] V. Nathan, A.H. Guenther, S.S. Mitra, Review of multiphoton absorption in crystalline solids, Journal of the Optical Society of America B 2 (1985) 294-316.

[177] M.I. Bakunov, S.B. Bodrov, Terahertz generation with tilted-front laser pulses in a contact-grating scheme, Journal of the Optical Society of America B 31 (2014) 2549-2557.

[178] T. Tanabe, K. Suto, J. Nishizawa, K. Saito, T. Kimura, Tunable terahertz wave generation in the 3- to 7-THz region from GaP, Applied Physics Letters 83 (2003) 237-239.

[179] M. Tsubouchi, K. Nagashima, F. Yoshida, Y. Ochi, M. Maruyama, Contact grating device with Fabry-Perot resonator for effective terahertz light generation, Optics Letters 39 (2014) 5439-5442.

[180] E. Kaksis, G. Almási, J.A. Fülöp, A. Pugžlys, A. Baltuška, G. Andriukaitis, 110-mJ 225-fs cryogenically cooled Yb:CaF_2 multipass amplifier, Optics Express 24 (2016) 28915-28922.

[181] R. DeSalvo, A.A. Said, D.J. Hagan, E.W.V. Stryland, M. Sheik-Bahae, Infrared to ultraviolet measurements of two-photon absorption and n_2 in wide bandgap solids, IEEE Journal of Quantum Electronics 32 (1996) 1324-1333.

[182] A.A. Said, M. Sheik-Bahae, D.J. Hagan, T.H. Wei, J. Wang, J. Young, E.W. Van Stryland, Determination of bound-electronic and free-carrier nonlinearities in ZnSe, GaAs, CdTe, and ZnTe, Journal of the Optical Society of America B 9 (1992) 405-414.